Molecular and Functional Characterization of the Galectin-3-Binding Protein LGALS3BP in Cancer and Centrosome Biology

Inaugural-Dissertation

to obtain the academic degree
Doctor rerum naturalium (Dr. rer. nat.)

submitted to the Department of Biology, Chemistry and Pharmacy
of Freie Universität Berlin

by
Sophia Schade
from Berlin

2015

Die vorliegende Arbeit wurde von Oktober 2010 bis Dezember 2015 unter der Leitung von Herrn PD Dr. Bodo Lange in der Abteilung von Herrn Prof. Dr. Hans Lehrach am Max-Planck-Institut für molekulare Genetik in Berlin angefertigt.

1. Gutachter:	PD Dr. Bodo Lange Abteilung Analyse des Vertebratengenoms Max-Planck-Institut für molekulare Genetik
2. Gutachter:	Prof. Dr. Rupert Mutzel Institut für Biologie – Mikrobiologie Freie Universität Berlin
Disputation am:	30.03.2016

Acknowledgments

First of all, I would like to express my greatest gratitude to my supervisor Bodo Lange who introduced me into this interesting research field and who supported my work throughout the past years with his vast knowledge and patient mentoring.

I am grateful to Prof. Mutzel for reviewing this thesis and for being a member of my committee. I would also like to thank Prof. Lehrach for introducing me into his department and for giving me the opportunity to finish my thesis in such a well-connected research environment.

I would particularly like to thank Prof. Schweiger for our fruitful collaboration and for all the enthusiasm she brought into this work. Special thanks go to her former group members Andrea Wunderlich and Stefan Börno who did an excellent job contributing to the *LGALS3BP* transcriptional regulation part of this thesis.

My sincere thanks go to all the members of the former Lange group. You were more than just colleagues as we helped each other for better or for worse. I cannot thank you enough for the great atmosphere during the working time and for the joyful moments we had in-between. Particularly, I thank Hannah Müller for the co-work on our publication and for the proof-reading of my thesis. Thank you Marie-Laure Fogeron for the initial work on this project and Verena Lehmann for managing all the lab things. Having started in a huge group, I am now the last one to turn off the lights. I wish you all the best for the future and hope that we will further stay in contact.

Many thanks go to all my friends inside and outside the institute for taking my mind off things when I needed it and for discussing important things like the origin of the universe.

Who would I be without my family? Thank you for always believing in me and supporting me in all my interests ever since I can remember.

Contents

Abstract

The centrosome acts as the main microtubule-organizing centre in eukaryotic cells. Besides its function in microtubule nucleation it is further implicated in integrating cellular signalling pathways that are essential for cell cycle progression or the response to DNA damage, for instance. In cancer, numerical and structural centrosome aberrations are frequently detected where they contribute to chromosomal instability. Seeking for factors that are functionally relevant for these centrosomal abnormalities, our group established a protein-protein interaction network among centrosomal and cell cycle-regulatory proteins using TAP-MS analysis. Thereby, LGALS3BP, which is deregulated in cancer, was revealed to interact with centrosomal components. The subcellular localization of LGALS3BP to centrosomes and in particular to the proximal part of centrioles was validated by several approaches in this study. LGALS3BP has been previously reported as a secreted glycoprotein with extracellular functions. The present study, however, provides striking evidence that LGALS3BP is involved in the maintenance of centrosome integrity: LGALS3BP upregulation caused centrosome hypertrophy, while depletion led to an accumulation of defective centriolar structures. Supportingly, LGALS3BP deregulation correlated with centrosome abnormalities in certain prostate as well as breast cancer cell lines. Importantly, two rescue experiments revealed a reversion of these phenotypes towards control cells upon restoration of normal LGALS3BP levels. Furthermore, the presence of both LGALS3BP and its interaction partner C-Nap1 was found to be crucial for cell proliferation and viability as simultaneous loss of these proteins caused aneuploidy and apoptosis. An *in vitro* kinase assay on LGALS3BP peptides revealed AKT1, CHK1 and CHK2 as candidate kinases, which suggests an implication of LGALS3BP in AKT signalling downstream events and DNA damage response. Together, these findings asked for mechanisms that regulate LGALS3BP expression and reasons for its deregulation in cancer. The present study revealed BRD4 as a positive regulator of *LGALS3BP* gene expression and as a mediator of INFγ-induced LGALS3BP upregulation. Additionally, EZH2 was found responsible for silencing *LGALS3BP* gene expression in prostate cancer as EZH2 depletion in a respective prostate cancer cell line led to re-expression of LGALS3BP. BRD4 and EZH2 are deregulated in various cancer types, which might explain LGALS3BP

deregulation and centrosome aberrations. This study represents the first characterization of intracellular LGALS3BP maintaining centrosome integrity and function. The new insights into *LGALS3BP* transcriptional regulation now provide opportunities to study if epigenetic therapies targeting *LGALS3BP* could counteract centrosome aberration in cancer.

Zusammenfassung

Das Zentrosom stellt das wesentliche Mikrotubuli-organisierende Zentrum in eukaryotischen Zellen dar. Neben seiner Funktion bei der Mikrotubulinukleation ist es beteiligt an der Integration von zellulären Signaltransduktionswegen, welche beispielsweise für das Fortschreiten des Zellzyklus sowie für die Antwort auf DNS-Schäden wichtig sind. Numerische und strukturelle Aberrationen des Zentrosoms treten sehr häufig während der Krebsentstehung auf und tragen zur Ausbildung von chromosomaler Instabilität bei. Um funktionell relevante Faktoren für diese zentrosomalen Anomalien zu identifizieren, wurde von unserer Arbeitsgruppe ein Proteininteraktionsnetzwerk mittels TAP-MS-Analyse etabliert, welches sich um zentrosomale und Zellzyklus-regulierende Proteine aufbaut. Hierbei wurde LGALS3BP, ein in Krebs dereguliertes Protein, entdeckt, welches mit anderen zentrosomalen Proteinen interagierte. Es konnte durch mehrere Methoden gezeigt werden, dass LGALS3BP am Zentrosom lokalisiert und zwar insbesondere am proximalen Teil der Zentriolen. Zuvor wurde LGALS3BP als ein sekretiertes Glykoprotein mit extrazellulären Funktionen beschrieben. Diese Studie jedoch belegt, dass LGALS3BP auch an der Aufrechterhaltung zentrosomaler Integrität beteiligt ist. Eine Hochregulation von LGALS3BP führte zu zentrosomaler Hypertrophie, wohingegen eine Verminderung von LGALS3BP eine Akkumulation fehlerhafter zentriolärer Strukturen bewirkte. Diese Ergebnisse korrelieren positiv mit LGALS3BP-Fehlexpression und zentrosomalen Aberrationen in verschiedenen Prostata- und Brustkrebszelllinien. Zudem konnte durch die Wiederherstellung normaler LGALS3BP-Expression in zwei Experimenten der jeweilige zentrosomale Phänotyp rückgängig gemacht werden. Es wurde außerdem gezeigt, dass LGALS3BP zusammen mit seinem Interaktionspartner C-Nap1 für die Zellproliferation und -lebensfähigkeit benötigt wird, da das Herunterregulieren beider Proteine zu Aneuploidie und Apoptose führte. Des Weiteren wurden die Kinasen AKT1, CHK1 und CHK2 über eine *in vitro* Phosphorylierungs-Analyse an LGALS3BP-Peptiden identifiziert, was darauf hindeutet, dass LGALS3BP in AKT-Signalwegen und in Antwortmechanismen auf DNS-Schäden involviert sein könnte. Aufgrund dieser Ergebnisse stellte sich die Frage nach Möglichkeiten der transkriptionellen Regulation von *LGALS3BP* und nach den Ursachen dessen Deregulierung in Krebs. In dieser Studie

wurde BRD4 als ein positiver Regulator der *LGALS3BP*-Genexpression ermittelt, welcher auch als Mediator der INFγ-Antwort von *LGALS3BP* agierte. Zudem wurde EZH2 für die *LGALS3BP*-Genstilllegung in Prostatakrebs verantwortlich gefunden, da eine Verminderung von EZH2 zur Reexpression von LGALS3BP in einer entsprechenden Prostatakrebszelllinie führte. In verschiedenen Krebsarten werden BRD4 und EZH2 häufig fehlexprimiert, was auch die LGALS3BP-Deregulation und somit die zentrosomalen Anomalien erklären könnte. Die vorliegende Arbeit stellt die erste Charakterisierung von intrazellulärem LGALS3BP dar, welches zentrosomale Integrität und Funktion aufrechterhält. Die neuen Einblicke in die transkriptionelle Regulation von *LGALS3BP* erlauben es nun experimentell zu ergründen, ob auf *LGALS3BP* gerichtete epigenetische Therapien Auswirkungen auf die Krebsentwicklung haben und die möglicherweise ursächlichen zentrosomalen Anomalitäten reduzieren.

1. Introduction

1.1 The centrosome

The centrosome is a non-membranous organelle, which acts as the main microtubule organizing centre (MTOC). It is present in eukaryotic cells with the exception of higher plants (angiosperms, gymnosperms) and the majority of animal oocytes. Our knowledge of centrosome assembly and function has acceleratingly increased ever since its discovery in 1887, independently by Edouard van Beneden and Theodor Boveri[1]. Nevertheless, today we are just beginning to unveil the compositional and functional complexity of this organelle throughout cell cycle and development as well as its implications in various diseases.

1.1.1 Structure of the vertebrate centrosome

In vertebrates, a mature centrosome is comprised of two centrioles in orthogonal arrangement that are embedded in a protein-rich matrix, called pericentriolar material (PCM) (Figure 1a)[2]. Amazingly, the human centrosome contains hundreds of proteins, including cell cycle regulators and signalling molecules, which either permanently or transiently localize to centrosomes[3–5]. The centrioles are barrel-shaped structures that are made up of nine microtubule triplets, which are radially arranged and stabilized via acetylation as well as poly-glutamylation[6,7]. Compared to the so-called daughter centriole, the older mother centriole additionally owns distal and subdistal appendages that are essential for microtubule anchoring and docking to the plasma membrane during ciliogenesis[2,8,9]. From G1 until G2 phase of cell cycle, mother and daughter centriole are tethered by interconnecting fibres[10]. Although the PCM appears amorphous in electron microscopy, subdiffraction microscopy revealed that it is highly structured by concentric toroidal layers of certain PCM proteins around centrioles and a spoke-like arrangement of the PCM protein pericentrin[11–13]. Towards mitosis, this architecture expands together with acquisition of further components, to reach the maximal MTOC activity[14]. Microtubule nucleation is mediated by the MTOC via γ-tubulin ring complexes (γ-TuRCs), which accumulate at centrosomes acting as templates by presenting a ring of γ-tubulins that make longitudinal contacts with

dimers of α- and β-tubulins (Figure 1b), which is comprehensively reviewed by Kollman *et al.*[15]

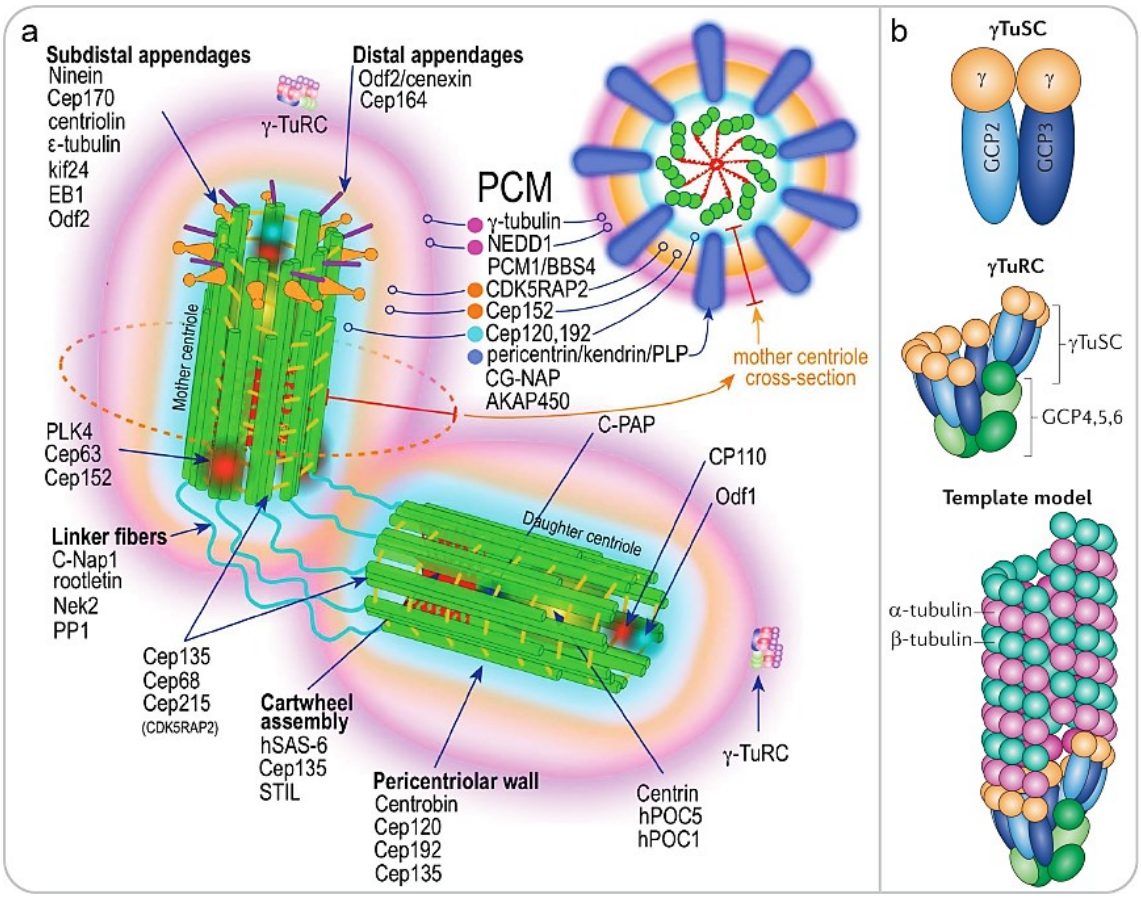

Figure 1: The vertebrate centrosome and γ-TuRC-mediated microtubule nucleation
(a) Schematic representation of a vertebrate centrosome in G1 phase of cell cycle. Mother and daughter centriole are tethered by linker fibres and embedded in the highly structured pericentriolar material (PCM). Several key proteins as well as their localization are given by this figure, which is taken from Pihan[16]. **(b)** The γ-tubulin small complex (γ-TuSC) is highly conserved in eukaryotes and essential for microtubule nucleation. Together with additional γ-tubulin complex proteins (GCPs) it makes up the γ-tubulin ring complex (γ-TuRC), which acts as a template for nucleating microtubules of 13-fold symmetry. Figure modified from Kollman *et al.*[15]

1.1.2 The centrosome duplication cycle

In proliferating cells, a single centrosome has to duplicate and to separate once per cell cycle to form a bipolar mitotic spindle. During cytokinesis, each daughter cell then receives one centrosome as well as one set of chromosomes.

Centrosome duplication exhibits noticeable similarities compared to DNA replication: both occur semiconservatively as well as only once per cell cycle and they are strictly controlled by the activity of cyclins in complex with cyclin-dependent kinases (CDKs).

Furthermore, both rely on licensing mechanisms to prevent reduplication in a single cell cycle[17,18]. To ensure chromosomal stability, centrosome as well as chromosome replication cycle have to proceed synchronously and in a coordinated manner. Therefore, core components of the cell cycle machinery also regulate the centrosome cycle. At the G1/S phase transition, cyclin E or A/CDK2 activity is required for procentriole formation[19–22]. Active CDK2 inactivates the anaphase-promoting complex/cyclosome (APC/C) towards the end of G1 phase and thereby prevents proteasomal degradation of its target proteins, such as SAS6, STIL and CPAP, which are critical for procentriole assembly[23–25]. CDK2 activation at the end of G1 phase thus couples the G1/S phase transition with the onset of procentriole formation. In mitosis, cyclin B/CDK1 activity leads to the activation of Aurora A kinase, which in turn activates PLK1 to trigger centriole disengagement[26–28]. Centriole disengagement also requires separase activity, which is checked by securin until the spindle assembly checkpoint has been satisfied at metaphase to anaphase transition, indicating further coupling of centrosome duplication and cell cycle[28,29].

In G1 phase of cell cycle, mother and daughter centriole are close to another, disengaged but tethered by linker fibres established by C-Nap1, rootletin, CEP68 and CEP215 (Figure 1a and Figure 2)[30,31].

At the onset of S phase, one procentriole begins to assemble orthogonally to the proximal part of the mother and the daughter centriole, respectively (Figure 2). In human cells, PLK4, CEP192, SAS6, STIL and CPAP are essential for procentriole assembly, since their depletion inhibits procentriole formation, while their overexpression gives rise to supernumerary procentrioles[32]. Furthermore, CEP57, CEP63 and CEP152 contribute to procentriole assembly by forming a ring at the proximal part of centrioles[33–35]. CEP192 and CEP152 together recruit PLK4 to one location within this ring and thereby trigger procentriole formation[12,36]. In the following, PLK4 binds and phosphorylates STIL promoting its association with SAS6, which in turn assembles a cartwheel structure of nine-fold symmetry[37–41]. STIL additionally interacts with CPAP, which initiates procentriole elongation with CEP135 stabilizing the cartwheel as well as binding to the microtubule triplets and centrobin as well as CP110 limiting procentriole length[25,42–45]. Thereafter, STIL and SAS6 are degraded and no longer detectable at the onset of G1 phase of the next cell cycle[23,24].

Initially lacking PCM, the procentrioles now acquire PCM as the centrosomes steadily accumulates PCM, a step called centrosome maturation, to reach its maximal microtubule-organizing capacity in mitosis through collective action of the kinases Aurora A and PLK1 (Figure 2)[46,47].

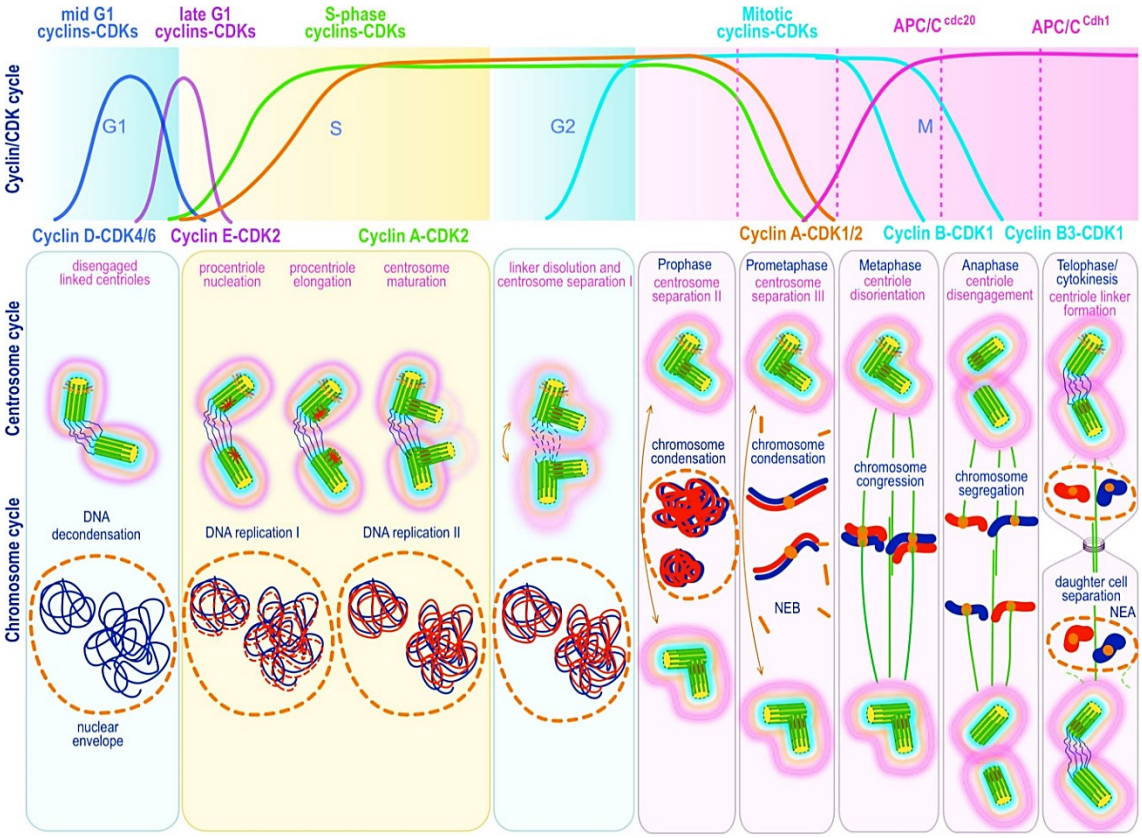

Figure 2: The centrosome and chromosome cycle in the course of cell cycle
Schematic illustration of key centrosomal and nuclear events throughout the cell cycle, including the course of specific cyclin/CDK activities to correlate and compare with. APC/C: anaphase-promoting complex/cyclosome; cdc20: cell-division cycle protein 20; Cdh1: Cdc20-homologue 1; CDK: cyclin-dependent kinase; NEB: nuclear envelope breakdown; NEA: nuclear envelope assembly. Figure taken from Pihan[16].

At G2/M phase transition, the proteinaceous linker between the parental centrioles is removed by NEK2-mediated phosphorylation of C-Nap1 and rootletin under control of PLK1, a step referred to as centrosome disjunction[31,48–54]. Subsequently, the two centrosomes separate, which is mediated by the motor protein kinesin-5, to form a bipolar mitotic spindle ensuring even distribution of the genetic material to daughter cells[55,56].

In the course of mitosis, the centriole and procentriole disengage by losing their orthogonal association while establishing a new proteinaceous linker at their proximal

ends and thus completing the duplication cycle (Figure 2)[16]. Since very recently, the precise mechanism of centriole disengagement has been solved: CEP215 is present at two distinct centrosomal locations, for one bound to CEP68 and for another bound to pericentrin. Plk1-mediated degradation of Cep68 as well as separase-mediated cleavage of pericentrin release both pools of Cep215 thereby promoting centriole disengagement[28]. As centriole-procentriole engagement prevents further procentriole assembly, their disengagement is considered as a licensing step for procentriole formation in the following cell cycle[18,57].

1.1.3 Centrosome functions

The centrosome exerts several cellular functions by acting as a MTOC and as a hub that integrates multiple key signalling pathways[58].

Since the centrosome is the main MTOC in eukaryotic cells, it is implicated in the coordination of microtubule-dependent functions. In interphase, the microtubule cytoskeleton shapes the cells, organizes their cytoplasm by positioning organelles, providing trails for intracellular transport as well as establishing cell polarity, and is further pivotal for cell motility and adhesion[59,60]. In mitosis, the microtubule cytoskeleton has to be rearranged into a bipolar mitotic spindle to ensure even segregation of chromosomes[59]. However, cells can also divide normally in systems with naturally absent centrosomes, as during female meiosis or in higher plants, by nucleating microtubules near chromosomes and focussing their minus ends via microtubule motor and microtubule-bundling proteins[61]. Contrarily, centrosomes are indispensable for asymmetric cell division as they contribute to a proper spindle orientation[62].

Centrosomes, in particular centrioles, are further essential to form cilia and flagella. In cells that have exited cell cycle, the centrosome migrates to the cell surface where the mother centriole transforms into a basal body of a cilium. Motile cilia, which own an axoneme of nine outer microtubule doublets and a central microtubule pair, are mainly found in epithelial cells protruding numerously from the apical pole to promote body fluid flow. Primary, non-motile cilia, which lack the central pair, are present in

almost all cell types to serve as sensory centres that regulate cell proliferation and embryonic development[63].

As detailed above, the centrosome cycle is closely linked to cell cycle progression. The centrosome itself, however is also involved in directing certain cell cycle events[64,65]. This might be mediated by the centrosome via acting as a scaffold that positions cell cycle regulatory proteins close to their downstream targets or upstream regulators[66].

The centrosome might regulate mitotic entry as cyclin B/CDK1 activation initially occurs at centrosomes at the onset of mitosis before it dissociates from the centrosome to promote nuclear envelope breakdown, chromatin condensation and mitotic spindle formation[67]. Centrosomal Aurora A and CHK1 properly time the G2/M transition, with Aurora A acting as a positive and CHK1 as a negative upstream regulator of CDK1 via targeting CDC25B (Figure 3)[68–70].

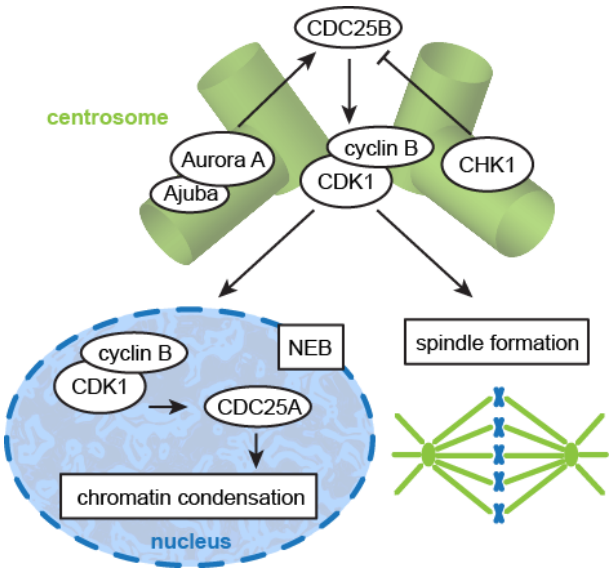

Figure 3: Regulation of the G2/M transition
Ajuba mediates centrosomal Aurora A activation, which leads to the recruitment of CDC25B to centrosomes. Aurora A then phosphorylates CDC25B, which subsequently activates CDK1/cyclin B to initiate early mitotic events like nuclear envelope breakdown (NEB), chromatin condensation and spindle formation. CHK1 expression is restricted to S and G2 phase of cell cycle and localizes to centrosomes in interphase but not in mitosis. During interphase CHK1 restrains CDK1 activity through local inhibition of CDC25B thereby preventing premature mitotic entry. At the end of G2 phase, CHK1 dissociates from centrosomes to allow initiation of mitotis[68–70].

Furthermore, the centrosome might be required for cytokinesis. At the end of telophase, the mother centriole transiently moves to the midbody, which marks the abscission site between the two daughter cells[71]. In cells with experimentally removed centrosomes, a cleavage furrow is formed, but cytokinesis cannot be completed [72,73]. As the Golgi complex associates with migrating centrosomes, it is suggested that this transient movement delivers secretory vesicles as well as other regulatory components to the midbody that are required for cytokinesis[65]. In agreement with this, several

centrosomal proteins localize to the midbody, e.g. CEP55 or centriolin, which are essential for proper cytokinesis[4,74–77].

Previously, centrosomes have been implicated in regulating G1/S transition as their loss caused cell cycle arrest in G1 phase[73,78,79]. However, later research unveiled that loss of centrosome integrity rather triggers cellular stress responses involving p38 and p53, which induce p21-mediated cell cycle arrest in G1 phase[80–82].

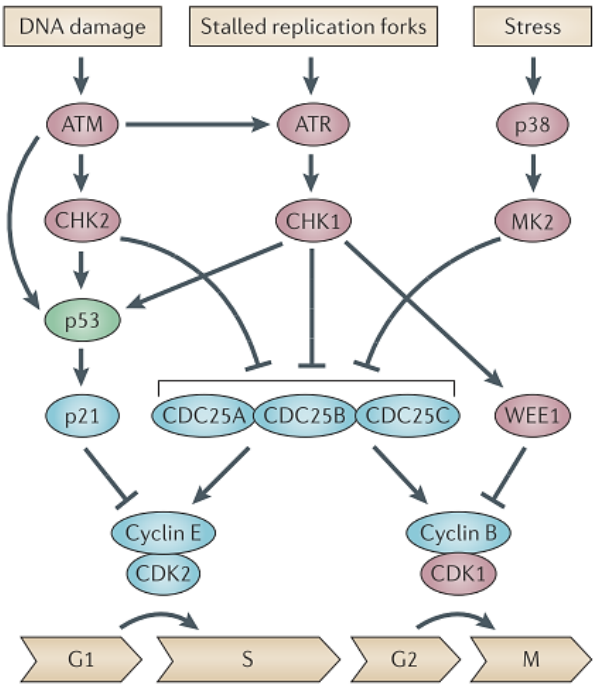

Figure 4: The DNA damage checkpoints
ATM is activated upon DNA double-strand breaks elicited by ionizing radiation or other genotoxic insults. ATR activation is caused by a broader spectrum of stress such as after DNA single-strand breaks upon ultraviolet irradiation, hypoxia or DNA replication stress. ATM activates CHK2 and ATR activates CHK1 to promote the degradation of CDC25 phosphatases or to activate the p53-p21$^{CIP/WAF1}$ pathway ending up in inhibitory phosphorylated cyclin-dependent kinases (CDKs). Additionally, CHK1 can activate the G2/M inhibiting kinase WEE1 to maintain genomic integrity. Together, this causes cell cycle arrest in G1, S or G2 phase of interphase or prevention of mitotic entry to allow cellular coordination of DNA repair, cell cycle progression, transcription, apoptosis or senescence[83–88]. MK2: MAPK-activated protein kinase 2. Figure from Bouwman and Jonkers[89].

The centrosome is further implicated in the checkpoint response to DNA damage as several DNA damage checkpoint proteins, such as ATM, ATR, CHK1, CHK2 and p53, can localize to this organelle (Figure 4)[90–92]. Specific inhibition of centrosomal CHK1 activity, for instance, is sufficient to interrupt DNA damage-induced G2 phase arrest[93].

Considering the aforementioned functions of the centrosome, it is easily conceivable that centrosome dysfunction may contribute to a plethora of diseases, such as ciliopathies, neurodegenerative disorders and cancer.

1.1.4 Centrosome aberrations and cancer

Centrosome aberrations occur frequently in cancer and are implicated in promoting chromosomal instability (CIN), one of the hallmarks of cancer[94]. They can be classified into structural and numerical centrosomal abnormalities, with the latter ones being

the most abundantly documented phenotypes[95]. Pihan extensively reviewed how supernumerary centrosomes may arise from over-replication of pre-existing centrosomes within one cell cycle[96–98], *de novo* formation[99,100] or from accumulation of centrosomes due to cytokinesis failure[16,101,102]. The numerical classification of centrosome aberrations, however, does not account for their qualitative aspects, which may be represented by misshaped centrioles, excess or insufficient PCM or acentriolar MTOCs[103–106].

Supernumerary centrosomes give rise to multipolar mitotic spindles, an outcome that depends on several additional factors. One critical factor for a successful division is the ploidy of the dividing cell as daughter cell viability depends on receiving a full haploid set of chromosomes[16]. Other factors comprise the ability to bypass the spindle assembly checkpoint[107], the competence of apoptotic pathways leading to mitotic[108] and post-mitotic[109] cell death, the ability to exit mitosis before anaphase (mitotic slippage) and importantly the ability to rearrange a multipolar spindle into a bipolar spindle before anaphase[16,109,110]. Figure 5 hereof illustrates the possible outcome of multipolar mitoses as outlined by Pihan[16].

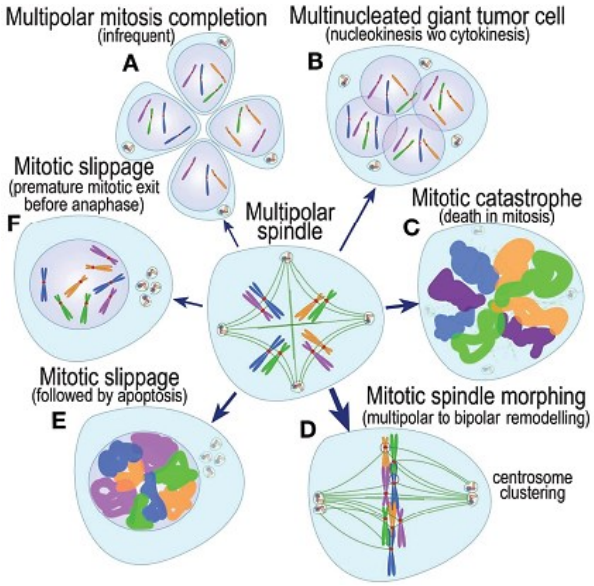

Figure 5: The outcome of multipolar mitoses
(A) A rare fraction of cells successfully complete multipolar mitosis as highly aneuploid cells. **(B)** Others fail cytokinesis resulting in multinucleated giant cells. **(C)** Some cells die directly during mitosis (mitotic catastrophe) or **(E)** in G1 phase after mitotic slippage. **(F)** Another fraction of cells exits mitosis before anaphase to become polyploid with supernumerary centrosomes. **(D)** Most multipolar mitotic cells, however, cluster their centrosomes after a certain delay to form bipolar spindles resulting in mostly normal but also abnormal (merotelic or syntelic) microtubule-kinetochore attachments. The arrow thickness estimates the frequency of these events. Figure taken from Pihan[16].

Frequently, the outcome of multipolar mitoses impacts cellular fitness and growth. Centrosome clustering, however, is an efficient mechanism that limits multipolar cell division[111]. The multipolar to bipolar spindle rearrangement before anaphase bears a risk for abnormal, merotelic or syntelic, spindle microtubule-kinetochore attachments

(Figure 6). Particularly, merotelic attachments are dangerous as they are poorly sensed by the spindle assembly checkpoint and may give rise to lagging chromosomes[112,113]. But also syntelic attachments are risky as they may promote further merotely[113,114]. As a result, missegregation of chromosomes might then induce unstable aneuploidy, which is also known as CIN.

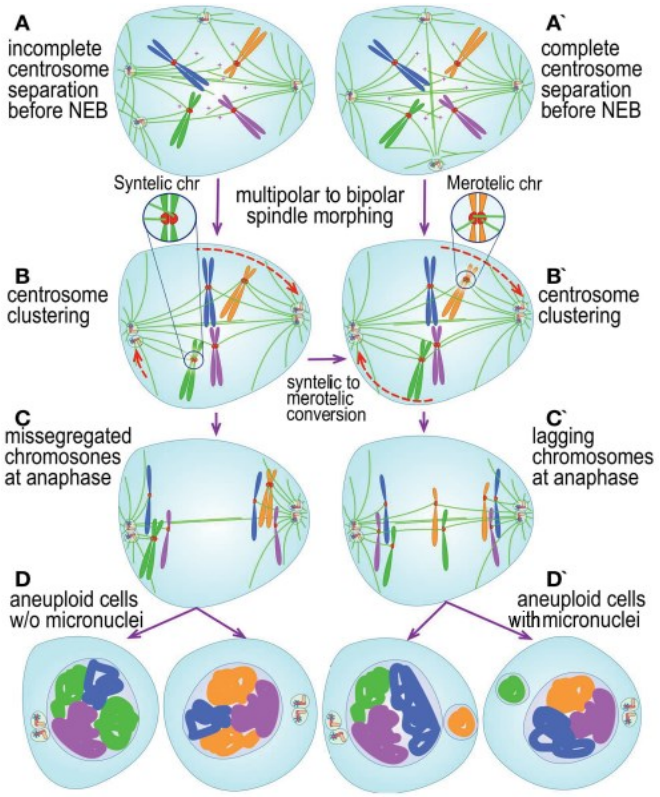

Figure 6: Multipolar to bipolar mitotic spindle conversion in cancer cells
Multipolar mitotic spindles arising from supernumerary centrosomes **(A, A')** convert their spindles to a bipolar configuration after a while **(B, B')**. Aberrant syntelic **(B)** or merotelic **(B')** kinetochore attachments acquired during the multipolar state may lead to monopolar chromosome segregation **(C)** or lagging chromosomes **(C')** resulting in aneuploid cells without **(D)** or with **(D')** micronuclei[16]. Centrosome clustering in tumour cells might be mediated by proteins involved in kinetochore microtubule attachment and sister chromatid cohesion as well as by members of the augmin complex microtubule pathway and the chromosome passenger complexes[115].
NEB: nuclear envelope breakdown; w/o: without. Figure taken from Pihan[16].

It should be mentioned here, however, that CIN may not arise from centrosomal aberrations alone, but rather presents a multifactorial phenomenon deriving additionally from defects in kinetochore microtubule attachment and dynamics[116], in the spindle assembly checkpoint[29], in chromosome replication, cohesion or condensation[117], in cytokinesis[118] or from defective checkpoints that manage DNA replication as well as the centrosome cycle[16,119]. Contributing to this, also structural centrosome aberrations may result in CIN by providing abnormal PCM scaffolding and thereby affecting several cellular signalling pathways that may lead to cancer progression.

While being associated with dynamic CIN due to chromosomal missegregation, centrosome abnormalities might also be involved in promoting structural CIN by

micronucleus formation, chromosome breakage at centromeres and DNA damage on aberrantly attached chromosomes[16]. A combination of structural and dynamic CIN might ultimately lead to genomic rearrangements as well as reprogramming of the cancer genome, and thereby contributes to altered gene expression, genetic mutations as well as oncogene gain and tumour suppressor loss, which further drives cancer progression.

1.2 The galectin-3-binding protein LGALS3BP

1.2.1 LGALS3BP protein structure and known functions

Lectin galactoside-binding soluble 3-binding protein (LGALS3BP) has been described as a soluble and highly glycosylated protein, which is secreted to the extracellular matrix where it forms large ring-like oligomers composed of 60 – 90 kDa subunits[120,121]. It is a member of the scavenger receptor cysteine-rich superfamily, which includes secreted as well as membrane-bound proteins implicated in the development of the immune system and in the regulation of immune responses[122].

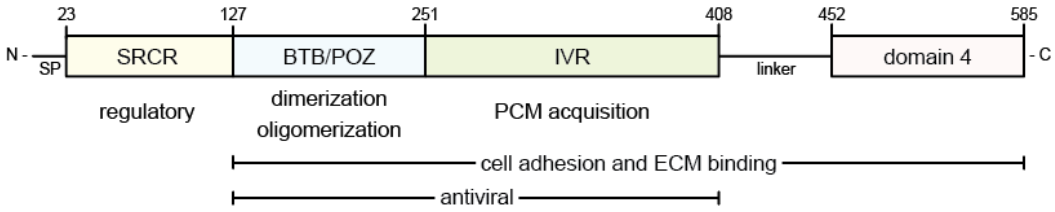

Figure 7: Domain structure of LGALS3BP
The LGALS3BP protein is composed of six stretches with four domains: a secretory signal peptide, a scavenger receptor cysteine-rich (SRCR) domain, subsequent BTB/POZ (BR-C, ttk and bab/ pox virus and zinc finger) and IVR (intervening region) domains and an uncharacterized domain 4, which is connected via a linker region. The proposed domain functions in LGALS3BP oligomerization, pericentriolar material (PCM) acquisition, cell adhesion as well as binding of extracellular matrix (ECM) components and their antiviral properties upon HIV-1 infection are assigned respectively. Domain structure according to Müller *et al.*[121]

The 585 aa sequence of LGALS3BP can be subdivided into six stretches with four structural or functional domains (Figure 7)[121]. The N-terminal secretory signal peptide is followed by a scavenger receptor cysteine-rich (SRCR) domain, which may have a regulatory function in oligomer assembly and, together with the other domains, might mediate binding of LGALS3BP interaction partners[121]. The subsequent BTB/POZ (broad

complex, tram-track, bric-a-brac/ pox virus and zinc finger) and IVR (intervening region) domains have been found necessary for the antiviral function of LGALS3BP after HIV-1 infection[123]. Furthermore, the BTB/POZ domain of LGALS3BP is required for its dimerization and oligomerization (Figure 8), which has been reported for other BTB/POZ-containing proteins as well[121,124–127], and our group identified the IVR domain to be necessary for the acquisition of pericentriolar material (PCM) at centrosomes[128]. The C-terminal putative domain 4 shares no similarity to other proteins and is yet uncharacterized. This domain is connected to the IVR via a linker region that contains a cleavage site for the extracellular protease plasmin at position 441[120,121]. The region comprising the BTB/POZ, IVR and domain 4 was found necessary for mediating cell adhesion through β1 integrins and for binding extracellular matrix (ECM) components, such as galectin-1 and -3, fibronectin, nidogen, laminin and collagen IV - VI[120,121,127].

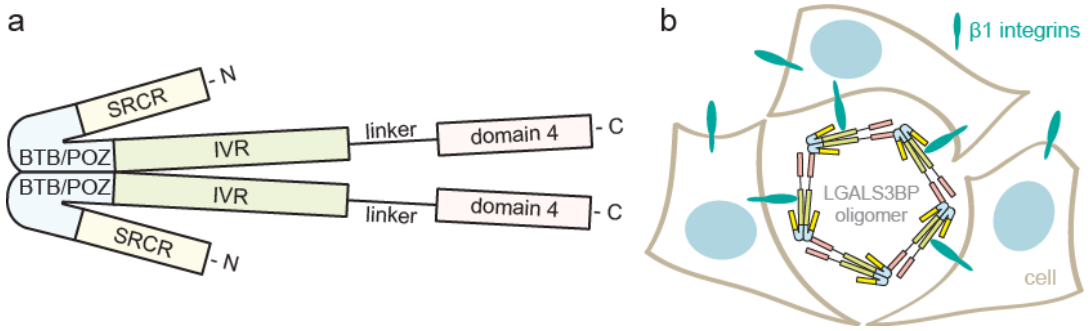

Figure 8: Extracellular LGALS3BP oligomers mediate cell adhesion
(a) The dimerization of LGALS3BP monomers is mediated through interaction of the respective BTB/POZ domains. **(b)** LGALS3BP dimers interact end-to-end, probably via BTB/POZ and domain 4, to form ring-like structures, which mediate cell adhesion through β1 integrins and several other extracellular matrix components. Figure prepared according to Müller *et al.* and Grassadonia *et al.*[121,129]

Several cellular functions have already been suggested for the extracellular pool of LGALS3BP. As already implied, secreted LGALS3BP is implicated in cell adhesion via binding to galectin-3, β1 integrins and several other ECM components (Figure 8b)[120,130].

Furthermore, several studies support a stimulatory role for LGALS3BP in the immune defence system. LGALS3BP has been shown to activate natural killer cells as well as lymphokine-activated killer cells and to induce secretion of the cytokines interleukin 1, 2, 6 and tumour necrosis factor alpha (TNFα) by activated T cells[131,132]. Additionally, LGALS3BP was shown to increase major histocompatibility (MHC) class I antigen expression in human breast cancer[133].

Nevertheless, cellular functions of the intracellular pool of LGALS3BP have not been identified so far.

1.2.2 LGALS3BP expression and function in disease

The LGALS3BP is conserved in the bony vertebrates (*Euteleostomi*). In humans, it is synthesized and secreted by various cell types, including haematopoietic cells and glandular or mucosal epithelia cells[131,134], and can be mainly found in serum as well as other body fluids[134–136].

LGALS3BP is upregulated after viral infections, such as dengue virus[137], hepatitis C virus[138] and human immunodeficiency virus (HIV)[139], for instance. Concerning HIV-1 infections, it has been shown that high LGALS3BP levels in infected mothers and their new-borns correlate with a reduced mother-to-child HIV-1 transmission[140]. In support of this observation, antiviral properties of LGALS3BP have been shown for its BTB/POZ and IVR domain in reducing the viral particle infectivity of HIV-1 by interfering with the maturation and incorporation of viral envelope proteins into progeny virions [123].

In cancer, LGALS3BP is frequently upregulated. Increased LGALS3BP expression in serum or in tumour tissue has been found associated with poor clinical outcome in patients with breast cancer[141,142], hepatocellular cancer[143], pancreatic cancer[144], lung cancer[145,146] and gastric cancer[147], for instance. LGALS3BP upregulation is implicated in metastasis[129,130,145,148], cell motility[149,150], chemoresistance[151], immune evasion of tumour cells[152] as well as oncogenic signalling towards survival, proliferation and migration mediated by cellular adherence to extracellular LGALS3BP[153]. Contrarily, also downregulation of LGALS3BP in certain tumours as well as LGALS3BP-associated favourable prognoses on cancer have been described[154–157].

1.2.3 Known regulators of LGALS3BP expression

The proposed regulatory elements within the *LGALS3BP* promoter already point to some of its transcriptional regulators as it contains a gamma interferon activation site (GAS), an interferon-sensitive response element (ISRE), two NFκB binding sites and several SP1 binding sites, for instance[158,159]. *LGALS3BP* has been reported as an interferon-stimulated gene, which is responsive to type I interferons (e.g. INFα and

INFβ) as well as to the type II interferon INFγ[160–163]. Additionally, LGALS3BP expression is induced by the cytokine TNFα via binding of the transcription factor NFκB to the *LGALS3BP* promoter[164]. Supportingly, another study revealed an induction of LGALS3BP by nerve growth factor (NGF) via the PI3K/AKT/NFκB pathway and that NFκB promoter binding is critical for *LGALS3BP* expression[165]. Therefore, it would not be surprising if LGALS3BP expression is stimulated by other cytokines as well. The induction of LGALS3BP through the aforementioned cytokines underlines its role in immune response and might point to its upregulation in cancer.

There is further evidence that LGALS3BP expression might be epigenetically regulated. The breast cancer cell line MCF-7, which exhibits low LGALS3BP expression, shows a respective upregulation of mRNA expression upon treatment with the DNA-demethylating agent 5-azacytidine[166]. Additionally, microRNA *miR596* has been identified as an epigenetic negative regulator of *LGALS3BP* mRNA expression[167]. An epigenetic regulation of *LGALS3BP* might be another reason for its observed deregulation in cancer as epigenetic alterations occur early during cancer development[168].

1.3 Epigenetics and cancer

Epigenetics is the study of heritable alterations in gene expression that are caused by external or environmental factors and not by changes in the DNA sequence. Epigenetic regulation plays crucial roles in various biological processes including embryonic development, genomic imprinting as well as X-chromosome inactivation[169,170]. Deregulation of epigenetic processes causes aberrant gene function as well as expression and thereby contributes to several human pathologies such as metabolic and autoimmune diseases, neurological disorders and cancer[170–172]. Histone modification, DNA methylation, noncoding RNAs, nucleosome positioning and long-range chromatin interactions are the main machineries of epigenetic modification, which also interplay to constitute an epigenetic theme associated with gene regulation. A detailed description of the epigenetic regulation is beyond the scope of this thesis. The main mechanisms as well as certain examples relevant for this study are therefore very briefly introduced in the following.

1.3.1 Histone modification

In eukaryotes, chromatin describes a highly ordered structure of DNA and proteins that provides packaging of the genome in a cell cycle-dependent manner. The basic functional unit is the nucleosome, which repeats every 160 – 240 bp across the genome and which is interconnected by sections of linker DNA[173]. Each nucleosome contains a nucleosome core, which is composed of an octamer of two copies of the canonical core histones H2A, H2B, H3 and H4, respectively, together with 145 – 147 bp of DNA wrapped around it (Figure 9). The linker histone H1 binds to short linker DNA stretches present on the nucleosome core. The nucleosome core with ≈ 165 bp of DNA together with the linker histone H1 is called chromatosome, which constitutes the nucleosome together with additional linker DNA up to final ≈ 240 bp of DNA[174].

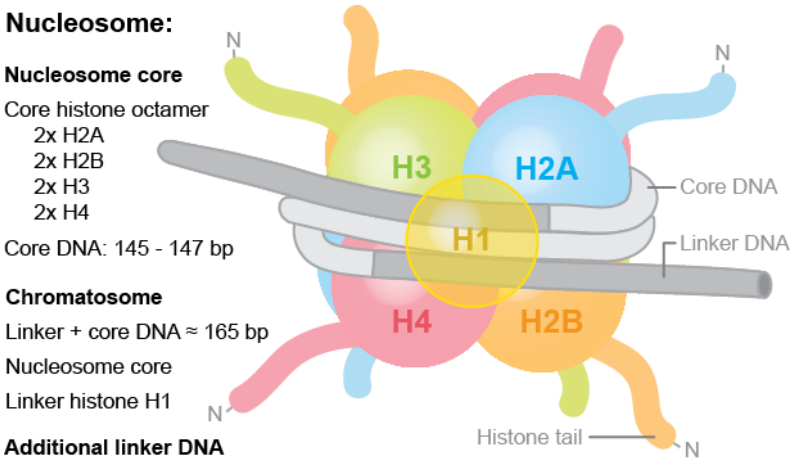

Figure 9: Composition of a nucleosome
The nucleosome core is composed of 145 – 147 bp of core DNA that is wrapped around an octamer of the core histones H2A, H2B, H3 and H4. Nucleosomes are interconnected by linker DNA stretches that are bound by the linker histone H1 at the nucleosome to form the chromatosome. The chromatosome and additional linker DNA constitutes the nucleosome.

Up to now, several post-translational modifications of core histones have been identified, such as acetylation, methylation, phosphorylation and many more, which mainly occur in their terminal tails and which influence chromatin structure thereby playing a crucial role for gene regulation[175–178]. Histones are modified by so-called writers, which covalently add modifications (e.g. histone acetyltransferases, methyltransferases and kinases), and erasers, which remove modifications (e.g. histone deacetylases, demethylases and phosphatases)[179]. Particular modifications on

histones characterize either transcriptionally active or repressed chromatin (Figure 10). Active genes are usually characterized by trimethylation of H3 on lysine 4 (H3K4me3), trimethylation of H3 on lysine 79 (H3K79me3), ubiquitylation of H2B on lysine 120 (H2BK120ub1), trimethylation of H3 on lysine 36 (H3K36me3) as well as high levels of lysine acetylation on H3 and H4 histone tails, for instance[180]. Silent genes, on the other hand, typically show trimethylation of H3 on lysine 27 (H3K27me3), ubiquitylation of H2A on lysine 119 (H2AK119ub1) and trimethylation of H3 on lysine 9 (H3K9me3)[180]. But also the linker histone H1 is post-translationally modified at its N- and C-terminal tails and is thereby involved in regulating gene expression and chromatin dynamics as extensively reviewed by Izzo and Schneider[181].

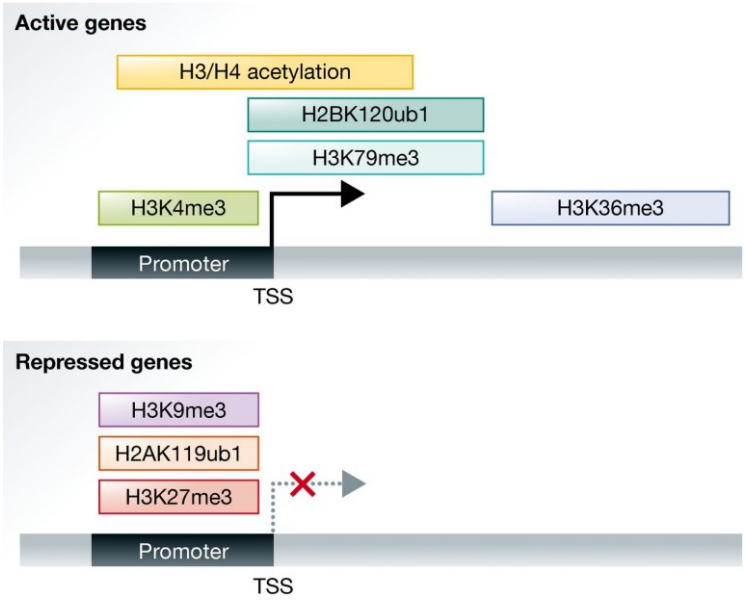

Figure 10: Histone modifications at active and repressed genes
Schematic illustration of some typical histone modifications distributed over active and silent genes. TSS transcription start site. Figure taken from Zhang *et al.*[180]

However, besides influencing chromatin structure, histone modifications can be recognized by so-called readers, specific adaptor proteins that are able to recruit other proteins necessary for gene regulation[179,182,183].

One of those readers is the bromodomain-containing protein 4 (BRD4), which is expressed as three isoforms that vary in their C-terminus given by the absence of 568 or 640 amino acids in the two short isoforms[184,185]. BRD4 recognizes and binds to acetylated lysines on histone H3 and H4 in interphase as well as in mitosis with preferences for H3K14, H4K5 and H4K12[186,187]. By binding to acetylated histones

through its bromodomains, BRD4 is involved in transcriptional regulation as it binds and activates the positive transcription elongation factor b (pTEFb), which in turn phosphorylates the large subunit of RNA polymerase II (RNA Pol II) promoting the transition from transcription initiation to elongation at target genes[188–193]. Additionally, BRD4 exhibits an atypical kinase activity to directly phosphorylate RNA Pol II[194]. Moreover, BRD4 is part of mediator complexes to play a role in transcription initiation[195,196]. Other functions of BRD4 in downstream gene regulation as well as its involvement in cell cycle progression, proliferation, inflammation and oxidative stress response are comprehensively reviewed by Jung *et al.* and Devaiah *et al.*[185,196] Importantly, BRD4 is implicated in numerous haematological as well as solid tumours and several bromodomain inhibitors have been developed so far that appear promising in anti-cancer therapy[185]. Supporting its role in cancer, BRD4 was found to be required for the expression of the proto-oncogene MYC, for instance[197].

As a so-called writer, the enhancer of zeste homolog 2 (EZH2) represents another relevant example for this study. EZH2 is the catalytic subunit of the polycomb repressive complex 2 (PRC2) and displays H3K27 methyltransferase transferase activity[198]. EZH2 as part of PRC2 is able to mono-, di-, and trimethylate H3K27 and these methylation states show different functional roles in gene expression[199]. Today, the link of H3K27me3 to gene repression is well-established. Besides independent processes, a common mechanism of PRC2-dependent gene silencing has been described, in which PRC2-mediated H3K27me3 induces the recruitment of polycomb repressive complex 1 (PRC1) that in turn catalyses the monoubiquitination of H2AK119 to promote chromatin compaction and gene silencing[200,201]. Recently, H3K27me1 has been identified to accumulate at active genes and to promote transcription, while H3K27me2 was shown to prevent the activity of cell type-unspecific enhancers on large chromatin domains[199]. Under normal conditions, EZH2 is expressed in stem cells to maintain pluripotency by silencing differentiation genes[202]. Importantly, in various cancer types, such as prostate cancer for instance, EZH2 is upregulated and implicated in the aggressiveness and prognostic outcome of cancer[202–208]. Supportingly, drug-mediated inhibition of EZH2 has already been shown to interfere with tumour growth and to increase the sensitivity to chemotherapy[209–211].

1.3.2 DNA methylation

DNA methylation is associated with stable gene silencing and occurs primarily at CpG dinucleotides in mammals via covalent modification of cytosine residues. CpG-rich DNA stretches are called CpG islands (CGIs), which are particularly located at the 5' end of genes and occupy ≈ 60 % of human gene promoters[212]. While CpG methylation is detected throughout the genome, the majority of CGIs remain unmethylated in normal cells[213,214]. Exceptionally during development, some CGI promoters are methylated, which remain stably silenced. Well-known examples for this naturally occurring CGI methylation are X-chromosome inactivation in female cells and the monoallelic expression of several imprinted genes[215,216]. Furthermore, certain tissue-specific CGI methylation has been described for developmentally important genes in somatic tissues[217]. Conversely, non-CGI CpG methylation in normal cells, which is spread all over the genome, predominantly occurs at repetitive genome regions, such as satellite DNA, to maintain genome integrity and to reduce transcriptional noise as gathered by various reviews[170,218,219].

Nowadays, gene silencing mediated by DNA methylation of CGI-containing promoters is well-established. Much less is known about methylation of promoters that do not contain CGIs though. However, some studies have already revealed that the repression of genes with non-CGI promoters is mediated by DNA methylation[220–222].

DNA methylation is catalysed by DNA methyltransferases (DNMTs), of which DNMT3A, DNMT3B and DNMT1 are the three mainly acting enzymes. DNMT3A and DNMT3B are so-called *de novo* methyltransferases, which act on unmethylated and hemimethylated CpGs in a replication-independent way. DNMT1 represents a maintenance methyltransferase, which methylates hemimethylated CpGs during replication and thereby contributes to the inheritance of DNA methylation patterns[223–225].

DNA methylation can either directly silence gene expression by interfering with transcription factor binding[226,227] or indirectly by recruiting methyl-binding domain proteins, which in turn mediate gene silencing through interactions with histone deacetylases, for instance[225,228,229].

Interestingly, the aforementioned histone methyltransferase EZH2 was also shown to directly control DNA methylation events: as a part of the PRC2, EZH2 is able to recruit

DNMTs to EZH2-targeted promoters thus providing a direct link between labile gene repression via histone modifications and stable gene silencing via promoter DNA methylation[230].

1.3.3 Noncoding RNAs

Although noncoding RNAs (ncRNAs) are not translated into proteins, they are involved in chromatin regulation, gene expression and other essential cellular functions[231]. They can be categorized into small (< 200 nt) and long (> 200 nt) ncRNAs, which comprise several classes, respectively[231].

MicroRNAs (miRNAs) are 18 – 25 nt small ncRNAs that silence the expression of target genes post-transcriptionally within the RNA-induced silencing complex (RISC) via base-pairing to the mRNA 3'-untranslated regions[232]. MiRNA genes are mainly transcribed by RNA Pol II and, like other genes, they can be regulated via epigenetic mechanisms[233,234]. The other way round, miRNAs can modulate epigenetic mechanisms by targeting regulators of DNA methylation or histone modification, for instance[235,236].

As relevant for the present study, the miRNA *miR26a* was shown to directly target and silence EZH2 expression[237–239]. Additionally, the proto-oncogene MYC was shown to repress *miR26a* and thereby stimulates EZH2 expression, which underlines the implications of EZH2 in various cancer types[240–242]. Furthermore, the *miR26a* gene was found hypermethylated and thus suppressed in *TMPRSS2:ERG* fusion-negative prostate cancer tissue and cell lines correlating with EZH2 overexpression[243].

Interestingly, also long ncRNAs interplay with other epigenetic mechanisms. Davidovich and Cech critically reviewed the recent findings on how long ncRNAs associate with the aforementioned PRC2 and mediate its recruitment to chromatin[244].

1.3.4 Nucleosome positioning and histone variants

As non-covalent epigenetic mechanisms, nucleosome positioning and the incorporation of specialized histone variants play an additional role in regulating chromatin structure and thereby gene expression.

Besides providing DNA packaging, nucleosomes can regulate gene activity by changing the accessibility of regulatory DNA elements to transcription factors. Jiang and Pugh reviewed how certain DNA sequences and chromatin remodelling complexes selectively position and organize nucleosomes so that they can regulate gene expression[245]. High-resolution genome-wide maps of nucleosome positions, for instance, reveal a common organization pattern at almost every gene that shows a nucleosome-free region (NFR) at the beginning and the end of genes. 5' NFRs may represent sites for the assembly of the transcription machinery, while 3' NFRs might provide sites for its disassembly[245]. Furthermore, the first nucleosome downstream of transcription start sites (TSSs) has been revealed to exhibit differential positioning in active and silent genes[246]. It is therefore suggested that TSSs can be determined by the positioning of nucleosomes, which may also regulate transcriptional initiation[245,246]. A deeper knowledge on how nucleosomes are positioned as a response to external stimuli might also unveil how deregulation of nucleosome positioning is leading to developmental defects and cancer.

In addition to nucleosome positioning via nucleosome remodellers, the incorporation of certain histone variants into nucleosomes affects nucleosome allocation and thus gene expression. The expression of the aforementioned canonical core histones (Figure 9) is tightly regulated during cell cycle, and they are incorporated into nucleosomes in a process that is strictly coupled to DNA replication in S phase. Contrarily, histone variants of these subtypes are expressed from orphan genes throughout the cell cycle, and they are incorporated during as well as after the completion of S phase often with the help of special chaperones [247,248]. Some histone variants, such as macroH2A and H2A.Z, differ greatly in their polypeptide sequences, which causes changes in chromatin structure and function[249]. The histone variant H3.3, on the other hand, shows minor differences to the canonical histone H3. However, these minor differences cause substantial changes in post-translational modification as well as in interactions with chromatin readers and chaperones[250–252]. H3.3 and H2A.Z show enrichment at promoters of activated genes or genes prepared for activation, and they are able to alter nucleosome stability thereby mediating gene activation[247,253–255]. Histone variants are involved in several specialized cellular functions, such as H2A.X in DNA repair or CENP-A in kinetochore assembly[256,257]. In

conclusion, the incorporation of histone variants into nucleosomes represents another epigenetic mechanism to modify chromatin structure according to requirements of different cellular processes.

1.3.5 Long-range chromatin interactions

Epigenetic gene regulation is also mediated by the three-dimensional architecture of chromatin within the nucleus as it is reviewed in depth by Ling and Hoffman[258]. During interphase, the chromatin is spread out three-dimensionally into chromosomal territories in a highly organized manner, and it has become evident now that nuclear architecture and chromatin geography play a vital role in regulating gene expression in normal as well as in malignant cellular backgrounds[258–261]. Genes present on loops of DNA, which protrude from euchromatic parts of chromosomes, are localized to active chromatin areas where gene transcription happens[262]. This chromosomal looping allows distant sections of DNA from the same chromosome but also from different chromosomes to interact thereby modifying the expression of genes that locate faraway from each other[258]. Additionally, recombination and genomic rearrangements are also facilitated by the proximity of these loops[263–265].

A prostate cancer-relevant example here is the gene fusion of the androgen-stimulated gene *TMPRSS2* and *ERG*, which encodes for a transcription factor. Both genes are located 3,000,000 bp apart on human chromosome 21q22.2 and their fusion is found in ≈ 50 % of prostate cancers[266]. The fusion of the 5' untranslated region of *TMPRSS2* to *ERG* results in androgen-regulated overexpression of ERG, which is thought to be sufficient for the initiation of prostate cancer[266,267]. Importantly, is has been shown that the androgen receptor induces chromosomal movements, which bring together the *TMPRSS2* and *ERG* genes facilitating their fusion[268]. As a consequence of ERG overexpression in *TMPRSS2:ERG* fusion-positive prostate cancer, *EZH2* is upregulated as it is a target gene of ERG[269]. This highlights the dramatic consequences of *TMPRSS2:ERG* gene fusion contributing to transformation and cancer progression.

1.3.6 Cancer epigenomics and its link to genetics

In addition to genetic alterations detected in cancer, the epigenomic landscape undergoes extensive distortion, including a genome-wide loss of DNA methylation (hypomethylation), an increase in promoter CGI methylation, hypoacetylation of chromatin, and aberrant changes in nucleosome occupancy as well as in histone modification[225,270]. These epigenetic changes result in a global deregulation of gene expression, which also concerns the expression of epigenetic regulators delineated above. Relating to this, Kanwal *et al.* compiled a plethora of epigenetic regulators that are deregulated in various cancer types in their introductory book chapter on cancer epigenomics[170].

While the genetic origin of cancer is commonly accepted, also epigenetic alterations are increasingly considered as key initiating events in several cancer types[168]. Like genetic mutations, epimutations can lead to chromosomal instability, inactivation of tumour suppressors and activation of oncogenes contributing to tumourigenesis[168,225,271]. Furthermore, epigenetic mechanisms are able to cause genetic mutations. Methylcytosines in CpGs, for instance, are regarded as hot spots for transitional mutations, which can destabilize gene structure and function[272–274]. It is therefore suggested that genetic and epigenetic aberrations intertwine and cooperate during tumourigenesis[271]. However, the fact that epigenetic aberrations occur early in cancer development and, unlike genetic mutations, are potentially reversible, makes epigenetic therapy a promising and relevant approach to fight cancer[168,275].

1.4 Aims of this study

Seeking for factors that are functionally relevant for centrosome aberrations in cancer, our group identified LGALS3BP interacting with centrosomal components within a protein-protein interaction network among centrosomal and cell cycle-regulatory proteins by using tandem affinity purification combined with mass spectrometry analysis (TAP-MS). It was quite surprising, though, to detect LGALS3BP, a secreted protein with only extracellular functions reported so far, within a centrosomal context. As LGALS3BP deregulation is detected in several cancer types and centrosomal aberrations in cancer are implicated in chromosomal instability, a cancer hallmark, the

aim of the project was to molecularly and functionally characterize the role of LGALS3BP for the human centrosome.

This aim has been addressed by initial validation studies on LGALS3BP localization to centrosomes via immunofluorescence microscopy analysis of endogenous as well as exogenously induced LGALS3BP expression. In the following, LGALS3BP function at centrosomes was examined by knockdown as well as overexpression studies. Additionally, LGALS3BP interacting proteins as well as known centrosomal regulators were included in this functional examination and possible upstream regulators, such as kinases targeting LGALS3BP, were determined. To further establish LGALS3BP deregulation in cancer, relevant transcriptional regulators, which are misexpressed in cancer as well, were examined in this context. Finally, this study aimed at correlating LGALS3BP deregulation and centrosome abnormalities in cancer, which might allow pharmaceutical intervention in the future.

2. Materials and Methods

2.1 Materials

2.1.1 Cell lines

Table 1: Human cell lines
DMEM – Dulbecco's modified Eagle's medium, K-SFM – keratinocyte serum-free medium, FCS – fetal calf serum, HS – horse serum, HI – human insulin, CT – cholera toxin, HC – hydrocortisone, BPE - bovine pituitary extract, EGF – epidermal growth factor, ATCC – American Type Culture Collection

Cell line	Culture medium	Source
U2OS	DMEM 1 g/l D-glucose, 10 % FCS, 1 % L-glutamine	ATCC
U2OS-GFP-Centrin2	DMEM 1 g/l D-glucose, 10 % FCS, 1 % L-glutamine	Duensing, S.
RWPE-1	K-SFM, 50 µg/ml BPE, 5 ng/ml EGF	ATCC
PC-3	RPMI, 10 % FCS	ATCC
LNCaP	RPMI, 10 % FCS	ATCC
DU-145	RPMI, 10 % FCS	ATCC
VCaP	DMEM 4.5 g/l D-glucose, 10 % FCS, 1 % L-glutamine	ATCC
SK-BR-3	McCoy's 5A, 10 % FCS	ATCC
MCF-10A	DMEM/F12 phenol red-free, 5 % HS, 10 µg/ml HI, 100 ng/ml CT, 500 ng/ml HC, 20 ng/ml EGF	ATCC
HEK293 and HEK293T	DMEM 4.5 g/l D-glucose, 10 % FCS, 1 % L-glutamine	ATCC
FlpIn TRex 293	DMEM 4.5 g/l D-glucose, 10 % FCS, 1 % L-glutamine, 100 µg/ml zeocin, 15 µg/ml blasticidin	Invitrogen
FlpIn TRex 293, stably transfected	DMEM 4.5 g/l D-glucose, 10 % FCS, 1 % L-glutamine, 100 µg/ml hygromycin, 15 µg/ml blasticidin	

Table 2: Bacterial cell lines

Cell line	Culture medium	Source
Top10	LB medium	Invitrogen
DB3.1	LB medium	Life Technologies

2.1.2 Antibodies

Table 3: Primary antibodies
Commercial and non-commercial (NC) monoclonal (MC) and polyclonal (PC) antibodies applied in immunofluorescence microscopy (IF) and Western blotting (WB)

Name	Clone	Raised in/ clonality	Provider	Catalogue #	Application
Anti-acetylated α-tubulin	6-11B-1	Mouse MC	Sigma	T7451	IF
Anti-BRD4		rabbit PC	Abcam	ab75898	WB
Anti-CBS		rabbit PC	Eurogentec	NC	WB
Anti-Centrin2	20H5	mouse MC	Salisbury[276]		IF
Anti-Centrin2		rabbit PC	Santa Cruz	sc-27793-R	IF
Anti-Centrobin		rabbit PC	Sigma	HPA023321	IF
Anti-CEP135		rabbit PC	Abcam	ab750025	IF
Anti-C-Nap1 (CEP250)		rabbit PC	ProteinTech	14498-1-AP	IF, WB
Anti-CPAP (CENPJ)	5D5	mouse MC	Abnova	H00055835-M01	IF
Anti-FLAG	M2	mouse MC	Sigma-Aldrich	F3165	IF, WB
Anti-FLAG		rabbit PC	Sigma-Aldrich	F7425	IF, WB
Anti-GFP		mouse MC	Roche	11814460001	IF
Anti-glutamylated α- and β-tubulin	GT335	mouse MC	Enzo	ALX-804-885	IF
Anti-LGALS3BP	12D4	mouse MC	Laferté *et al.*[277]	NC	IF
Anti-LGALS3BP		rabbit PC	Sigma-Aldrich	HPA000554	WB
Anti-living colours		rabbit PC	Clontech	632377	WB
Anti-MAGED2		mouse MC	Abcam	ab56805	IF, WB
Anti-myc	9E10	mouse MC	Upstate	05-419	IF, WB
Anti-myc		rabbit PC	Upstate	06-549	IF, WB
Anti-Pericentrin		rabbit PC	Covance	PRB-432C	IF

Anti-SAS6	91.390.21	mouse MC	Santa Cruz	sc-81431	IF
Anti-STAT1		rabbit PC	Cell Signalling	#9172	WB
Anti-TUBGCP3		rabbit PC	Eurogentec	NC	WB
Anti-β-actin	AC-15	mouse MC	Sigma-Aldrich	A5441	WB
Anti-γ-tubulin	TU-30	mouse MC	Abcam	ab27074	IF
Anti-γ-tubulin		rabbit PC	Sigma-Aldrich	T5192	IF

Table 4: Secondary antibodies
Polyclonal secondary antibodies used in immunofluorescence microscopy (IF) and Western blotting (WB)

Name	Raised in	Provider	Catalogue #	Application
Alexa Fluor 488 anti-mouse IgG (H+L)	goat	Life Technologies	A11029	IF
Alexa Fluor 488 anti-rabbit IgG (H+L)	goat	Life Technologies	A11034	IF
Alexa Fluor 594 anti-mouse IgG (H+L)	goat	Life Technologies	A11032	IF
Alexa Fluor 594 anti-rabbit IgG (H+L)	goat	Life Technologies	A11037	IF
Alexa Fluor 647 anti-rabbit IgG (H+L)	goat	Life Technologies	A21244	IF
HRPO anti-mouse IgG (H+L)	donkey	Dianova	715-035-150	WB
HRPO anti-rabbit IgG (H+L)	goat	Dianova	111-035-144	WB

2.1.3 Oligonucleotides

Table 5: Oligonucleotides
Applied siRNAs, shRNAs and primers for RNAi, qPCR and cloning LGALS3BP and STAT1 promoters into pGL3-E luciferase reporter vector

Name	Sequence (5'-3')		Provider	Application
Custom 3'UTR *LGALS3BP* duplex siRNA #1	sense antisense	AGAAAUUACUGGAAGGCUUUU AAGCCUUCCAGUAAUUUCUUU	Thermo Scientific	RNAi
Custom 3'UTR *LGALS3BP* duplex siRNA #2	sense antisense	GGUGGUGAGAACCGGAGAAUU UUCUCCGGUUCUCACCACCUU	Thermo Scientific	RNAi
siGENOME *EZH2* siRNA	SMARTpool, mix of 4 siRNAs (Catalogue # M-004218-03-0005)		Thermo Scientific	RNAi

siGENOME *CEP55* siRNA	SMARTpool, mix of 4 siRNAs (Catalogue # M-006893-01-0005)		Thermo Scientific	RNAi
siGENOME *CEP250* siRNA	SMARTpool, mix of 4 siRNAs (Catalogue # M-012364-01-0005)		Thermo Scientific	RNAi
siGENOME *LGALS3BP* siRNA	SMARTpool, mix of 4 siRNAs (Catalogue # M-008016-00-0005)		Thermo Scientific	RNAi
siGENOME *MAGED2* siRNA	SMARTpool, mix of 4 siRNAs (Catalogue # M-017284-00-0005)		Thermo Scientific	RNAi
siGENOME non-targeting siRNA pool #2	mix of 4 siRNAs (Catalogue # D-001206-14)		Thermo Scientific	RNAi
siGENOME *TUBGCP3* siRNA	SMARTpool, mix of 4 siRNAs (Catalogue # M-018323-01-0005)		Thermo Scientific	RNAi
shC2	GACACTATGGAAACACCAG		Schweiger[278]	RNAi
shE1	GCGGGAGCAGGAGCGAAGA		Schweiger[278]	RNAi
shGFP	GCAAGCTGACCCTGAAGTTC		Schweiger[278]	RNAi
BRD4-both primer	forward reverse	AACCTGGCGTTTCCACGGTA GCCTGCACAGGAGGAGGATT	Invitrogen	qPCR
BRD4-long primer	forward reverse	GAAATGAAGCCTGTGGATGTCG TCGGCTCCTGTTTCTGTTTGTC	Invitrogen	qPCR
GAPDH primer	forward reverse	CATTTCCTGGTATGACAACGA TCCTCTTGTGCTCTTGCT	Invitrogen	qPCR
HPRT1 primer	forward reverse	AGGAAAGCAAAGTCTGCATTG GGTGGAGATGATCTCTCAACT	Invitrogen	qPCR
LGALS3BP primer	forward reverse	AGAGAGACGCTGGTGTGGTCT GCTGGCTGTCAAAGATCTGG	Invitrogen	qPCR
STAT1 primer	forward reverse	GCATGAAATCAAGAGCCTGGAA CCACACCATTGGTCTCGTGTT	Invitrogen	qPCR
LGALS3BP primer	forward reverse	TTTAAGCTTCTATGTGCAAACAGGGAGG TTTAGATCTTAGGAGAGTGGCCACAG	Invitrogen	cloning into pGL3-E luciferase reporter vector
STAT1 primer	forward reverse	TTTAAGCTTGCTCAGCCAATTAGACGC TTTAGATCTGACGTCGCCAAATCTGTC	Invitrogen	

2.1.4 Vectors

Table 6: Vectors
The vectors phRL-TK and pGL3-Enhancer were kindly provided to Prof. Dr. Dr. med. Michal-Ruth Schweiger's group by PD Dr. Sylvia Krobitsch's group.

Vector	Backbone	Source	Application
pSUPER.retro.puro		Schweiger[278]	Cloning of shRNAs
pcDNA3-N-TAP	pcDNA3	Gingras, A.-C.	Destination vector, Gateway cloning

pcDNA5/FRT/TO-NTAP	pcDNA5/FRT/TO	Lab stock	Destination vector, Gateway cloning
pc-myc-CMV-D12	pCL	RZPD	Destination vector, Gateway cloning
pdEYFP-gen		DKFZ	Destination vector, Gateway cloning
pFLAG-CMV-D11	pCL	RZPD	Destination vector, Gateway cloning
pDONR221		Invitrogen	Donor vector, Gateway cloning
pDONR223		Invitrogen	Donor vector, Gateway cloning
pGL3-E-LGALS3BPprom	pGL3-Enhancer	Wunderlich, A.	Dual-Luciferase Reporter Assay
pGL3-Enhancer		Promega	Dual-Luciferase Reporter Assay, cloning gene promoters
pGL3-E-STAT1prom	pGL3-Enhancer	Wunderlich, A.	Dual-Luciferase Reporter Assay
phRL-TK		Promega	Dual-Luciferase Reporter Assay, normalization
pDONR221-CEP250_stop	pDONR221	Lab stock	Entry clone, Gateway cloning
pDONR221-TUBGCP3_stop	pDONR221	Lab stock	Entry clone, Gateway cloning
pDONR223-LGALS3BP	pDONR223	Lab stock	Entry clone, Gateway cloning
pDONR223-LGALS3BP_stop	pDONR223	Lab stock	Entry clone, Gateway cloning
CEP250-N-FLAG	pFLAG-CMV-D11	Lab stock	Expression clone, transfection
EGFP-N-FLAG	pFLAG-CMV-D11	Lab stock	Expression clone, transfection
EGFP-N-TAP	pcDNA5/FRT/TO-N-TAP	Lab stock	Expression clone, transfection
EGFP-YFP-C	pdEYFP-gen	Lab stock	Expression clone, transfection
LGALS3BP–YFP-C	pdEYFP-gen	Lab stock	Expression clone, transfection
LGALS3BP-N-FLAG	pFLAG-CMV-D11	Lab stock	Expression clone, transfection
LGALS3BP-N-myc	pcMyc-CMY-D12	Lab stock	Expression clone, transfection
LGALS3BP-N-TAP	pcDNA5/FRT/TO-N-TAP	Lab stock	Expression clone, transfection
PLK4-N-TAP	pcDNA3/FRT/TO-N-TAP	Lab stock	Expression clone, transfection
TUBGCP3-N-FLAG	pFLAG-CMV-D11	Lab stock	Expression clone, transfection

pOG44	Invitrogen	Flp recombinase expression vector, generating stable cell lines

2.1.5 Chemicals

Name	Provider	Application
Agarose	Invitrogen	Agarose gel electrophoresis
Ethidium bromide	AppliChem	Agarose gel electrophoresis
Acetic acid	Merck	Buffer component
Bromphenolblue	AppliChem	Buffer component
Dithiothreitol (DTT)	AppliChem	Buffer component
Ethylene glycol tetraacetic acid (EGTA)	AppliChem	Buffer component
Ethylenediaminetetraacetic acid (EDTA)	Roth	Buffer component
Glycerol	Merck	Buffer component
Glycine	Merck	Buffer component
$MgCl_2$	Merck	Buffer component
NaCl	Roth	Buffer component
Nonidet P40 (NP-40)	AppliChem	Buffer component
PIPES	Sigma	Buffer component
Sodium dodecyl sulfate (SDS)	Roth	Buffer component
Tris-base	Merck	Buffer component
Tris-HCl	Merck	Buffer component
Triton-X 100	Sigma	Buffer component
Tween-20	Sigma	Buffer component
Xylencyanol FF	AppliChem	Buffer component
β-Mercaptoethanol	Merck	Buffer component

Blasticidin	Invitrogen	Cell culture
Dimethylsulfoxid (DMSO)	Merck	Cell culture
Hygromycin B	Invitrogen	Cell culture
Nocodazole	Sigma	Cell culture
poly L lysine	Sigma	Cell culture
Tetracycline	Invitrogen	Cell culture
Zeocin	Invitrogen	Cell culture
MeOH	Merck	Fixation, buffer component
Paraformaldehyde (PFA)	AppliChem	Fixation
DAPI (diamidino-2-phenylindol-dihydrochlorid)	AppliChem	Immunofluorescence microscopy
Mowiol 4-88	Calbiochem	Immunofluorescence microscopy
p-Phenylendiamine (PDA)	Sigma	Immunofluorescence microscopy
Calyculin A	Calbiochem	Phosphatase inhibitor
Na_3VO_4	AppliChem	Phosphatase inhibitor
NaF	AppliChem	Phosphatase inhibitor
Okadaic acid	Calbiochem	Phosphatase inhibitor
β-glycerophosphate	AppliChem	Phosphatase inhibitor
Aprotinin	Sigma	Protease inhibitor
Leupeptin	Sigma	Protease inhibitor
Pefabloc SC	Roche	Protease inhibitor
Pepstatin A	Sigma	Protease inhibitor
Acrylamide/Bis solution 37,5:1	Serva	SDS-PAGE
Ammonium persulfate (APS)	Merck	SDS-PAGE
Tetramethylethylenediamine (TEMED)	Invitrogen	SDS-PAGE

Ampicillin	AppliChem	Selecting resistant bacteria
Concanamycin A	Sigma	Selecting resistant bacteria
Spectinomycin	Sigma	Selecting resistant bacteria
Ponceau S	Sigma	Western blotting

2.1.6 Kits and reagents

Table 7: Kits and reagents applied in this study

Name	**Provider**	**Application**
1 kb DNA Ladder	Invitrogen	Agarose gel electrophoresis
1 kb Plus DNA Ladder	Invitrogen	Agarose gel electrophoresis
Dual-Luciferase Reporter Assay System	Promega	Analysis of promoter activity
LB agar medium	MP Biomedicals	Bacterial cell culture
LB medium	MP Biomedicals	Bacterial cell culture
dNTPs	Bioline	cDNA synthesis
random primers	Promega	cDNA synthesis
Nuclease-free water	Promega	cDNA synthesis, qPCR
RNase H	Promega	cDNA synthesis
RNasin	Promega	cDNA synthesis
SuperScript II Reverse Transcriptase Kit	Invitrogen	cDNA synthesis
Bovine pituitary extract (BPE)	Sigma	Cell culture
Cholera toxin (CT)	Sigma	Cell culture
DharmaFECT 1	Thermo Fisher Scientific	Cell culture
DMEM	Gibco	Cell culture
DMEM/F12	Gibco	Cell culture

Dulbecco's PBS without Ca^{2+} and Mg^{2+}, sterile	PAA Cell Culture Company	Cell culture
Effectene Transfection Reagent Kit	Qiagen	Cell culture
Epidermal growth factor	Sigma	Cell culture
Fetal calf serum	Biochrom AG	Cell culture
Horse serum	Gibco	Cell culture
Human insulin	Sigma	Cell culture
Hydrocortisone	Sigma	Cell culture
K-SFM	Invitrogen	Cell culture
McCoy's 5A	Gibco	Cell culture
Recombinant human INFγ	PeproTech	Cell culture
RPMI	Gibco	Cell culture
Trypsin-EDTA 10x	Gibco	Cell culture
X-tremeGENE9	Roche	Cell culture
LR Clonase II enzyme mix	Invitrogen	Cloning
Bovine serum albumin (BSA)	Sigma-Aldrich	Immunofluorescence staining, INFγ-treatment control
EndoFree Plasmid Maxi Kit	Qiagen	Plasmid DNA preparation
Plasmid Mini Kit	Qiagen	Plasmid DNA preparation
GoTaq qPCR Master Mix	Promega	qPCR
Quick-RNA MicroPrep Kit	Zymo Research	RNA preparation
PageRuler Prestained Protein Ladder	Fermentas	SDS-PAGE
In Situ Cell Death Detection Kit, fluorescein	Roche	TUNEL assay
cOmplete Mini, EDTA-free protease inhibitor cocktail	Roche	Western blotting
Western Lightning Plus-ECL	PerkinElmer	Western blotting

2.1.7 Solutions and buffers

Table 8: Solutions and buffers

Buffer/solution	Composition
DNA loading buffer, 6x	0.25 % Bromphenolblue, 0.25 % Xylencyanol FF, 30 % Glycerol
Extraction buffer	5mM PIPES, 2mM EGTA, 0.6 % Triton X 100
Freezing medium	90 % FCS, 10 % DMSO
Freezing medium (MCF-10A)	90 % horse serum, 10 % DMSO
Lysis buffer A	125 mM NaCl, 50 mM Tris-HCl, 1.5 mM $MgCl_2$, 1 mM DTT, 5 % Glycerol, 0.2 % NP-40, 2 µg/ml Aprotinin, 2 µg/ml Leupeptin, 1 mM Pefabloc, 1 µg/ml Pepstatin A, 25 mM NaF, 1 mM Na_3VO_4, 5 nM okadaic acid, 5 nM Calyculin A, 50 mM β-glycerophosphate, 1 mM EDTA pH 8.0
Lysis buffer B for CIP	100 mM NaCl, 50 mM Tris-HCl, 10 mM $MgCl_2$, 1 mM DTT, 2 µg/ml Aprotinin, 2 µg/ml Leupeptin, 1 mM Pefablock, 1 µg/ml Pepstatin A
Main gel buffer pH 8.8	1.5 M Tris, 0.4 % SDS
Non-fat dry milk, 5 %	2.5 g non-fat dry milk powder in 50 ml PBS-Tween
Non-fat dry milk, 5 % with protease inhibitors	1 cOmplete Mini protease inhibitor cocktail tablet dissolved in 10 ml of 5 % non-fat dry milk
Non-fat dry milk, 5 % with protease and phosphatase inhibitors	25 mM NaF, 1 mM Na_3VO_4, 5 nM okadaic acid, 5 nM Calyculin A, 50 mM β-glycerophosphate, 1 mM EDTA pH 8.0, 1 cOmplete Mini protease inhibitor cocktail tablet dissolved in 10 ml of 5 % non-fat dry milk
PBS pH 7.4, 10x	1.37 M NaCl, 14.7 mM KH_2PO_4, 78.1 mM Na_2HPO_4, 26.8 mM KCl
PBS-T	1x PBS, 0.003 % Triton-X 100
PBS-Tween	1x PBS, 0.05 % Tween-20
Ponceau S solution	0.1 % Ponceau S, 5 % Acetic acid
SDS running buffer, 10x	250 mM Tris-base, 2.5 M Glycine, 1 % SDS
SDS sample buffer, 2x	0.125 M Tris pH 6.8, 4 % SDS, 20 % Glycerol, 10 % β-Mercaptoethanol, 0.004 % Bromphenolblue
Stacking gel buffer pH 6.8	0.5 M Tris, 0.4 % SDS
TAE running buffer pH 8.5, 10x	0.4 M Tris-base, 0.01 M EDTA, 0.2 M Acetic acid
Western transfer buffer	19.3 mM Tris-HCl, 288 mM Glycine, 20 % MeOH

2.2 Methods

2.2.1 Cloning

Gateway Cloning

The Gateway Technology (Invitrogen) was applied according to the manufacturer's instructions to clone compatible entry clones into destination vectors via the LR recombination reaction catalysed by the LR Clonase II enzyme mix (Invitrogen). The LR reaction mixture was transformed into *E. coli* Top10 cells and expression clones were selected by plating on LB agar containing 50 µg/ml ampicillin. A successful cloning was evaluated by restriction digestion of the expression clones.

Transformation of bacteria via electroporation

For transformation 1-2 µl of plasmid DNA were mixed with 50 µl of the required *E. coli* strain (Top10 for entry and expression clones, DB3.1 for destination vectors) and transferred into an electroporation cuvette (0.1 cm electrode). Cuvettes were then loaded into an electroporator and electroporation was carried out at 25 µF, 200 Ω and 1.25 kV for 2 s. Thereafter, bacteria were resuspended in 300 µl LB medium, transferred into an appropriate Eppendorf vial and incubated for 30 min at 37 °C at 400 rpm in a thermomixer. Bacteria were then plated on LB agar plates supplied with the corresponding antibiotics and cultured over night at 37 °C.

Plasmid preparation

For plasmid preparations, colonies from overnight cultures were picked from agar plates and inoculated into LB medium provided with the respective antibiotics. After shaking overnight at 37 °C, small volumes (≈3 ml) were prepared with the Plasmid Mini Kit (Qiagen) for plasmid DNA amounts up to 20 µg and larger volumes (150 ml) were prepared with the EndoFree Plasmid Maxi Kit (Qiagen) for endotoxin-free plasmid DNA amounts up to 500 µg. Subsequently, the plasmid DNA was verified by restriction digestion.

Restriction digestion

Restriction digestion was performed with appropriate restriction enzymes (NEB) to verify plasmid DNA. Suitable restriction enzymes as well as expected bands after digestion were computed with the Vector NTI Advance software (Invitrogen). The following restriction digestion reaction mixture was applied:

- 2 µl plasmid DNA
- 0.5 µl restriction enzyme
- 2 µl 10 x NEB buffer
- (2 µl 10 x BSA)
- dH_2O up to 20 µl

The reaction mixture was incubated in a thermomixer (Eppendorf) at 37 °C shaking at 450 rpm for 2 h and subsequently analysed by agarose gel electrophoresis.

Agarose gel electrophoresis

Agarose gel electrophoresis was performed to separate DNA fragments by length and to confirm expected DNA bands after restriction digestion. 0.8 % agarose gels (dissolved in 1x TAE running buffer) containing 1 µg/ml ethidium bromide were prepared in gel electrophoresis chambers (built by the institute's workshop) and doused with 1x TAE running buffer before being loaded with samples in 6x DNA loading buffer. The 1 kb DNA Ladder and 1 kb Plus DNA Ladder (Invitrogen) served as a size marker. Electrophoresis was carried out at 80 mV with the PowerPAC Basic (BioRad) power supply. Gels were then documented with the AlphaImager system (AlphaInnotech).

2.2.2 Cell culture

Culturing and passaging of human cells

Cell lines were cultured in cell culture flasks (TPP) containing their respective medium (Table 1 on page 23) at 37 °C, 5 % CO_2 and 90 % humidity. Cell culture reagents (PBS, trypsin-EDTA, culturing media) were sterile und pre-warmed to 37 °C before

application to the cells. The culturing medium was refreshed twice a week and cells were split as they reached 80-90 % confluency.

Splitting was performed by rinsing the cells with PBS followed by incubation with 0.05 % trypsin-EDTA at 37 °C until all cells detached. Subsequently, the cells were resuspended in culturing medium (more than 5x greater volume than trypsin-EDTA) and a suitable volume of cell suspension was transferred into a new cell culture flask, which was filled with fresh medium to the final volume.

Freezing and thawing of human cells

For cryopreservation of cell aliquots, cells were detached by trypsinization and collected in a 15 ml centrifuge tube. Cells were then pelleted at room temperature at 1,200 rpm (Eppendorf Centrifuge 5810R) and subsequently washed in pre-warmed PBS and pelleted again. Finally, cells were resuspended in freezing medium and 1 ml aliquots were transferred into cryovials. The aliquots were slowly frozen at -80 °C for one day and then stored in liquid nitrogen.

Thawing of cell aliquots was performed shortly in a water bath at 37 °C. The cell suspension was subsequently transferred into a cell culture flask and culturing medium was added to the final volume.

Seeding of human adherent cells

Adherent cells were detached from the bottom of the cell culture flask by trypsinization and resuspended in corresponding culturing medium. The cell density was determined with a hemocytometer (Laboroptik) so that the cell suspension could be diluted with culturing medium to the desired cell number in a final volume.

If excess peel-off of cells for immunofluorescence microscopy samples should be avoided, cells were settled on poly-L-lysine (PLL)-coated glass cover slips. PLL-coated cover slips were prepared by dousing the clean glass cover slips for 15 min in a sterile 100 µg/ml PLL solution followed by drying at ambient temperature. The PLL solution could be reused up to five times and stored at -20 °C. The coated cover slips could be kept at -20 °C for further application.

Transient transfection of human cells

HEK293T and U2OS cells were transiently transfected with endotoxin-free DNA using the Effectene Transfection Reagent Kit (Qiagen) according to the manufacturer's instructions. In short, cells were seeded in 6-well plates (TPP) one day before transfection so that they reach 40-80 % confluency the next day. Per 6-well, 0.4 µg DNA in a sterile reaction tube were diluted with the DNA-condensation buffer EC to a final volume of 100 µl. Next, 3.2 µl of Enhancer solution were added and briefly vortexed followed by 2 – 5 min incubation at ambient temperature. 10 µl of Effectene transfection reagent were then added to the DNA-Enhancer mixture and mixed by pipetting up and down. To allow transfection complex formation, the samples were incubated for 5 – 10 min at room temperature. In the meantime, the culturing medium was aspired from the cells and replaced by 1,600 µl of fresh culturing medium. Subsequently, the transfection solution was mixed with 600 µl of culturing medium and added dropwise to the cells. Cells were harvested after 24 – 96 h.

Stable transfection of human cells

The day before transfection, 3 x 10^5 FlpIn TRex 293 cells of a low passage number were seeded per well of 6-well plate (TPP). On the next day, the culturing medium was replaced by medium without antibiotics 1 – 3 h before transfection. For transfection, 100 µl serum-free DMEM containing 0.1 µg of the transgene and 0.9 µg of the recombinase-encoding vector (pOG44) were mixed with 100 µl serum-free DMEM containing 3 µg PEI and incubated for 15 min at room temperature. Thereafter, the mixture was added dropwise to the cells. 24 h after transfection, the medium was refreshed with antibiotic-free DMEM/10 %. The next day, cells were transferred into a 25 cm^2 cell culture flask (TPP) and selection for stably transfected cells was initiated after the cells have settled down. For this purpose, the culturing medium was exchanged by DMEM/10 % FCS containing selection antibiotics (15 µg/ml blasticidin and 100 µg/ml hygromycin B). Within the next two weeks, dead untransfected cells were removed by exchanging the selective culturing medium every 2 – 3 days. Colonies of stably transfected cells, which appeared approximately 10 days after transfection, were further expanded and cryopreserved. Transgene expression in FlpIn TRex 293

cells could be induced by 1 µg/ml tetracycline. A proper transgene expression was validated by immunofluorescence microscopy and immunoblotting.

RNA interference

One day before transfection, a proper number of cells were seeded in 6-well plates (TPP) depending on the cell line and duration of RNAi. To transfect siRNAs (Table 5), the DharmaFECT 1 transfection reagent (Thermo Fisher Scientific) was used according to the manufacturer's instructions. For this purpose, 2 µl of a 20 µM siRNA stock solution were mixed with 198 µl of serum-free RPMI medium without antibiotics in a falcon (Sarstedt) and 2 – 4 µl of DharmaFECT reagent were mixed with RPMI to a final volume of 200 µl in another falcon. After incubation for 5 min at room temperature, the contents of both falcons were combined and incubated for 20 min at room temperature followed by adding 1.6 ml of the respective culturing medium. The culturing medium was then removed from the wells und replaced by the transfection complex mix. Cells were harvested after 24 – 96 h.

The X-tremeGENE9 transfection reagent (Roche) was applied to transfect HEK293T cells with shRNAs (Table 5) following the manufacturer's instructions. The cells were seeded depending on the plating format (Table 9) one day before transfection. On the next day, the culturing medium was replaced by medium without antibiotics. The X-tremeGENE9 transfection reagent was diluted in serum-free medium without antibiotics, incubated for 5 min at ambient temperature and then added to the shRNA. After another 15 min of incubation the transfection complex mixture was added dropwise to the cells and distributed equally by gently swivelling the cell culture plate. The cells were kept in the incubator until harvest after 72 h.

Table 9: Transfection with X-tremeGENE9 in certain plating formats

Plating format	Seeded cells	DMEM, +FCS, -AB [µl]	DNA [ng]	DMEM, -FCS, -AB [µl]	X-tremeGENE 9 [µl]
96-well	1×10^4	66.7	33.3	3.23	0.1
24-well	8×10^4	410	205	19.9	0.62
6-well	5×10^5	2,000	1,000	97	3

If cells should be stimulated with INFγ for 48 h additionally to the knockdown, they were treated with 100 U INFγ 24 h after transfection. Treatment with 0.1 % BSA served as a negative control in this setup.

2.2.3 SDS-PAGE

To separate proteins in cell lysates by molecular weight, SDS-PAGE was performed according to Laemmli[279]. Cell pellets were resuspended in 2x SDS sample buffer and denatured for 10 min at 99 °C in a thermomixer (Eppendorf).

Table 10: Composition of polyacrylamide gels

	Stacking gel	Main gel		
		7.5 %	10 %	12.5 %
dH_2O	3 ml	4.45 ml	3.5 ml	2.46 ml
30 % Acrylamide/Bis solution 37,5:1	0.6 ml	3.11 ml	4.15 ml	5.19 ml
Stacking gel buffer	1.3 ml	–	–	–
Main gel buffer	–	4.6 ml	4.6 ml	4.6 ml
TEMED	4 µl	10 µl	10 µl	10 µl
10 % APS	58 µl	83 µl	83 µl	83 µl

Subsequently, samples were chilled on ice and either stored at -20 °C or loaded on a polyacrylamide gel of a chosen composition (Table 10). The PageRuler Prestained Protein Ladder (Fermentas) was applied as a molecular weight marker.

The electrophoretic separation of proteins was carried out in a gel electrophoresis chamber (EMBL) in 1x SDS running buffer at 25 mA supplied by a PowerPac Basic (BioRad).

2.2.4 Western blotting

To detect proteins of a certain molecular weight, immunoblotting was performed after the principles of Towbin[280]. Briefly, proteins were transferred electrophoretically from a polyacrylamide gel onto a Whatman Protran nitrocellulose membrane (GE

Healthcare Life Sciences, 0.45 µm pore size) for ≈ 2 h at 400 mA using a wet-tank blotting system (Hoefer TE 22, Amersham Biosciences) filled with western transfer buffer. The transfer of proteins was verified by staining the membrane reversibly with Ponceau S solution. After destaining with PBS-Tween buffer, the membrane was blocked with 5 % non-fat dry milk (in PBS-Tween). Subsequently, the primary antibody was incubated for at least 1 h followed by incubation with the HRPO-coupled secondary antibody for maximum 45 min. Antibodies were diluted in 5 % non-fat dry milk and excess amounts were washed off with PBS-Tween between the incubation steps. The Western Lightning Plus-ECL reagent (PerkinElmer) was applied to detect chemiluminescence of a labelled protein on an X-ray film (Fuji).

2.2.5 Mitotic index determination

The mitotic index was determined by immunofluorescence microscopy analysis as ratio of mitotic cells given by positive phospho-histone H3-labelling and total cell number acquired by DAPI-staining. Statistical analysis was carried out by chi-squared test compared to the respective negative control.

2.2.6 TUNEL assay and apoptotic index determination

MeOH-fixed cells on glass cover slips were rehydrated and permeabilized for 10 min in PBS-T buffer. To label terminal DNA-strand breaks of apoptotic cells, a TUNEL assay was performed. For this purpose, the *In Situ* Cell Death Detection Kit (Roche) was used following manufacturer's instructions. Briefly, 50 µl of the provided enzyme solution (terminal deoxynucleotidyl transferase) was mixed with 450 µl of the label solution (fluorescein-coupled deoxyuridine triphosphate). 50 µl of this mix were applied to the cells, which were then incubated in a humidified chamber in the dark at 37 °C for 60 min. At the end, 10 µl of a 4 µg/ml DAPI stock solution were added to the cells for 1 min followed by washing the cover slips 4 x with PBS-T buffer. Cover slips were then mounted onto microscope slides by embedding them in Mowiol containing 2 mg/ml p-phenylenediamine (pda) followed by sealing the cover slips with nail varnish. Analysis was performed by immunofluorescence microscopy. The apoptotic index was then calculated as ratio of TUNEL-positive cells and total cell number acquired by

DAPI-staining. Statistics were performed by chi-squared test compared to negative control.

2.2.7 Microscopy

Pre-fixation extraction

Pre-fixation extraction was carried out before labelling endogenous LGALS3BP for immunofluorescence microscopy. For this purpose, cells grown on glass cover slips were incubated for 20 s in extraction buffer and immediately fixed with ice-cold MeOH.

Fixation

Cells grown on glass cover slips were either fixed directly with ice-cold MeOH for 5 min or with 4 % paraformaldehyde (PFA) solution for 15 min followed by MeOH-fixation. Cells in MeOH could be kept for storage at -20 °C.

Immunolabelling

After fixation, cells were rehydrated in PBS-T buffer for 15 min at ambient temperature. To reduce non-specific antibody binding at free aldehyde groups, cells fixed by combined PFA/MeOH-fixation were blocked for at least 30 min in PBS-T buffer containing 1 % BSA. Subsequently, cells were labelled with the primary antibody for at least 1 h at room temperature or overnight at 4 °C. Excess antibody was removed by washing the cover slips four times before incubation with the secondary antibody for maximum 45 min. To stain DNA, DAPI solution was added directly to the secondary antibody at 1 µg/ml final concentration for 1 min at the end followed by washing the cover slips four times. Antibody dilutions and washing steps were carried out with PBS-T (containing 0.1 % BSA for combined PFA/MeOH-fixed cells). Finally, cover slips were mounted onto microscope slides by embedding them in Mowiol containing 2 mg/ml p-phenylenediamine (pda) followed by sealing the cover slips with nail varnish.

Microscopy and image acquisition

Sample examination and microscopic quantifications were carried out with the AxioImager Z1 fluorescence microscope (Carl Zeiss Microscopy, Jena) using the following objectives:

- Zeiss Plan-Apochromat 20x/0.75
- Zeiss Plan Apochromat 63x/1.4 Oil DIC
- Zeiss Plan-Apochromat 100x/1.4 Oil Ph3

The AxioVision software (Carl Zeiss Imaging) was applied for microscope operation, image acquisition and data export.
The LSM700 confocal microscope (Carl Zeiss Microscopy) was used for colocalization studies with the following objectives:

- Zeiss EC Plan-Neofluar 40x/1.30 Oil DIC
- Zeiss Plan-Apochromat 63x/1.40 Oil DIC
- Zeiss Plan-Apochromat 100x/1.40 Oil DIC

Microscope operation, image acquisition and data export was performed with the ZEN software (Carl Zeiss Imaging).

Image analysis

Quantitative image analysis was performed with CellProfiler (determination of DNA contents via integrated DAPI intensities for examination of cell cycle distributions) and ImageJ (determination of relative protein levels in immunoblots via densitometry, total cell number given by DAPI-staining, immunofluorescence intensities at centrosomes, area of pericentriolar material and microtubule regrowth). The following ImageJ macros were written for a given purpose:

Determination of total cell number given by DAPI-staining (20x objective images)

```
setAutoThreshold("Default");
//run("Threshold...");
setAutoThreshold("Default dark");
run("Convert to Mask");
run("Watershed");
run("Analyze Particles...", "size=150-Infinity circularity=0.05-1.00 show=Nothing display include summarize");
```

Immunofluorescence intensities at centrosomes (63x objective images)

```
setAutoThreshold("Default");
//run("Threshold…");
setAutoThreshold("Default dark");
run("Create Selection", "");
run("Enlarge...", "enlarge=2");
run("Create Mask", "");
run("Set Measurements...", "area mean modal min integrated median display redirect=[image.zvi Ch2] decimal=0");
run("Analyze Particles...", "size=0-Infinity circularity=0.00-1.00 show=Outlines display exclude");
```

Area of pericentriolar material (63x objective images)

```
setAutoThreshold("Default");
//run("Threshold…");
setAutoThreshold("Default dark");
run("Convert to Mask");
setThreshold(255, 255);
run("Restore Selection");
run("Analyze Particles...", "size=25-300 circularity=0.30-1.00 show=Outlines display summarize");
```

The analysis of nucleus shapes in U2OS cells transfected simultaneously with siRNA pools targeting LGALS3BP as well as C-Nap1 and with non-targeting siRNA as a negative control was performed with the ImageJ software using the Shape_Descriptor1u plugin written by Chinga, G. Image analysis was performed on fluorescence micrographs of > 2,000 DAPI-stained nuclei per experiment, which were thresholded to obtain binary images of the nuclei. The area, form factor and roundness were then analysed. In this case, the form factor describes the boundary of nuclei and is calculated by:

$$form\ factor = \frac{4\pi \cdot area}{perimeter^2}$$

A form factor of 1 represents a perfect and smooth circle whilst lower values towards 0 indicate increasing boundary irregularities given by greater nucleus perimeters.

The roundness describes the circularity of a nucleus and is calculated by:

$$roundness = \frac{4 \cdot area}{\pi \cdot length^2}$$

A roundness value of 1 again represents a perfect circle whilst lower values towards 0 indicate increasing stretching of a nucleus given by elliptical shapes of greater length.

Within the experiment, nuclei with areas smaller than 1,000 pixels were excluded from analysis to eliminate the background of cell debris. Subsequently, the calculated form

descriptors were plotted against each other and against the nucleus area in scatter plots. No statistical analysis was performed due to the lack of replicates.

Image processing

Immunofluorescence micrographs as well as scanned X-ray films of immunoblots were processed with Adobe Photoshop CS5 by slight level regulation and contrast enhancement. Figures were prepared with Adobe Illustrator CS5.

2.2.8 Quantitative real-time PCR (qPCR)

Preparation of total RNA from cultured cells

RNA preparations were performed by Andrea Wunderlich using the Quick-RNA MicroPrep Kit (Zymo Research) according to the manufacturer's instructions.

cDNA synthesis

cDNA was synthesized by Andrea Wunderlich using the SuperScript II Reverse Transcriptase Kit (Invitrogen). 300 ng of total RNA were mixed with 250 ng of random primers, 1 µl of 10 mM dNTPs and added nuclease-free water to a final volume of 13 µl. The mixture was incubated for 5 min at 65 °C and chilled on ice afterwards. Subsequently, 4 µl of 5x first strand buffer, 1 µl of 0.1 M DTT, 1 µl RNasin (40 U/µl) and 1 µl of SuperScript II reverse transcriptase (200 U/µl) were added to the mixture and incubated successively for 5 min at 25 °C, 60 min at 50 °C and 15 min at 70 °C (PCR cycler PTC-100, MJ Research). To digest template RNA, 1 µl of RNase H (2 U/µl) was added and incubated for 30 min at 37 °C. Next, RNase H was inactivated by heat for 20 min at 65 °C and the remaining single-stranded cDNA was diluted in nuclease-free water to 5 ng/µl final concentration.

Quantitative real-time PCR

qPCR was performed by Andrea Wunderlich and data analysis as well as interpretation was done by me.

Per reaction, 5 ng of cDNA were mixed with each 0.75 µl of 5 µM forward and reverse primers (Table 5), 5 µl of 2x GoTaq qPCR Master Mix (Promega, containing BRYT Green

dye, GoTaq Hot Start DNA polymerase and dNTPs) and added nuclease-free water to a final volume of 10 µl. qPCR was carried out in absolute quantifications (standard curve) using the Fast Real-Time PCR system 7900HT (Applied Biosystems) under specific cycling conditions (Table 11).

Table 11: Cycling conditions for qPCR

Time	Temperature	
2 min	50 °C	
10 min	95 °C	
15 s	95 °C	40 cycles
1 min	60 °C	
15 s	95 °C	
15 s	60 °C	
15 s	95 °C	

Results given by C_T values were interpreted using the $\Delta\Delta C_T$ method following Applied Biosystems' instructions in the manual. First, means and standard deviations of the replicate measurements were calculated. Next, ΔC_T values were calculated by:

$$\Delta C_T = C_{T\ target} - C_{T\ reference}$$

GAPDH and *HPRT1* were used as reference genes in this study. The standard deviation *s* of the ΔC_T values is calculated using the formula:

$$s = \sqrt{s_{target}^2 + s_{reference}^2}$$

The $\Delta\Delta C_T$ value is calculated by:

$$\Delta\Delta C_T = \Delta C_{T\ treatment} - \Delta C_{T\ control}$$

The standard deviation of ΔC_T was kept for $\Delta\Delta C_T$ because $\Delta\Delta C_T$ involves the subtraction of $\Delta C_{T\ control}$ and thus represents a subtraction of an arbitrary constant. Subsequently, fold changes (FC) were calculated out of $\Delta\Delta C_T$ values using the formula:

$$FC = 2^{-\Delta\Delta C_T}$$

To better represent up- and downregulation of gene expression in a bar chart, data were $\log_2$-transformed. A two-tailed *t*-test was applied on the $\Delta\Delta C_T$ values to test for significance as compared to the respective controls.

2.2.9 Gene expression analysis and methylation profiling of prostate cancers

The experiments were performed by Börno *et al.* and results presented in this thesis originated from their data set. The experimental methodology is briefly summarized in the following according to Börno *et al.*[243]

Biological samples

Prostate tissue samples (51 prostate cancer and 53 normal prostate tissues) were obtained from the University Medical Centre Hamburg-Eppendorf (Hamburg, Germany) in agreement with the local ethics committee and the patients. Only tissues containing at least 70 % tumor cells were included in the study. Normal prostate tissue samples contained exclusively normal tissue material with epithelial cell content between 20 % and 40 %. Epithelial cells were collected by Laser Capture Microdissection (Zeiss) from 10 tissue sections each. DNA was isolated using the DNA Mini Kit (Qiagen) according to the manufacturer's instructions. The *TMPRSS2:ERG* fusion status was determined with real-time PCR.

Gene expression analysis on Affymetrix GeneChip microarray

To obtain amplified and labelled sense DNA, the Affymetrix GeneChip Whole Transcript Sense Target Labelling Assay was applied on 1 µg of total RNA. According to the manufacturer's instructions, cDNA was hybridized to the Affymetrix 1.0 Human Exon ST arrays. The raw data were processed with the Affymetrix powertools.

Methylated DNA immunoprecipitation and high-throughput sequencing (MeDIP-Seq)

Briefly, 2.5 µg of genomic DNA were fragmented to 100 – 200 bp using the Covaris S2 system and end repaired with End Repair mix (Enzymatics) followed by a purification step (Qiagen DNA Purification Kit). Barcoded sequencing adapters were ligated followed by nick translation with DNA polymerase I (NEB, 10 U). Anti-5-methyl cytosine-coupled magnetic beads were used for the enrichment step of the methylated DNA immunoprecipitation (MeDIP). Sequencing libraries were generated before the enrichment and incubated with the beads for 4 h in IP buffer (10 mmol/l sodium phosphate buffer pH 7, 140 mmol/l NaCl, 0.25 % Triton-X 100). Beads were washed 3x in IP buffer and DNA was eluted in elution buffer (50 mmol/l Tris-HCl

pH 7.5, 10 mmol/l EDTA, 1 % SDS) for 15 min at 65 °C. After 2 h of incubation with proteinase K, the DNA was extracted (phenol/chloroform) and precipitated (ammonium acetate/ethanol). SOLiD sequencing libraries were prepared following the SOLiD V3 fragment multiplex library preparation protocol (Life Technologies). Following MeDIP, enrichment libraries were amplified with multiplex library PCR primers, size-selected and quantified by qPCR with library PCR primers. Dilutions of a prequantified SOLiD fragment library control (DH10B) were used to create the standard. Samples were diluted to 100 pg/µl using 1x Low TE buffer (Applied Biosystems) and qPCR was repeated. Equal amounts of up to 8 barcoded libraries were pooled and fixed to sequencing beads by emulsion PCR following the templated bead preparation protocol for SOLiD V3. Sequencing was conducted on a SOLiD 3 Plus using barcode sequencing chemistry (up to 35 bp; Lifetechnologies).

2.2.10 Luciferase reporter assay

To examine gene promoter activities under certain conditions, the Dual-Luciferase Reporter Assay System (Promega) was applied. The LGALS3BP and STAT1 promoter regions were cloned by Andrea Wunderlich in front of the *Photinus pyralis* (firefly) luciferase reporter gene, respectively, whose expression was later driven by the promoter fragment. After substrate administration, the luciferase expression resulted in light emission, which corresponds to the promoter activity. The pGL3-Enhancer (E) reporter vector system (Promega) was used for the promoter cloning and the *Renilla reniformis* (sea pansy) luciferase vector phRL-TK was applied for normalization. Both vector systems were kindly provided by the group of PD Dr. Sylvia Krobitsch.

8×10^4 Hek293T cells were seeded in 24-well plates and co-transfected the next day with the *Renilla reniformis* (sea pansy) luciferase reporter vector and either the cloned promoter construct or the empty vector as a control. Additionally, cells were transfected for 72 h with shRNA targeting the long isoform of BRD4 (shE1), both isoforms of BRD4 (shC2) or shGFP as a control. To analyse the effect of INFγ stimulation on LGALS3BP promoter activity, cells were furthermore treated with 100 U INFγ for 48 h and with 0.1 % BSA as a control.

Afterwards, the luciferase reporter assay was performed according to the manufacturer's instructions. Briefly, the cells were washed with 1x PBS before being lysed directly in the 24-well plates in 100 µl of 1x Passive Lysis Buffer per well for 15 min at room temperature. Subsequently, 20 µl of the lysate were transferred into a white clear bottom 96-well plate (Costar), which was then inserted into the Glomax Multi luminometer (Promega) to measure luciferase activities using a pre-designed programme: Firefly and sea pansy luciferase activities were acquired successively for each 10 s with a 2 s delay after initial application of 25 µl LAR II substrate and subsequent injection of 25 µl Stop & Glo substrate to the lysates. The firefly luciferase activities were then normalized to the corresponding sea pansy luciferase activities and further normalization was carried out to the empty vector, shGFP and BSA-treatment controls. Results were tested for significance using a two-tailed *t*-test.

2.2.11 Microtubule regrowth assay

One day before treatment 1.5 x 10^5 MCF10A cells, 1.5 x 10^5 stable FlpIn TRex 293 cells or 3 x 10^5 SK-BR-3 cells were seeded on PLL coated coverslips in 24 well plates. To depolymerize microtubules, cells were treated with 33 µM nocodazole diluted in corresponding culture medium for two hours at 37 °C. Thereafter, cells were washed four times with warm culture medium and incubated at 37 °C to allow microtubule regrowth. Cells were fixed with ice-cold MeOH immediately after 5 min and 10 min nocodazole washout, respectively and were immunolabelled for both α-tubulin and γ-tubulin afterwards. Immunofluorescence images were obtained using a Zeiss Axioimager Z1 microscope with a Zeiss Plan-Apochromat 63x/1.4 oil objective. Images were recorded with a Zeiss AxioCamMRm camera using AxioVision 4.8 acquisition software. Microtubule regrowth was defined as the area covered by MTOC asters in relation to the whole cell area. For regrowth quantification microtubule asters that emanated from centrosomes as well as the corresponding cells were outlined by hand using the ImageJ software's freehand selection tool and selected areas were measured in pixels subsequently. The experiments were carried out in duplicates with n>200 of analysed cells per replicate for each time point. Data were expressed as ratio between

aster and cell area and displayed by boxplots using the R package ggplot2. A Wilcoxon rank sum test with continuity correction was applied to obtain *p* values.

2.2.12 Mitotic arrest

A mitotic arrest was induced as performed by Qian *et al.*[281] by culturing U2OS cells successively for 24 h with 2 mM thymidine, 2 h without thymidine and 16 h with 100 ng/ml nocodazole. Cells accumulated in mitosis were collected by shake-off and lysed in an appropriate lysis buffer for subsequent analysis.

2.2.13 Phosphorylation analysis in immunoblots

Detection of LGALS3BP phospho-bands in mitotic and interphase U2OS cells

U2OS cells were arrested in mitosis as described above and collected by shake-off. The left-over interphase cells were separately collected after trypsinization. Cells were pelleted by centrifugation at 4 °C and 1,200 rpm (Eppendorf Centrifuge 5810R). Subsequently, cell pellets were washed twice with cold PBS and lysed for 30 min in 500 µl of lysis buffer A (containing phosphatase and protease inhibitors) on ice. Lysates were supplemented with 2x SDS sample buffer and separated by SDS-PAGE. Proceeding with western blotting, the dry milk solution was supplemented with phosphatase and protease inhibitors. Phosphorylated and non-phosphorylated LGALS3BP was detected by antibody-labelling of endogenous LGALS3BP.

Dephosphorylation of LGALS3BP

U2OS cell pellets were washed twice with cold PBS and lysed for 30 min on ice in 500 µl of lysis buffer B (supplemented with protease inhibitors, but lacking phosphatase inhibitors). Subsequently, 100 U of calf-intestinal alkaline phosphatase (CIP) were added to the lysate and incubation was carried out for 60 min at 37 °C in a thermomixer (Eppendorf). Thereafter, protein samples separated by SDS-PAGE were analysed by western blotting using dry milk solutions supplemented only with protease inhibitors. Cells lysed in lysis buffer A without following CIP-treatment served as negative controls. Immunolabelling against endogenous LGALS3BP was used to evaluate the success of dephosphorylation.

2.2.14 Kinase profiling against peptide substrates

To find appropriate kinases responsible for LGALS3BP phosphorylation, three selected phosphorylation sites were examined, which were mentioned on www.phosphosite.org (S256, S444) and www.phosida.com (T220). These phosphorylation sites were then entered into two different kinase motif finder platforms (PhosphoNET by Kinexus and KinasePhos2.0, respectively) to find best matching kinases by algorithm. The kinases AKT1, CaMK4, CHK1, CHK2, CK1d and PLK1 were chosen because they showed high prediction scores.

Subsequently, Kinexus was assigned to synthesize wild type peptides of LGALS3BP incorporating the annotated phosphorylation sites and mutant peptides, in which the phosphorylatable serine or threonine was exchanged by a non-phosphorylatable alanine (Table 12).

Table 12: Synthetic LGALS3BP peptides used for Kinexus profiling against selected protein kinases
Six different peptides were synthesized for the predicted phosphorylation sites at T220, S256 and S444 of native LGALS3BP protein. For the non-phosphorylatable mutant peptides T/S was replaced by A at the site of interest. To allow binding to the phosphocellulose plate within the radiometric assay, YS was removed from original T220 sequence, DL and SD was replaced by KK in the S256 and S444 peptides, respectively. Sequence changes are highlighted in blue and phosphorylation sites of interest in red. Wt – wild type, mt – mutant.

Predicted Phosphorylation Site	Synthetic Peptide	Status	Synthetic Peptide Sequence	Purity [%]
T220 YSRRIDITLSSVKCF	T220	wt	- - RRIDITLSSVKCF	>90
	A220	mt	- - RRIDIALSSVKCF	>85
S256 ILLPQDPSFQMPLDL	S256	wt	ILLPQDPSFQMPLKK	>86
	A256	mt	ILLPQDPAFQMPLKK	>90
S444 PLVKYSSDYFQAPSD	S444	wt	PLVKYSSDYFQAPKK	>98
	A444	mt	PLVKYSADYFQAPKK	>95

The various recombinant protein kinases employed in the substrate profiling process were cloned, expressed and purified by Kinexus using proprietary methods. Kinexus then profiled the kinases against the custom peptides in duplicates using the radiometric assay method as followed:

- Profile T220 and A220 peptides against kinases AKT1, CK1d and PLK1
- Profile S256 and A256 peptides against kinases AKT1, CaMK4, CHK1 and CHK2
- Profile S444 and A444 peptides against kinases AKT1, CaMK4, CHK1, CHK2 and PLK1

The radiometric kinase assay was performed in a final volume of 25 µl according to the following assay reaction recipe:

- 5 µl of diluted active protein kinase (≈10-50 nM final protein concentration in the assay)
- 5 µl of assay solution of test substrate (at 500 µM)
- 10 µl of kinase assay buffer
- 5 µl of [γ-^{33}P] ATP (250 µM stock solution, 0.8 µCi)

The assay was initiated by adding [γ-^{33}P] ATP (PerkinElmer) to the reaction mixture. Incubation at room temperature lasted 20 - 40 min depending on the protein kinase tested. After the incubation period, the assay was terminated by spotting 10 µl of the reaction mixture onto a multiscreen phosphocellulose P81 plate. The plate was then washed three times for 15 min in 1 % phosphoric acid solution. The radioactivity on the P81 plate was counted in the presence of scintillation fluid in a Trilux scintillation counter.

Measurements were then averaged and blank corrected. Next, the wild type peptides were compared to the non-phosphorylatable mutant peptides. Differences in counts ≥ 80 % were declared as highly phosphorylated, ≥ 30 % moderately phosphorylated and ≤ 30 % as weakly phosphorylated compared to the corresponding phospho-mutant peptide.

3. Results

This section comprises results that have partly been published by our group[128] as well as outcomes of a collaboration with Dr. Andrea Wunderlich and Dr. Stefan Börno, who are former members of Prof. Dr. Dr. med. Michal-Ruth Schweiger's group. The contributions of others are indicated in the text as well as in our group's publication[128].

3.1 Identification of centrosomal LGALS3BP

3.1.1 LGALS3BP was identified within a centrosomal protein interaction network

The initial project focused on the identification of functional protein networks within the centrosome to examine interdependencies between the centrosome and regulatory and signalling proteins relating to centrosome aberrations frequently observed in cancer. For that reason, 23 centrosomal and cell cycle-regulatory proteins were expressed in human embryonic kidney cells (HEK293) as baits. Next, tandem affinity purification followed by mass spectrometry (TAP-MS) was performed to isolate protein complexes and to identify protein-protein interactions (for more detailed information please see Fogeron *et al.*[128]). The resulting large protein network with 1,560 interactions was then condensed to a smaller protein interaction network among known and newly identified centrosomal proteins (Figure 11a). Two major sub-complexes, centring on γ-TuRC components and the centriolar protein C-Nap1 (CEP250), were identified within the centrosomal network. To determine candidates relating to centrosome abnormalities in cancer, only proteins with at least three interactions and those, which are known to be deregulated in cancer, were selected out of the first 1,560 proteins. Twelve proteins were identified thereby, of which eight proteins showed a centrosomal or spindle-related phenotype after initial functional characterization upon RNAi. Among them, LGALS3BP interacted with the two major sub-complexes via TUBGCP3 and C-Nap1, which was validated by immunoprecipitation approaches (Figure 11b, c). Additionally, the newly identified MAGED2 interacted with p53, the γ-TuRC, C-Nap1 and LGALS3BP (validated in Figure 11d) at a high confidence level and might thus represent another centrosomal candidate protein.

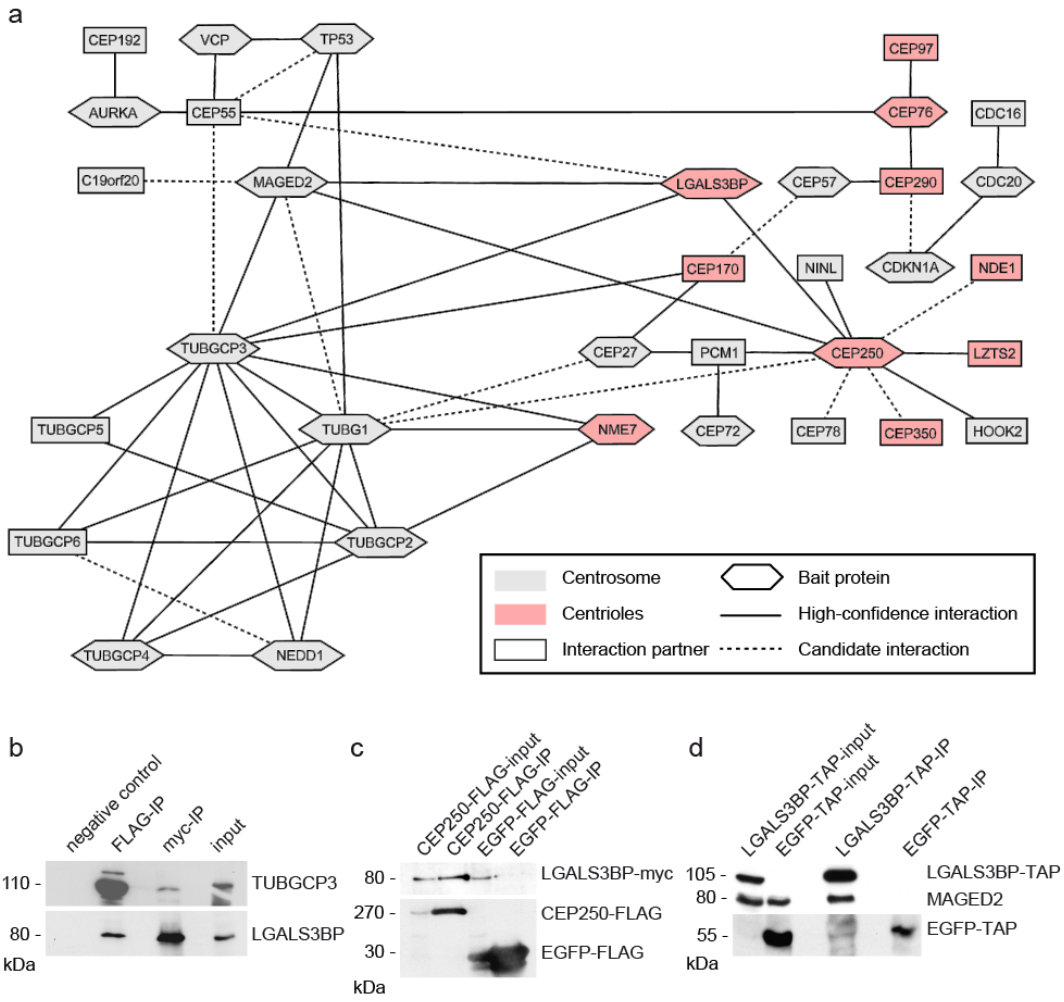

Figure 11: LGALS3BP is identified within a centrosomal protein interaction network
(a) Centrosomal protein interaction subnetwork derived from a complete TAP interaction network that shows known, newly identified or newly localized centrosome proteins (LGALS3BP and MAGED2). Interactions are displayed as lines between bait proteins (hexagons) and their interaction partners (rectangles). Centrosomal proteins are coloured in grey and centriolar proteins in red. Solid lines indicate high confidence interactions (Mascot score of the prey protein >50, at least two identified peptides) and dotted lines candidate interactions (Mascot score >24). **(b)** The interaction of LGALS3BP with TUBGCP3 was validated by co-immunoprecipitation after co-expression of TUBGCP3-FLAG and LGALS3BP-myc in HEK293 cells. **(c)** The interaction between LGALS3BP-myc and a FLAG-tagged CEP250 fragment was confirmed by FLAG-immunoprecipitation after co-expression in HEK293 cells. Co-expression of EGFP-FLAG and LGALS3BP-myc served as a negative control. **(d)** Endogenous MAGED2 interacted with TAP-tagged LGALS3BP in HEK293 cells. EGFP-TAP was used as a negative control. Figure adapted from Fogeron *et al.*[128]

3.1.2 LGALS3BP localized to centrioles

After validation of LGALS3BP within the centrosomal protein interaction network, it was of interest whether LGALS3BP veritably localizes to centrosomes. For this purpose, immunofluorescence microscopy of human osteosarcoma cells (U2OS) was performed using a mouse monoclonal antibody against LGALS3BP after pre-fixation extraction.

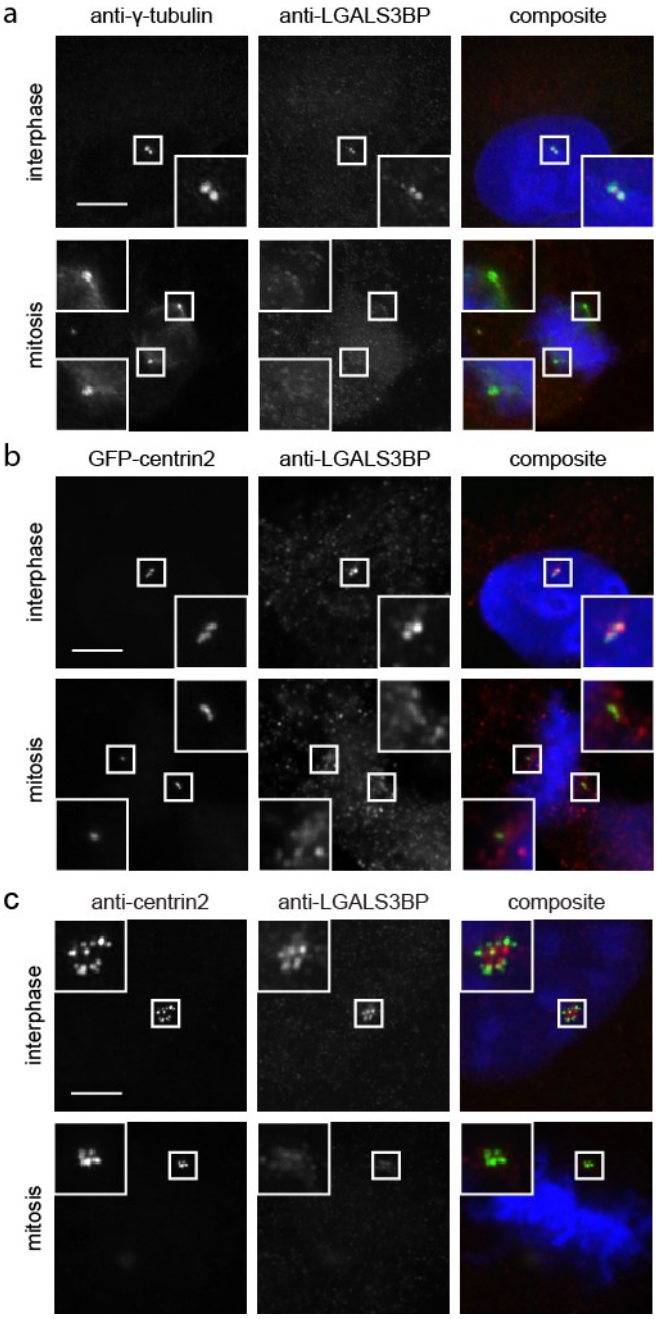

Figure 12: Endogenous LGALS3BP localizes to the centrosome and is amplified upon centriole overduplication **(a)** LGALS3BP localized to the centrosome in U2OS cells in interphase and to a much lesser extent in mitosis. Centrosomes were labelled with an anti-γ-tubulin antibody shown in green, LGALS3BP was labelled with a mouse monoclonal antibody shown in red and DNA was stained with DAPI shown in blue in the composite images. **(b)** LGALS3BP localized to the proximal part of centrioles in interphase U2OS cells stably expressing GFP-centrin2. LGALS3BP-labelling appeared weaker in mitosis. GFP-centrin2 is shown in green, LGALS3BP-labelling in red and DAPI-stained DNA in blue in the composite images. **(c)** LGALS3BP foci were amplified after induction of centriole overduplication by exogenous overexpression of TAP-tagged PLK4 for 48 h in U2OS cells. Amplified LGALS3BP foci localized proximal to newly formed centrioles and their signal intensity appeared weaker in mitosis. Centrioles were labelled with a mouse monoclonal anti-centrin2 antibody shown in green, LGALS3BP was labelled with a mouse monoclonal antibody shown in red and DNA was stained with DAPI shown in blue in the composite images. Scale bars in all images represent 5 µm.

Endogenous LGALS3BP localized to interphase centrosomes as counter-labelled with an anti-γ-tubulin antibody, whereas LGALS3BP-labelling appeared weaker in mitosis (Figure 12a). More precisely, LGALS3BP localized to the proximal part of centrioles in interphase U2OS cells stably expressing GFP-centrin2, as judged by the positioning of procentrioles (Figure 12b). Next, LGALS3BP localization was examined in U2OS cells after induction of centriole overduplication by overexpression of TAP-tagged PLK4 for 48 h. Interestingly, this led up to amplified LGALS3BP foci, which localized to the proximal ends of the overduplicated centrioles. LGALS3BP-labelling appeared weaker in mitosis also under these conditions (Figure 12c).

In the following, localization of exogenously expressed LGALS3BP was investigated through immunofluorescence microscopy. For this purpose, U2OS cells were transfected with a LGALS3BP-FLAG expression plasmid for 48 h. Expression of EGFP-FLAG served as a negative control. Labelling the centrosome with an anti-γ-tubulin antibody revealed a centrosomal localization of the LGALS3BP-FLAG expression construct while the negative control did not (Figure 13a). In more detail, LGALS3BP-FLAG was detected at the centrioles and their interconnecting area as revealed by counter-labelling centrioles with a centrin2-antibody (Figure 13b).

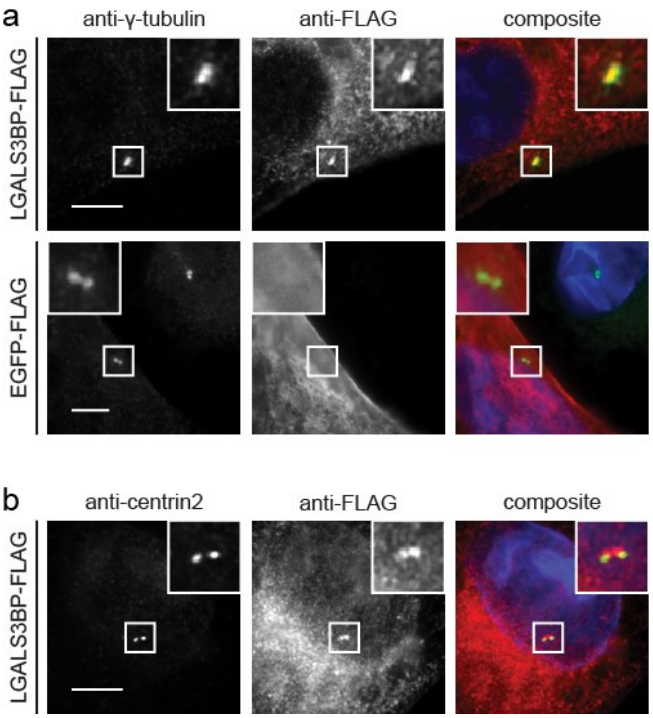

Figure 13: Exogenous LGALS3BP localizes to the centrosome
FLAG-tagged LGALS3BP and EGFP were transiently expressed for 48 h in U2OS cells. **(a)** LGALS3BP-FLAG localized to the centrosome as given by γ-tubulin whereas the negative control EGFP-FLAG did not. LGALS3BP-FLAG and EGFP-FLAG were labelled with an anti-FLAG antibody shown in red, anti-γ-tubulin-labelling is shown in green and DAPI-stained DNA is shown in blue in the composite images. **(b)** LGALS3BP-FLAG localized to the proximal end of centrioles and to their interconnecting area. Centrioles were labelled with an anti-centrin2 antibody shown in green, LGALS3BP-FLAG-labelling is shown in red and DAPI-stained DNA is shown in blue in the composite image. Scale bars in all images represent 5 µm. Figure modified from Fogeron *et al.*[128]

Additional studies were performed by our group, including transmission electron microscopy of pre- and post-embedding immunogold-labelling of LGALS3BP in U2OS cells, which also confirmed proximal localization of LGALS3BP to centrioles[128].

Altogether, LGALS3BP was found to be a centrosomal protein associated with the proximal part of centrioles. In a centrosomal context, LGALS3BP has only been reported to interact with the γ-TuRC[282] at that time, but neither centrosomal localization nor function has been analysed before. We therefore decided to focus on LGALS3BP for further detailed studies.

3.2 Functional characterization of centrosomal LGALS3BP

3.2.1 Overexpression of LGALS3BP caused PCM hypertrophy

After LGALS3BP has been identified as a centrosomal protein as described in the previous section, a next question was the functional role of LGALS3BP for the centrosome. This was first addressed by overexpression experiments. For this purpose, HEK293T cells were transiently transfected with a CMV promoter-driven LGALS3BP-FLAG plasmid for 48 h. HEK293T cells were chosen because they are easily transfectable and show high transfection rates. The pFLAG-CMV-D11 vector backbone additionally ensured high expression rates.

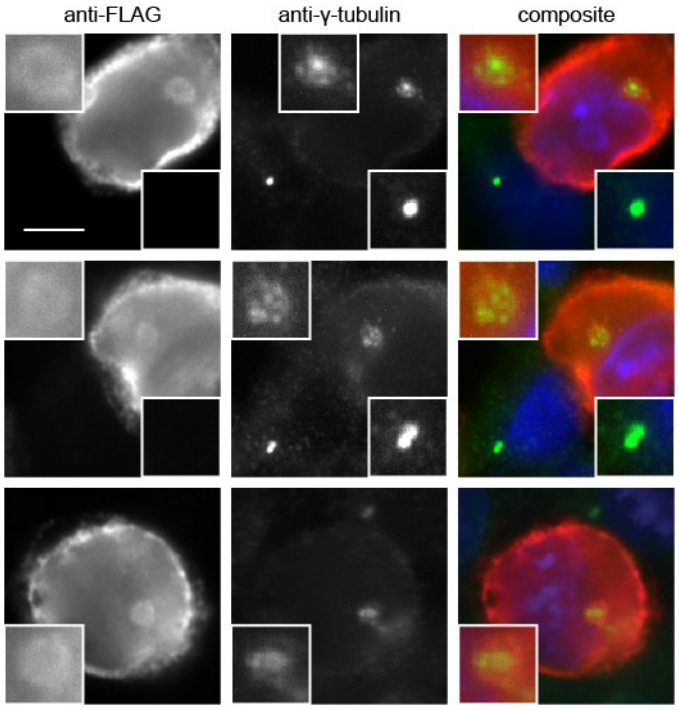

Figure 14: LGALS3BP overexpression leads to the accumulation of pericentriolar material
HEK293T cells were transiently transfected with a LGALS3BP-FLAG expression plasmid for 48 h. Cells that overexpress LGALS3BP-FLAG displayed dispersed centrosome structures with accumulated pericentriolar material (PCM) as labelled with an anti-γ-tubulin antibody. Untransfected cells (bottom left in the first two rows), on the other hand, exhibited focused centrosomes. γ-tubulin is shown in green, anti-FLAG-labelling in red and DAPI-stained DNA in blue in the composite images. Boxes display magnifications of the centrosome and the scale bar represents 5 µm.

HEK293T cells transfected with LGALS3BP-FLAG for 48 h showed localization of the overexpressed fusion protein to the cytoplasm and prominently to the cell cortex. Additionally, a strong labelling in the area of the centrosome was detected as given by γ-tubulin immunolabelling (Figure 14). Interestingly, centrosomes of those transfected cells appeared enlarged with dispersed PCM and not as focussed as in untransfected neighbouring cells. However, the enlarged PCM area never exceeded the LGALS3BP-FLAG accumulations in the centrosomal region. These findings might be due to potential γ-TuRC acquisition capabilities of LGALS3BP because it was shown to

interact with the γ-TuRC via GCP3 in the centrosomal protein-interaction network (Figure 11).

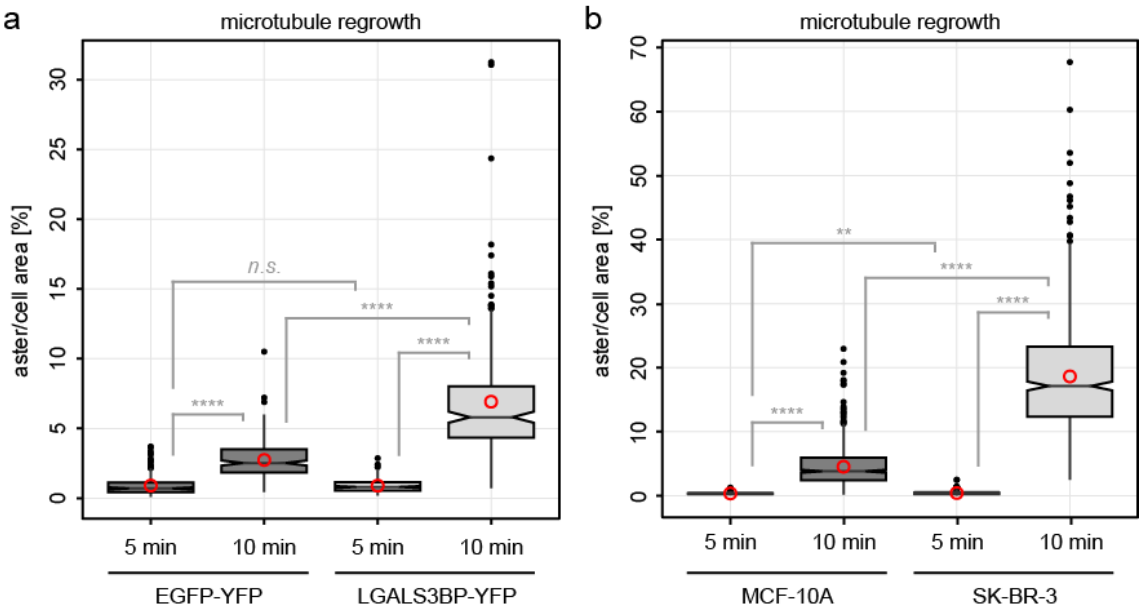

Figure 15: Microtubule regrowth assay in LGALS3BP-overexpressing cells
Microtubules were depolymerized by nocodazole-treatment and then allowed to regrow after washout with the respective culturing medium for 5 or 10 min. Repolymerization was measured as ratio between microtubule aster and whole cell area. Data are expressed as boxplots of duplicates (a) or triplicates (b) with each $n>200$. Red circles indicate the means. *P*-values were obtained via Wilcoxon rank sum test with continuity correction**:** **** $p<0.0001$, ** $p<0.01$ and *n.s.* not significant. **(a)** Expression of stably integrated LGALS3BP-YFP was induced for 48 h by tetracycline in FlpIn TRex 293 cells before nocodazole-treatment. EGFP-YFP served as a control. The area covered by regrowing microtubules increased by time in both expression backgrounds with the LGALS3BP-YFP expressing cells covering a larger area after 10 min compared to control cells. **(b)** The breast cancer cell line SK-BR-3 showed larger areas of microtubule asters after 10 min of regrowth compared to the non-tumorigenic breast epithelial cell line MCF-10A.

PCM hypertrophies besides other centrosomal aberrations are hallmarks of cancer and are known to affect microtubule nucleation ability of centrosomes[104,283]. To test whether PCM hypertrophy due to LGALS3BP overexpression influences microtubule nucleation, a regrowth assay upon nocodazole-treatment was performed in stably transfected FlpIn TRex 293 cells. Additionally, the breast cancer cell line SK-BR-3 was analysed, because it endogenously overexpresses LGALS3BP and shows PCM hypertrophy (Figure 24 on page 71). As a control the non-tumorigenic breast epithelial cell line MCF-10A with normal centrosomes and normal levels of LGALS3BP expression was included to the assay. As time points for measurements, 5 min and 10 min were chosen for analysis because in all investigated cells the microtubule asters were clearly

visible after 5 min in and the whole cell area was not yet covered by microtubules after 10 min of nocodazole release.

The area of microtubule asters steadily increased in all examined cells after nocodazole washout. Tetracycline-induced overexpression of LGALS3BP-YFP in FlpIn TRex 293 cells led to a significantly faster increase of aster area covering the cell compared to EGFP-YFP expressing cells after 10 min (Figure 15). The same behaviour was observed in the two breast cell lines with the cancerous SK-BR-3 cells having shown faster microtubule regrowth compared to the non-tumorigenic MCF-10A cells after 10 min (example images shown in Supplemental Figure 1).

High LGALS3BP protein levels leading to PCM hypertrophy might thus correlate with overall centrosomal microtubule organization capacity.

3.2.2 Depletion of LGALS3BP affected centriolar integrity

As a next step, depletion of endogenous LGALS3BP was performed by RNAi to examine a potential effect on centrosome structure or number. For this purpose, human osteosarcoma U2OS cells were transfected for 72 h with a siRNA pool targeting LGALS3BP and a non-targeting siRNA pool as a control.

As observed in immunofluorescence microscopy, an efficient depletion of LGALS3BP in U2OS cells (Figure 16c) led to supernumerary centrin2-positive structures, which were partly not associated with the PCM (Figure 16a). These multiple centriolar structures appeared in interphase (≈ 50 %) and in mitosis even more frequently (≈ 80 %), which was validated by quantification of centrin2 foci in immunofluorescence microscopy carried out by Marie-Laure Fogeron[128] (Figure 16b).

This experiment was repeated with alternative LGALS3BP siRNAs to exclude any off-target effects of the siRNA pool that was used initially.

Indeed, transfection of U2OS cells with a siRNA pool targeting the 3'UTR of *LGALS3BP* mRNA as well as with another single LGALS3BP siRNA resulted in supernumerary centriole-like structures detected in immunofluorescence microscopy (Figure 17a). These structures significantly occurred in ≈ 30 % and respectively ≈ 45 % of the cells, which was validated after quantification of excess centrin2-positive foci per cell applying a two-tailed *t*-test (Figure 17b). Furthermore, LGALS3BP protein levels were

effectively depleted by alternative silencing just as the initial transfection with the LGALS3BP siRNA pool as determined by immunoblotting (Figure 17c).

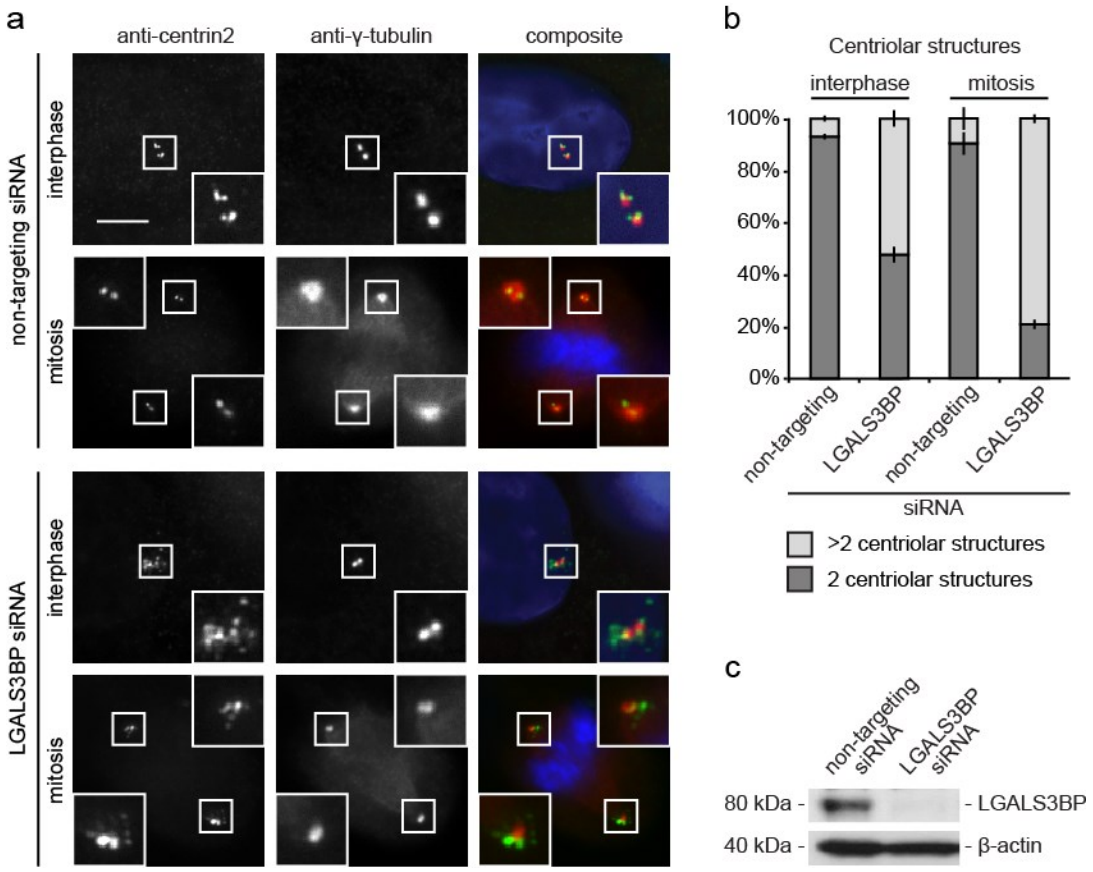

Figure 16: LGALS3BP depletion leads to supernumerary centriolar structures
U2OS cells were treated 72 h with a siRNA pool targeting *LGALS3BP*. Non-targeting siRNA served as a negative control. **(a)** Depletion of LGALS3BP led up to multiple centriolar structures in interphase and mitosis, respectively. These centrin2-positive structures were partly not associated with the PCM as labelled with an anti-γ-tubulin antibody. Antibody-labelling of centrin2 is shown in green, γ-tubulin in red and DAPI-stained DNA in blue in the composite images. The scale bar represents 5 µm. **(b)** Quantification of centriolar structures per centrosome. The plots represent means ± standard deviation of duplicates with each *n*>200. **(c)** Immunoblotting of LGALS3BP validated the depletion efficiency in this experiment. β-actin served as a loading control.

Subsequently, a rescue experiment was performed in U2OS cells to substantiate the centriolar LGALS3BP depletion phenotype. For that purpose, endogenous LGALS3BP was depleted by RNAi targeting the 3'UTR of *LGALS3BP* mRNA together with transient overexpression of exogenous LGALS3BP-YFP. Thereby, the occurrence of excess centriolar structures upon depletion of endogenous LGALS3BP was rescued in LGALS3BP-YFP-overexpressing cells up to 96 h. Neighbouring cells that were not expressing LGALS3BP-YFP or cells expressing EGFP-YFP as a control did not show a rescue of supernumerary centriolar structures (Figure 18a). The quantification of

excess centrin2 foci revealed a significant increase for cells depleted for endogenous LGALS3BP together with EGFP-YFP overexpression as a positive control compared to cells transfected with non-targeting siRNA as a negative control. The occurrence of these supernumerary centriolar structures successively decreased by time in cells simultaneously expressing exogenous LGALS3BP-YFP until there was no significant difference anymore after 96 h compared to the negative control (Figure 18b).

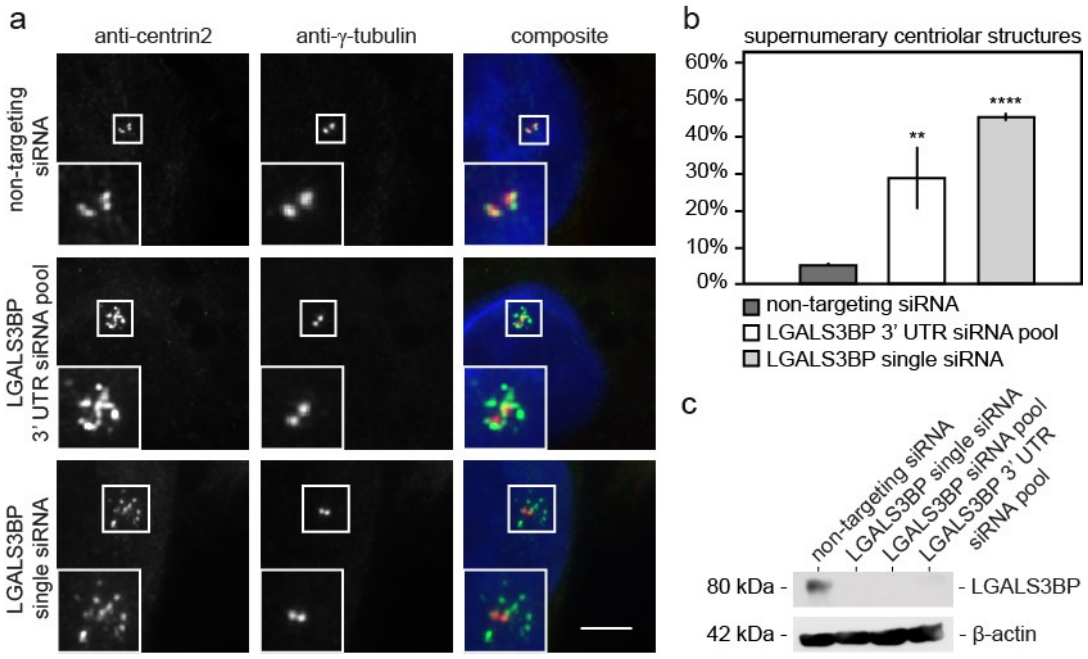

Figure 17: LGALS3BP depletion phenotype is reproduced by alternative siRNA-transfection
U2OS cells were transfected 72 h with a siRNA pool targeting the 3'UTR of *LGALS3BP* mRNA and with an alternative single siRNA against *LGALS3BP*. Non-targeting siRNA was used as a negative control. **(a)** In immunofluorescence microscopy both siRNA-treatments targeting different regions of LGALS3BP led to multiple centrin2-positives structures exceeding PCM area given by γ-tubulin-labelling. Antibody-labelling of centrin2 is shown in green, γ-tubulin in red and DAPI-stained DNA in blue in the composite images. The scale bar represents 5 µm. **(b)** Quantification of supernumerary centriolar structures that were more than 4 per cell. Data are expressed as means ± standard deviation of triplicates with each $n>200$. **** $p<0.0001$ and ** $p<0.01$ compared to non-targeting siRNA control in a two-tailed *t*-test. **(c)** Immunoblotting of LGALS3BP demonstrated the depletion efficiency of three different LGALS3BP knockdowns. β-actin served as a loading control. Figure modified from Fogeron *et al.*[128]

Supportingly, western blot analysis corroborated an efficient knockdown of endogenous LGALS3BP while protein levels of exogenous LGALS3BP-YFP progressively augmented in this experiment (Figure 18c). Overall, these findings indicate that the occurrence of supernumerary centrin2-positive structures was exclusively caused by the depletion of LGALS3BP and did not represent any off-target effects.

Since fluorescence-activated cell sorting and mitotic index analysis did not show distinct changes cell cycle progression after LGALS3BP depletion compared to control[128], the observed supernumerary centrin2-positive structures are not likely to occur due to cell cycle deregulation. Moreover, these excess centriolar structures had partially not acquired PCM, suggesting that they were not capable to mature.

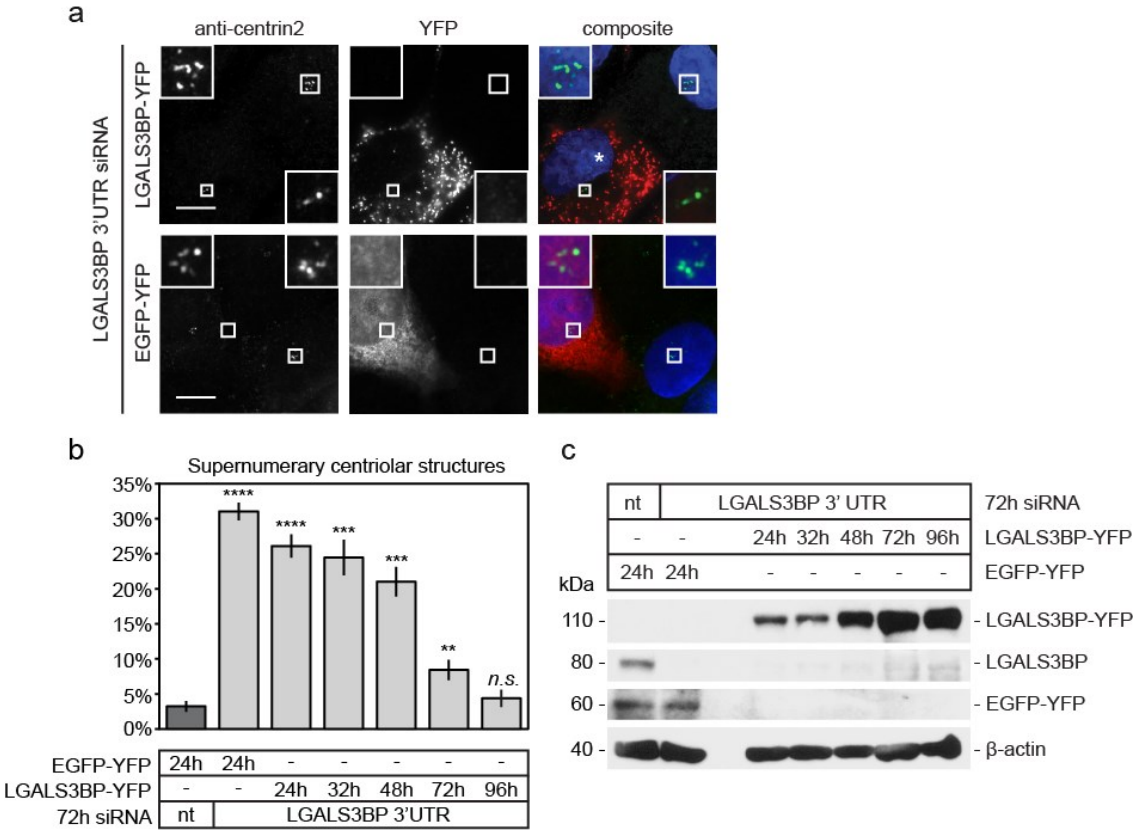

Figure 18: Exogenous LGALS3BP expression rescues the depletion phenotype of endogenous LGALS3BP

Depletion of endogenous LGALS3BP with a LGALS3BP 3'UTR siRNA pool while simultaneously overexpressing exogenous LGALS3BP-YFP decreased the supernumerary centriolar structures in U2OS cells. Overexpression of EGFP-YFP and the non-targeting (nt) siRNA pool served as negative controls. **(a)** The centriolar phenotype after depletion of endogenous LGALS3BP was rescued in LGALS3BP-YFP-overexpressing U2OS cells (asterisk) that showed a normal centriole number (upper panel). This was not the case in cells expressing EGFP-YFP as control (lower panel). Centrin2-labelling is displayed in green, LGALS3BP-YFP and EGFP-YFP are shown in red and DAPI-stained DNA in blue in the composite images. The scale bars represent 10 µm. **(b)** Quantification of the centrin2-positive structures that were more than 4 per cell. Overexpression of exogenous LGALS3BP-YFP by 96 h decreased the supernumerary centriolar structures up to control ranges. Data are shown as means ± standard deviation of triplicates with n>200 for each experiment. **** p<0.0001, *** p<0.001, ** p<0.01 and *n.s.* not significant compared to negative control in a two-tailed t-test. **(c)** Immunoblotting of LGALS3BP and LGALS3BP-YFP validated the depletion of endogenous LGALS3BP while exogenous protein was overexpressed. β-actin served as a loading control. Figure modified from Fogeron *et al.*[128]

To verify this hypothesis, the protein composition of these structures was qualitatively analysed by immunofluorescence microscopy. For this purpose, twelve centriolar and

pericentriolar markers were examined regarding their localization to supernumerary centriole-like structures that appear upon LGALS3BP depletion in U2OS cells.

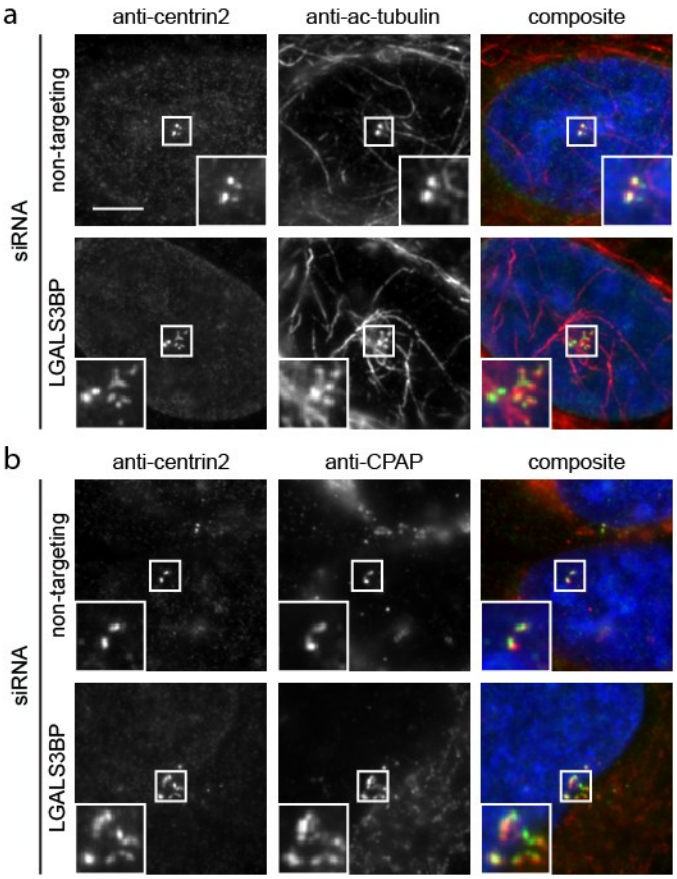

Figure 19: Centrin2-positive structures after LGALS3BP depletion contain acetylated tubulin and CPAP
Qualitative fluorescence microscopy analysis of U2OS cells being transfected for 72 h with a LGALS3BP siRNA pool. Non-targeting siRNA served as a negative control. **(a)** In control cells acetylated tubulin was located at the parental centrioles but not to newly formed procentrioles (G2-centrioles in upper panel). After LGALS3BP knockdown acetylated tubulin localized to supernumerary centrin2-positive structures (lower panel). **(b)** In non-targeting siRNA-transfected cells CPAP localized to the centrioles (upper panel). LGALS3BP-depleted cells showed excess centrin2-positive structures with residing CPAP (lower panel). Centrin2-immunolabelling is shown in green, anti-ac-α-tubulin and anti-CPAP in red and DAPI-stained in blue in the composite images. The scale bars represent 5 µm.

Intriguingly, these structures comprised centrin2, CPAP (early acquired to procentrioles, but also present at the proximal end of parental centrioles[284]) and acetylated tubulin (Figure 19) but lacked the early centriolar markers PLK4 and SAS6, CEP135, daughter centriolar marker centrobin, mother centriolar marker ODF2, C-Nap1 as well as the PCM components pericentrin and γ-tubulin[128]. Sometimes, polyglutamylated tubulin localized to the supernumerary centriolar structures (Table 13 and Supplemental Figure 2). Altogether, the marker composition of the centrin2-positive structures detected upon LGALS3BP depletion did not indicate precisely their origin. They might represent newly formed, but incomplete centrioles or might be the result of centriolar fragmentation.

3.2.3 Qualitative analysis of LGALS3BP and its interaction partners

In the following, the impact of LGALS3BP interaction partners on the formation of supernumerary centriolar structures and their marker composition was examined in U2OS cells after RNAi. For this purpose, cells were transfected for 72 h with siRNA targeting GCP3, C-Nap1, CEP55, MAGED2 and LGALS3BP as single knockdowns as well as LGALS3BP siRNA together with GCP3, C-Nap1, CEP55 or MAGED2 siRNA for simultaneous depletion. Transfection with non-targeting siRNA served as a negative control. Next, cells were immunolabelled for centrin2 together with centrobin, acetylated α-tubulin, CPAP, SAS6, polyglutamylated α- and β-tubulin, CEP135, C-Nap1 or pericentrin and subsequently analysed via immunofluorescence microscopy. The qualitative analysis of the phenotypes is briefly summarized by Table 13 and example images are shown in Supplemental Figure 2.

In control cells, two centrin2 foci were observed in mitosis as well as in G1-phase and four foci in G2-phase. Principally, two foci of each tested marker were observed at interphase centrosomes, with centrobin being located more pronounced at daughter centrioles[285], acetylated and glutamylated tubulin at mature centrioles and SAS6 at procentrioles. CPAP and CEP135 foci were detected at the proximal parts of parental centrioles and at the sides of newly forming procentrioles. C-Nap1 localized to the proximal centriolar region as well as to the interconnecting area and pericentrin around parental centrioles. In mitosis, two centrin2 foci were detected per spindle pole with only one focus of each tested marker localizing to it. The fluorescence intensities of CPAP and C-Nap1 appeared weaker in mitosis as compared to interphase cells.

Noticeably, GCP3 or MAGED2 single knockdown neither affected centriole number after detecting centrin2-labelling nor any other tested marker as compared to the negative control. Furthermore, in all RNAi backgrounds one SAS6 focus was detected per pole in mitosis and two foci at S- and G2-phase centrosomes. In G1 of interphase no SAS6-labelling occurred, because SAS6 is not acquired to procentrioles until the beginning of centriole duplication in early S-phase[24].

The double knockdowns of LGALS3BP with GCP3 or MAGED2 did not reveal alterations in the marker composition of excess centrin2 structures compared to LGALS3BP

depletion alone. Simultaneous depletion of LGALS3BP together with C-Nap1 or CEP55 displayed additive phenotypes of the single knockdowns. However, in contrast to the single knockdowns, centrobin foci were amplified from time to time but did not colocalize to all centrin2-positive structures in the LGALS3BP and C-Nap1 as well as in the LGALS3BP and CEP55 double knockdown.

Table 13: Qualitative analysis of centriolar markers or PCM components upon RNAi
Markers were analysed in immunofluorescence microscopy concerning their localization to centrin2-positive structures upon single and double knockdown of LGALS3BP and its interacting partners for 72 h in interphase U2OS cells. Non-targeting siRNA served as a negative control. Red boxes represent obvious and yellow boxes occasionally observed amplifications compared to non-targeting control. Signal loss or weakening is shown by blue boxes. Numbers in boxes indicate signal foci observed and green-written text elucidates the localization of a tested marker to excess centrin2-positive structures.

		Tested marker								
		Centrin2	Centrobin	Ac-tubulin	CPAP	SAS6	Glut-tubulin	CEP135	C-Nap1	Pericentrin
RNAi	non-targeting	2 - 4	1 - 2	2	2	0 / 2	2	1 - 2	2	1 - 2
	GCP3	2 - 4	1 - 2	2	2	0 / 2	2	1 - 2	2	1 - 2
	C-Nap1	frequently amplified	1 - 2	2	frequently amplified	0 / 2	frequently amplified	1 - 2	0 / weak	1 - 2
	CEP55	frequently amplified	1 - 2	frequently amplified	frequently amplified	0 / 2	frequently amplified	frequently amplified	frequently amplified	frequently amplified
	MAGED2	2 - 4	1 - 2	2	2	0 / 2	2	1 - 2	2	1 - 2
	LGALS3BP	amplified	1 - 2	amplified	amplified	0 / 2	frequently amplified	1 - 2	2	frequently amplified
	LGALS3BP + GCP3	amplified	1 - 2	amplified	amplified	0 / 2	frequently amplified	1 - 2	2	frequently amplified
	LGALS3BP + C-Nap1	amplified	frequently amplified	amplified	amplified	0 / 2	frequently amplified	1 - 2	0 / weak	frequently amplified
	LGALS3BP + CEP55	amplified	frequently amplified	amplified	amplified	0 / 2	frequently amplified	frequently amplified	frequently amplified	frequently amplified
	LGALS3BP + MAGED2	amplified	1 - 2	amplified	amplified	0 / 2	frequently amplified	1 - 2	2	frequently amplified

Since LGALS3BP, MAGED2 and C-Nap1 interacted with each other at a high confidence level (Figure 11), it was of interest to examine the interdependencies of these interactions regarding their localization and the formation of supernumerary centriolar structures.

Firstly, centrioles and MAGED2 localization were examined via immunofluorescence microscopy upon knockdown of all three interactors in U2OS cells, respectively. The transfection with non-targeting siRNA served as a negative control. The efficient protein depletion in this experiment was verified by immunoblotting (Figure 20b).

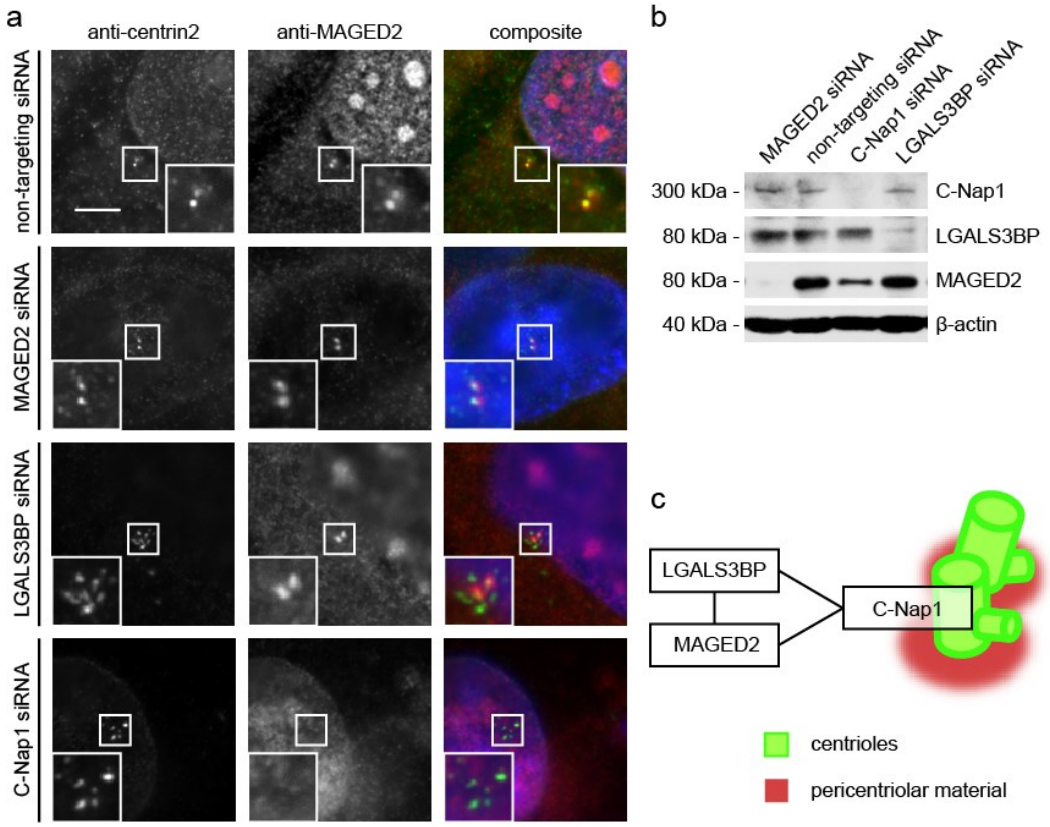

Figure 20: Centrosomal localization of MAGED2 depends on C-Nap1 but not on LGALS3BP
U2OS cells were treated for 72 h with siRNA targeting MAGED2, LGALS3BP or C-Nap1. Non-targeting siRNA served as a negative control. **(a)** MAGED2-depleted cells lost nuclear localization of MAGED2 whilst centrosomal localization of MAGED2 persisted. LGALS3BP knockdown did not affect either nuclear or centrosomal MAGED2 localization but led to supernumerary centriolar structures as given by centrin2-labelling. Depletion of C-Nap1 did not diminish nuclear MAGED2 localization but led to loss of centrosomal MAGED2 and to supernumerary centrin2-positive structures. In the composite images immunolabelling of centrin2 is shown in green, MAGED2 in red and DAPI-labelled DNA in blue. The scale bar represents 5 µm. **(b)** Immunoblotting of this experiment validated the depletion efficiency. **(c)** The schematic illustrates the interactions between LGALS3BP, MAGED2 and C-Nap1 with C-Nap1 mediating their localization to the centrosome.

Immunofluorescence microscopy of centrin2-labelling revealed no effect on centriole number upon MAGED2 knockdown but showed multiple centrin2-positive structures after LGALS3BP and C-Nap1 depletion (Figure 20a, first column). Endogenous MAGED2 showed a speckled localization to the nucleus as well as two foci at the centrioles in control cells. The centrosomal localization of MAGED2 persisted after MAGED2 knockdown, its nuclear localization, however, disappeared. LGALS3BP depletion had no effect on MAGED2 localization to the nucleus and to the centrosome compared to

control cells. The multiple centrin2-positive structures upon LGALS3BP knockdown appeared around the two MAGED2 foci in the centrosomal region. In contrast to MAGED2 and LGALS3BP depletion, a C-Nap1 knockdown led to a loss of centrosomal MAGED2-labelling whilst nuclear labelling was retained (Figure 20a, second column). Altogether, these findings suggested C-Nap1 being necessary for the centrosomal localization of MAGED2 (Figure 20c).

Next, LGALS3BP and C-Nap1 localization was analysed upon RNAi in U2OS cells. Antibody-labelling of endogenous LGALS3BP was again detected at the proximal part of centrioles and their interconnecting region in control cells stably expressing the centriolar marker GFP-centrin2 (Figure 21a, first lane). LGALS3BP depletion led to multiple centrin2-positive structures in these cells accompanied by a reduced LGALS3BP fluorescence intensity of ≈ 60 % at centrosomes as compared to the control (Figure 21a, b). Surprisingly, C-Nap1 knockdown significantly decreased LGALS3BP fluorescence intensity at centrosomes even more (≈ 40 %) than LGALS3BP knockdown (Figure 21a, b). Conversely, LGALS3BP knockdown did not affect C-Nap1 localization to centrosomes (Figure 21c, d). Solely C-Nap1 depletion significantly decreased centrosomal C-Nap1-labelling (Figure 21c, d). Labelling of endogenous LGALS3BP and C-Nap1 in GFP-centrin2-U2OS cells revealed colocalization of both proteins at the proximal part of centrioles as evaluated by the presence of procentrioles (Figure 21e). As a conclusion, C-Nap1 also mediated the localization of LGALS3BP to centrioles probably acting as an anchoring scaffold at the proximal part of centrioles (Figure 21f).

In the following, the interaction of LGALS3BP and C-Nap1 was functionally analysed in more detail. For this purpose, single and double knockdowns of LGALS3BP and C-Nap1 were examined in U2OS cells by immunofluorescence microscopy.

At a first glance, strikingly few mitotic cells were observed after simultaneous depletion of LGALS3BP and C-Nap1 compared to the negative control and the single knockdowns. Additionally, the double knockdown revealed a large amount of apoptotic cells as judged by condensed chromatin bodies. To validate this, mitotic and apoptotic cells were quantified. LGALS3BP and C-Nap1 double knockdown led to a significant decrease of the mitotic index to ≈ 0.5 % as compared to the negative control (≈ 2.5 %), while the LGALS3BP and C-Nap1 single knockdown experiments showed no significant alterations compared to control cells (Figure 22a).

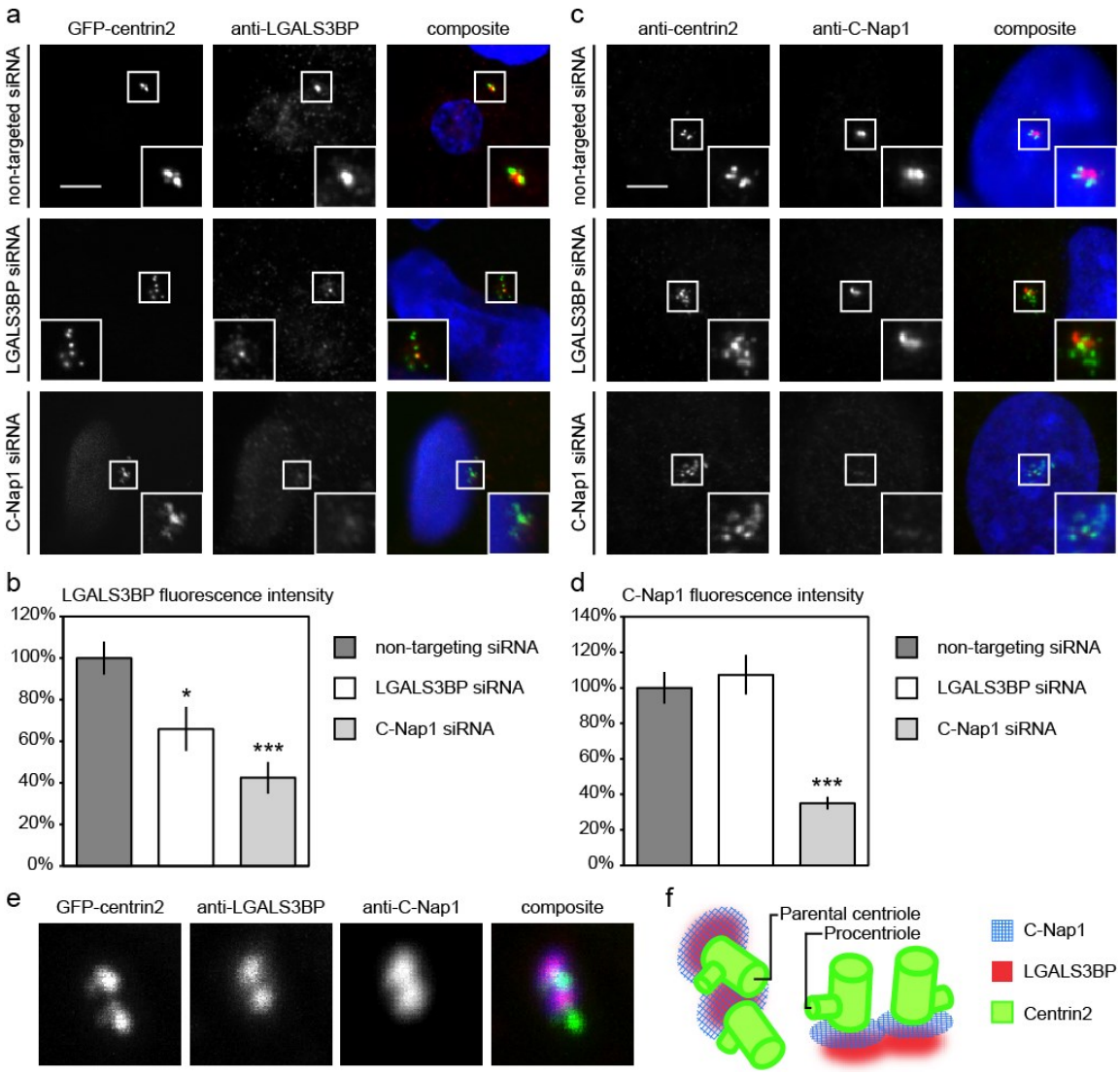

Figure 21: C-Nap1 enables centrosomal localization of LGALS3BP

(a-d) Cells were depleted for LGALS3BP and C-Nap1 by siRNA-transfection for 72 h. Non-targeting siRNA served as a negative control. **(a)** Stably GFP-centrin2-expressing U2OS cells depleted for LGALS3BP displayed amplified centriolar structures with decreased LGALS3BP fluorescence intensity at the region of centrosomes. Cells depleted for C-Nap1 also revealed supernumerary centriolar structures with even lower LGALS3BP fluorescence intensity at centrosomes compared to LGALS3BP depletion. In the composite images GFP-centrin2 is shown in green, LGALS3BP-immunolabelling in red and DAPI-stained DNA in blue. The scale bar represents 5 µm. **(b)** The bar chart represents the ImageJ quantification of background-corrected LGALS3BP fluorescence intensities within the region of the centrosome upon C-Nap1, LGALS3BP and control knockdown. **(c)** U2OS cells depleted for LGALS3BP as well as for C-Nap1 showed supernumerary centrin2-positive structures, respectively. C-Nap1 fluorescence signals remained unchanged at the centrosome after LGALS3BP depletion whilst C-Nap1 knockdown led to a decreased fluorescence intensity of C-Nap1. Immunolabelling of centrin2 is displayed in green, C-Nap1 in red and DAPI-stained DNA in blue. The scale bar represents 5 µm. **(d)** The bar chart plots the ImageJ quantification of C-Nap1 fluorescence intensities at the centrosome upon C-Nap1, LGALS3BP and control knockdown. **(b,d)** Bar charts represent means ± standard deviation of triplicates with $n>200$ for each experiment. * $p<0.05$ and *** $p<0.001$ compared to negative control in a two-tailed t-test. **(e)** C-Nap1 and LGALS3BP colocalized in stably GFP-centrin2-expressing U2OS cells. The localization of both was detected at the proximal part of centrioles as judged by the presence of procentrioles. GFP-centrin2 is displayed in green, immunolabelling of LGALS3BP in red and C-Nap1-labelling in blue in the composite image. **(f)** Schematic localization of C-Nap1 and LGALS3BP to the centrioles.

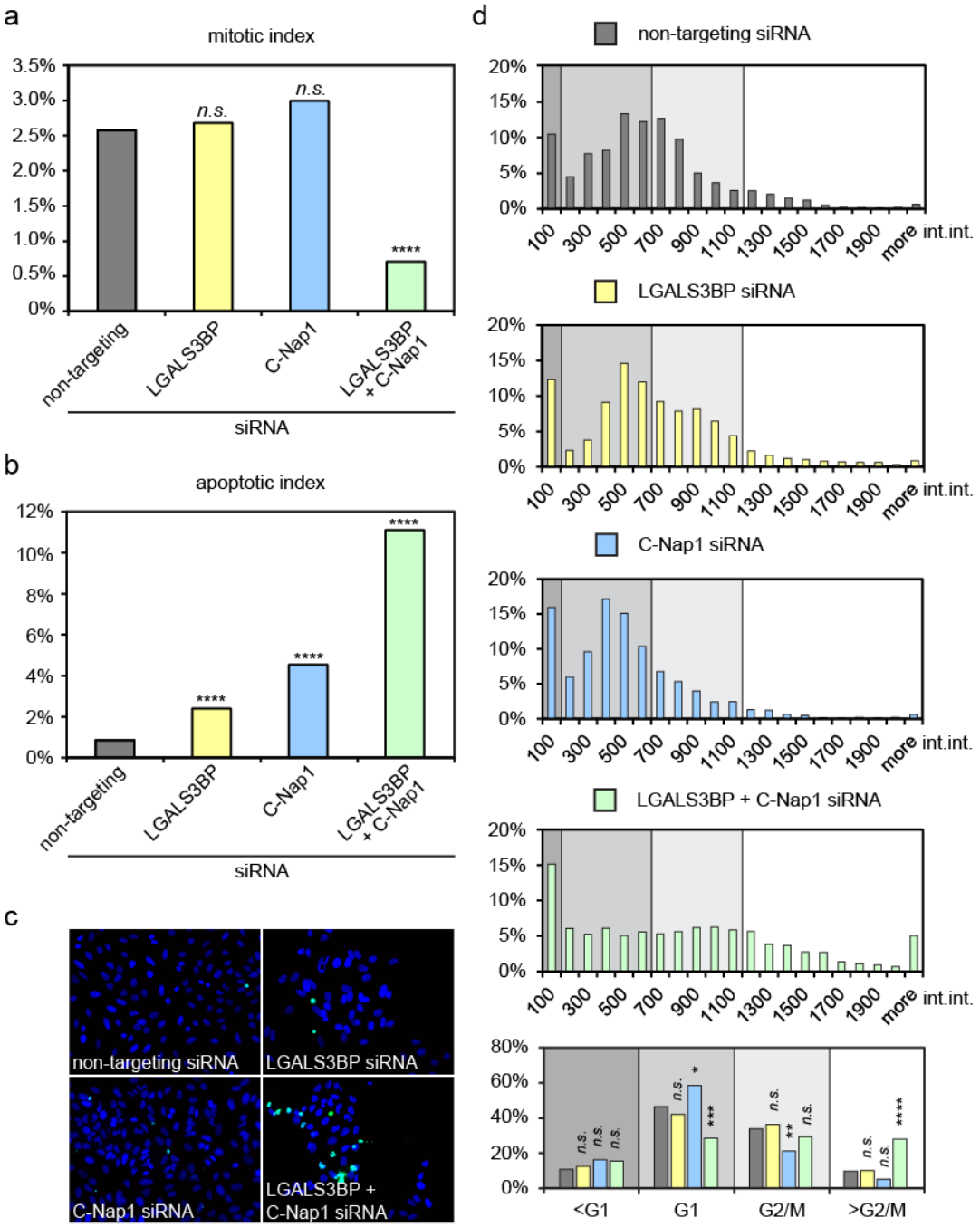

Figure 22: Double knockdown of LGALS3BP and C-Nap1 affects cell cycle distribution and apoptosis rate

U2OS cells were transfected with siRNA targeting LGALS3BP and C-Nap1 for 72 h. Additionally, both targets were depleted simultaneously. Non-targeting siRNA served as a negative control. **(a)** The bar chart displays the quantification of the mitotic index in this experiment. **(b)** The bar chart represents the apoptotic index quantification of TUNEL-positive nuclei. **(a,b)** The following total cell numbers were analysed in this experiment: non-targeting (*n*=5,515), LGALS3BP (*n*=3,133), C-Nap1 (*n*=2,071), LGALS3BP+C-Nap1 (*n*=1,973). **(c)** The immunofluorescence micrographs present example images of TUNEL-labelling (shown in green) in this experiment with DAPI-stained DNA shown in blue. **(d)** The first four histograms display DNA contents obtained by quantitative densitometry of DAPI-stained nuclei given as integrated intensities (int.int.) with *n*>2.000 cells being analysed in each experiment. The different shades of grey within the plot area indicate bins of cell cycle stages (from left: <G1, G1, G2/M, >G2/M). The bottom plot represents cell populations in each bin of cell cycle stage. (a,b,d) Chi-squared tests were applied to test significance with * $p<0.05$, ** $p<0.01$, *** $p<0.001$, **** $p<0.0001$ and *n.s.* not significant compared to non-targeting siRNA control.

Subsequently, a TUNEL assay was performed to label apoptotic cells in this experiment (Figure 22c). Quantification of TUNEL-positive fluorescein signals revealed a highly significant increase of the apoptotic index up to ≈ 11 % in U2OS cells simultaneously depleted for LGALS3BP and C-Nap1 as compared to non-targeting siRNA-transfected cells with an apoptotic index less than 1 %. Single knockdown experiments of LGALS3BP and C-Nap1 also displayed a significant increase of the apoptotic index with ≈ 2 % and ≈ 4 %, respectively (Figure 22b). Nevertheless, these increases did not reach the apoptotic index of the double knockdown, not even as an additive effect.

Considering the decrease of the mitotic index and the increase of the apoptotic index in cells co-depleted for LGALS3BP and C-Nap1, the question arose whether cell cycle distribution might be affected due to a specific arrest. Addressing this question, the DNA content was determined by quantitative densitometry of DAPI-stained DNA in immunofluorescence micrographs using the CellProfiler software. The calculated integrated intensities were then plotted as histograms and split into bins for <G1, G1, G2/M and >G2/M nuclei. As a result, the cell cycle profile of LGALS3BP-depleted cells appeared similar to the non-targeting siRNA control and displayed no significant alterations of cells populating the different bins of cell cycle stages (Figure 22d, last plot). In comparison, the C-Nap1 single knockdown led to a significant shift from G2/M to G1 phase cells, which is in line with previous findings[82,286]. The LGALS3BP and C-Nap1 double knockdown, however, displayed striking alterations compared to the others given by a substantial decrease in the G1 population and a highly significant increase in the >G2/M population of cells. Additionally, a fraction of cells double-depleted for LGALS3BP and C-Nap1 appeared multinucleated or displayed deformed nuclei with nucleus boundary irregularities (Supplemental Figure 6).

3.2.4 LGALS3BP deregulation correlated with centrosome aberrations in cancer cells

As aforementioned, exogenous overexpression of LGALS3BP caused PCM hypertrophy and siRNA-mediated LGALS3BP depletion affected centriolar integrity. Thus, a consequent question was if cells with endogenously deregulated LGALS3BP levels exhibit the described centrosomal aberrations and if these could be even reverted.

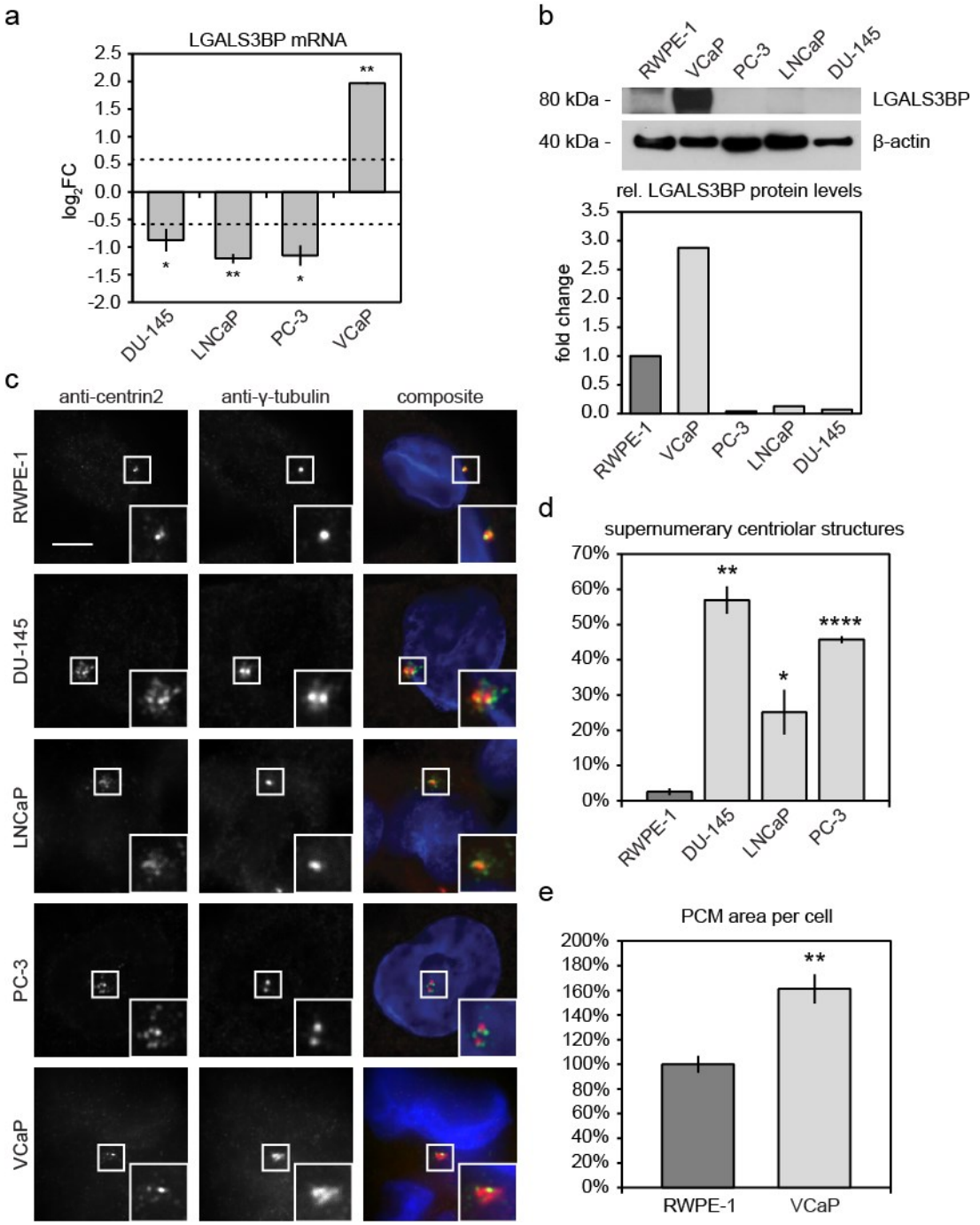

Figure 23: Prostate cancer cells show deregulated LGALS3BP expression and centrosomal aberrations
(a) QPCR analysis of prostate cancer cell lines revealed differential expression of *LGALS3BP* mRNA compared to the non-tumorigenic prostate epithelial cell line RWPE-1. The DU-145, LNCaP and PC-3 cancer cell lines showed low expression of *LGALS3BP* mRNA whereas the VCaP cancer cell line highly expressed LGALS3BP. C_T values were normalized to the reference gene *GAPDH* and to the RWPE-1 cell line. Data are shown as $\log_2$FC (fold change) and represent means ± standard deviation of two replicates. (Raw data: Andrea Wunderlich). * p<0.05 and ** p<0.01 compared to RWPE-1 cells in two-tailed t-test. Dotted lines indicate the cut-off for differential gene expression at $|\log_2 FC| \geq 0.6$. **(b)** Immunoblotting of LGALS3BP revealed highly elevated LGALS3BP protein levels in VCaP cells and low levels in PC-3, LNCaP and DU-145 cells compared to RWPE-1 control cells. LGALS3BP protein levels were normalized to the β-actin loading control and plotted in the bar chart after densitometric ImageJ analysis. **(c)** Compared to the RWPE-1 control cells, DU-145, LNCaP and PC-3 cells exhibited amplified centrin2-positive structures in immunofluorescence microscopy. VCaP cells displayed dispersed pericentriolar material (PCM) as

labelled by γ-tubulin. Centrin2-immunolabelling is shown in green, γ-tubulin-labelling in red and DAPI-stained DNA in blue in the composite images. The scale bar represents 5 µm. **(d)** The bar chart displays the quantification of supernumerary centrin2-positive structures (>4 per cell) in DU-145, LNCaP and PC-3 prostate cancer cells compared to RWPE-1 control cells. **(e)** The ImageJ quantification of the PCM area per cell in RWPE-1 control and VCaP prostate cancer cells is presented by this bar chart. **(d,e)** The bar charts show means ± standard deviation of triplicates with $n>200$ in (d) and $n>100$ in (e) for each experiment. * $p<0.05$, ** $p<0.01$ and **** $p<0.0001$ compared to RWPE-1 cells in two-tailed t-test, assuming unequal variances.

QPCR studies within the collaboration with Andrea Wunderlich and Stefan Börno revealed differential expression of *LGALS3BP* mRNA in certain prostate cancer cell lines. The *TMPRSS2:ERG*–negative prostate cancer cell lines DU-145, LNCaP and PC-3, for instance, displayed significantly decreased *LGALS3BP* mRNA levels compared the normal prostate epithelial cell line RWPE-1. The *TMPRSS2:ERG*–positive prostate cancer cell line VCaP, on the other hand, exhibited significantly elevated *LGALS3BP* levels (Figure 23a). In agreement with the mRNA levels, the LGALS3BP protein levels were reduced in DU-145, LNCaP and PC-3 cells and augmented in VCaP cells compared to RWPE-1 cells as detected by LGALS3BP-immunoblotting (Figure 23b).

After the validation of LGALS3BP deregulation in these cell lines immunofluorescence microscopy analysis was performed regarding centrosomal anomalies. For this purpose, centrioles were labelled with an anti-centrin2 antibody and the PCM was labelled with anti-γ-tubulin.

The RWPE-1 prostate control cell line displayed two to four centrin2 foci per cell depending on the cell cycle stage. The PCM marker γ-tubulin localized to the centrioles with one focus detected in G1-phase and two foci in G2-phase. However, the prostate cancer cell lines DU-145, LNCaP and PC-3 with decreased LGALS3BP levels exhibited supernumerary centrin2-positive structures while γ-tubulin-labelling appeared normal compared to RWPE-1 cells. VCaP cells with elevated LGALS3BP protein levels, however, showed centrioles of normal appearance with scattered PCM (Figure 23c). These phenotypes strongly resembled those upon LGALS3BP depletion and exogenous upregulation as previously described. Quantification of excess centrin2 foci revealed that these structures significantly occurred in ≈ 55 % of DU-145 cells, ≈ 25 % of LNCaP cells and ≈ 45 % of PC-3 cells (Figure 23d). VCaP cells significantly possessed ≈ 60 % larger centrosomes than RWPE-1 prostate control cells as evaluated by ImageJ macro-based quantification of γ-tubulin-labelling (Figure 23e).

Furthermore, the breast adenocarcinoma cell line SK-BR-3 was analysed because it expresses high levels of LGALS3BP (www.proteinatlas.org). The mammary epithelial cell line MCF-10A with normal LGALS3BP expression served as a control.

To examine centrosomes and LGALS3BP localization via immunofluorescence microscopy, the cells were antibody-labelled for γ-tubulin and LGALS3BP after pre-fixation extraction. Endogenous LGALS3BP again localized to centrosomes in MCF-10A cells (Figure 24a, first row). In comparison, the SK-BR-3 cells showed prominent accumulation of endogenous LGALS3BP in the centrosomal area.

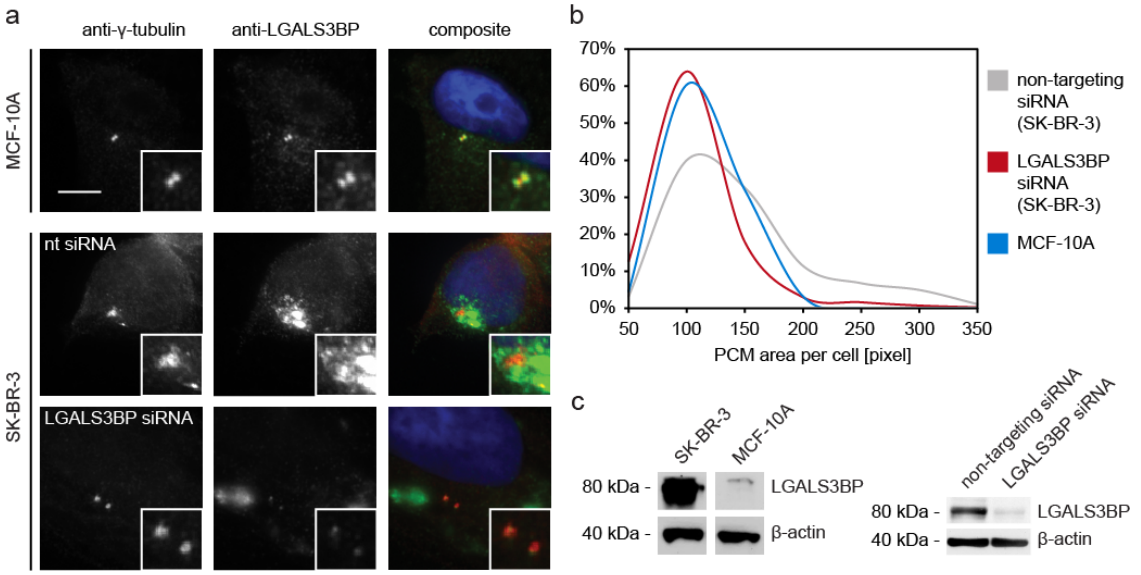

Figure 24: LGALS3BP depletion rescues PCM dispersion in breast cancer cells with high LGALS3BP expression

(a) Compared to the control breast epithelial cell line MCF-10A the breast cancer cell line SK-BR-3 endogenously overexpressed LGALS3BP and exhibited dispersion of pericentriolar material (PCM) given by γ-tubulin. In immunofluorescence microscopy SK-BR-3 cells transfected 72 h with a siRNA pool targeting LGALS3BP showed smaller and more focused centrosomes compared to SK-BR-3 cells transfected with a non-targeting siRNA pool as negative control. Immunolabelling of γ-tubulin is shown in red, endogenous LGALS3BP in green and DAPI-stained DNA in blue in the composite images. The scale bar represents 5 µm. **(b)** ImageJ quantification of total PCM area per cell revealed a reduction of PCM area in SK-BR-3 cells after LGALS3BP depletion up to control ranges of MCF-10A cells. The data derived from triplicate measurements of each $n > 200$. **(c)** Immunoblotting of LGALS3BP showed augmented protein levels in SK-BR-3 cells compared to normal levels in MCF-10A cells (left panel) as well as the validation of LGALS3BP knockdown efficiency in SK-BR-3 cells (right panel). As a loading control β-actin was used in both experiments. Figure modified from Fogeron *et al.*[128]

Additionally, the PCM defined by γ-tubulin-labelling appeared disrupted with an enlarged PCM area compared to MCF-10A cells (Figure 24a, second row). Furthermore, western blotting confirmed highly elevated LGALS3BP protein levels in SK-BR-3 cells as compared to MCF-10A cells (Figure 24c, left blot). Therefore, the centrosome

morphology of SK-BR-3 cells closely resembled that of the VCaP prostate cancer cell line and HEK293T cells upon exogenous LGALS3BP overexpression.

A next question was if the dispersed PCM area in SK-BR-3 cells is depending on LGALS3BP levels. To deplete LGALS3BP, SK-BR-3 cells were transfected for 72 h with a LGALS3BP siRNA pool and with a non-targeting siRNA pool as a control.

Immunofluorescence microscopy revealed more focused centrosomes in LGALS3BP-depleted SK-BR-3 cells compared to non-targeting siRNA-transfected SK-BR-3 cells. Moreover, the centrosomal LGALS3BP fluorescence signal decreased to a great extent with a minor LGALS3BP signal still detectable at centrosomes (Figure 24a, last row). Immunoblotting of LGALS3BP confirmed an efficient depletion in this experiment (Figure 24c, right blot). To validate the reduction of PCM hypertrophy in SK-BR-3 cells upon LGALS3BP knockdown in comparison with MCF-10A cells, the area of γ-tubulin-labelling was measured in pixels utilizing an ImageJ macro on immunofluorescence micrographs of the respective cells. Plotting the data in histograms revealed larger PCM areas in control-transfected SK-BR-3 cells compared to MCF-10A cells (Figure 24b and Supplemental Figure 3a). Depletion of LGALS3BP in SK-BR-3 cells, however, led to a notable shift towards a smaller PCM area comparable to the results measured in MCF-10A cells and thus represented a rescue of PCM hypertrophy. The rescue was further verified by a second experiment using the pericentriolar marker pericentrin additionally to of γ-tubulin (Supplemental Figure 3c).

3.2.5 Analysis of LGALS3BP phosphorylation

Phosphorylation plays an important regulatory role for centrosome structure and function[40,49,52–54,92,284,287–293]. Since LGALS3BP was shown to be a centriole-associated protein with functions in centrosome integrity, it suggested itself to examine its phosphorylation status.

First, phosphorylation of LGALS3BP was analysed via immunoblotting in mitotic and interphase U2OS cells. For this purpose, mitotic cells were collected by shake-off after a thymidine-nocodazole block and the left-over interphase cells were harvested after trypsinization. Cells were then lysed in the presence of protease and phosphatase inhibitors to preserve phosphorylated portions of LGALS3BP.

Under these conditions, immunoblotting of endogenous LGALS3BP revealed a ≈ 20 kDa higher molecular band additionally to the band of LGALS3BP at ≈ 80 kDa in mitosis and interphase (Figure 25a).

To ascertain if the ≈ 20 kDa higher molecular band represents a phosphorylated pool of LGALS3BP, U2OS cells were lysed in the absence of phosphatase inhibitors and then incubated for 30 min with calf intestinal alkaline phosphatase (CIP). Cell lysate with phosphatase inhibitors and no CIP-treatment was applied as a negative control.

The application of CIP to the cell lysate led to a weakened band at ≈ 100 kDa as detected by LGALS3BP-immunolabelling, although the main band of LGALS3BP appeared weaker, too, when compared to control lysates.

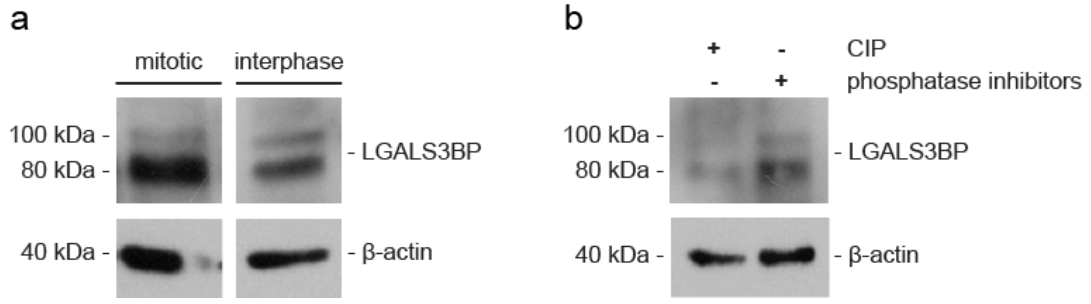

Figure 25: LGALS3BP phosphorylation in interphase and in mitosis
(a) U2OS cells were arrested in mitosis by thymidine-nocodazole block and collected by shake off. The remaining interphase cells were harvested upon trypsinization. Lysis of the cells and immunoblotting were performed in the presence of phosphatase inhibitors. LGALS3BP-immunolabelling detected a ≈ 20 kDa higher molecular band additionally to the LGALS3BP band at ≈ 80 kDa. **(b)** The higher molecular band of LGALS3BP weakened after incubating U2OS cell lysate with calf-intestinal alkaline phosphatase (CIP). **(a,b)** LGALS3BP was detected with a specific rabbit LGALS3BP-antibody and β-actin served as a loading control.

To discover kinases responsible for LGALS3BP phosphorylation, three phosphorylation sites were further analysed because they were listed already on www.phosphosite.org (S256, S444) and www.phosida.com (T220). These phosphorylation sites were entered into two different kinase motif finder platforms (PhosphoNET and KinasePhos2.0, respectively) to find best matching kinases by algorithm. The kinases AKT1, CaMK4, CHK1, CHK2, CK1d, and PLK1 were chosen because they showed high prediction scores. In the following, the Kinexus corporation was assigned to synthesize wild type peptides of LGALS3BP incorporating the annotated phosphorylation site as well as the corresponding phospho-mutant peptides, in which the phosphorylatable serine or threonine was exchanged by a non-phosphorylatable alanine. Additionally, Kinexus

profiled the wild type and phospho-mutant peptides against the kinases using a radiometric assay method.

Profiling of the T220 LGALS3BP peptide against the AKT1 kinase revealed 84 % more counts per minute when compared to the phospho-mutant A220 peptide indicating a high phosphorylation rate of the wild type peptide (Table 14). In this context, CK1d and PLK1 kinases showed weak phosphorylation (22 % and 17 %) of the wild type peptide when compared to the phospho-mutant peptides.

Table 14: The T220 peptide is highly phosphorylated by AKT1 compared to the phospho-mutant.
In vitro activities of AKT1, CK1d, and PLK1 kinases in the presence of wild type and mutant LGALS3BP peptides T220 and A220 were obtained using a radioisotope assay format. Averaged and blank-corrected measurements are given as counts per minute (cpm). The difference in counts between wild type (wt) and mutant (mt) peptides (T220 - A220) is also given as % change from the phospho-mutant control (CFC). The positive control verified the activity of the applied kinases.

Kinase	Positive control	T220 (wt)	A220 (mt)	Δ T220 - A220	
	[cpm]	[cpm]	[cpm]	[cpm]	CFC [%]
AKT1	134,656	8,874	1,413	7,461	84
CK1d	57,692	6,208	4,826	1,382	22
PLK1	51,216	1,565	1,305	260	17

Profiling the S256 phosphorylation site against the AKT1, CaMK4, CHK1, and CHK2 kinases only resulted in weak phosphorylation (37 %) of the synthetic S256 peptide by CHK1 when compared to the A256 phospho-mutant peptide (Table 15). AKT1, CaMK4, and CHK2 kinases did not phosphorylate the wild type peptide though.

Table 15: CHK1 weakly phosphorylates the LGALS3BP S256 peptide.
In vitro kinase activities of AKT1, CaMK4, CHK1 and CHK2 in the presence of wild type and mutant LGALS3BP peptides S256 and A256 were obtained by radiometry. Kinase activities were averaged, blank-corrected and given as counts per minute (cpm). The difference in counts between wild type (wt) and mutant (mt) peptides (Δ S256 - A256) is also given as % change from the phospho-mutant control (CFC). All kinases were active in this assay as given by the positive control.

Kinase	Positive control	S256 (wt)	A256 (mt)	Δ S256 - A256	
	[cpm]	[cpm]	[cpm]	[cpm]	CFC [%]
AKT1	134,656	38	0	38	-
CaMK4	174,417	348	356	-8	-
CHK1	165,948	2,624	1,658	966	37
CHK2	125,122	0	3	-3	-

The profiling of LGALS3BP S444 wild type peptide and A444 phospho-mutant peptide against AKT1, CaMK4, CHK1, CHK2 and PLK1 kinases revealed moderate phosphorylation of the S444 peptide by CaMK4 (59 %) and no phosphorylation by AKT1 and PLK1 as compared to the phospho-mutant (Table 16). CHK1 and CHK2, on the other hand, highly phosphorylated the S444 wild type peptide (85 % and 98 %) in comparison to the A444 phospho-mutant peptide.

Table 16: The LGALS3BP S444 peptide is highly phosphorylated by CHK1 and CHK2.
Radiometric profiling of AKT1, CaMK4, CHK1, CHK2 and PLK1 kinases in the presence of wild type and mutant LGALS3BP peptides S444 and A444 revealed high phosphorylation levels for CHK1 and CHK2. The *in vitro* kinase activities were averaged, blank-corrected and given as counts per minute (cpm). The difference in counts between wild type (wt) and mutant (mt) peptides (Δ S444 - A444) is also given as % change from the phospho-mutant control (CFC).The positive control verified proper activities of the tested kinases in this assay.

Kinase	Positive control [cpm]	S444 (wt) [cpm]	A444 (mt) [cpm]	Δ S444 - A444 [cpm]	Δ S444 - A444 CFC [%]
AKT1	134,656	20	73	-53	-
CaMK4	174,417	3,840	1,562	2,278	59
CHK1	165,948	50,871	7,606	43,265	85
CHK2	125,122	2,860	57	2,803	98
PLK1	51,216	950	1,042	-92	-

Summing up the results of the *in vitro* kinase assays, LGALS3BP wild type peptides were able to be phosphorylated by certain kinases. Especially AKT1, CHK1 and CHK2 represented suitable kinases for further phosphorylation studies on LGALS3BP since they displayed the highest phosphorylation rates and were also reported to affect centrosome number[294] or to localize at centrosomes[70,295].

3.3 Regulation of LGALS3BP expression

3.3.1 LGALS3BP expression depended on BRD4

The previous results pointed out a role of LGALS3BP in centrosome integrity as well as a strong correlation between deregulated LGALS3BP expression and centrosomal aberrations in cancer. Especially in relation to cancer it was of interest to understand

the regulation of LGALS3BP expression since this could possibly allow pharmaceutical intervention in cancer progression.

The collaboration with Andrea Wunderlich was initiated because LGALS3BP was one of the top downregulated genes upon BRD4 depletion in HEK293T cells as resulted from mRNA sequencing analysis during her studies in Michal-Ruth Schweiger's group[296]. Moreover, an Ingenuity Pathway Analysis (QIAGEN) of the BRD4 knockdown mRNA sequencing data displayed interferon signalling as the most significantly affected pathway in this study (Supplemental Figure 4)[296]. As *LGALS3BP* represents an INFγ-stimulated gene[161,163], we decided to include STAT1 into the further analysis since it mediates the cellular INFγ response by forming homodimers[297,298]. Due to these findings it was of interest for us how BRD4 influences LGALS3BP expression and if BRD4 affects the INFγ response of LGALS3BP upon stimulation.

To address these questions, we performed isoform-specific depletion of BRD4 in HEK293T cells and analysed mRNA and protein levels as well as promoter activities in INFγ-stimulated and unstimulated backgrounds. An isoform-specific BRD4 knockdown was achieved by 72 h shRNA-transfection, which targets either both isoforms of BRD4 (shC2) or only the long isoform of BRD4 (shE1, Figure 26a). ShGFP served as a negative control.

Quantitative real-time PCR was performed to analyse mRNA expression in HEK293T cells with the resulting data being normalized to *HPRT1* reference gene expression and to shGFP-transfected cells. Thereby, BRD4-depleted HEK293T cells revealed significantly downregulated mRNA levels of *BRD4*, *STAT1* and *LGALS3BP* (Figure 26b). Precisely, considering the isoform-specific depletion of BRD4, shC2-transfection led to a 2.1 – 4.4 fold downregulation of *BRD4* as detected with primers for both *BRD4* variants and to a 2.2 – 3.4 fold downregulation of the long *BRD4* isoform. Transfection with shE1 resulted in 4.5 – 6.5 fold downregulation of both *BRD4* variants and mRNA levels of the long *BRD4* isoform decreased 2.6 – 4.7 fold. *STAT1* and *LGALS3BP* mRNA levels were more downregulated after shC2-transfection (4.8 – 7.3 and 25.6 – 40.4 fold downregulation) compared to shE1-transfected HEK293T cells (1.8 – 2.7 and 4.1 – 5.6 fold downregulation). Additionally, western blot analysis of this experiment showed downregulation of STAT1 and LGALS3BP protein levels (Figure 26c). The STAT1 band at

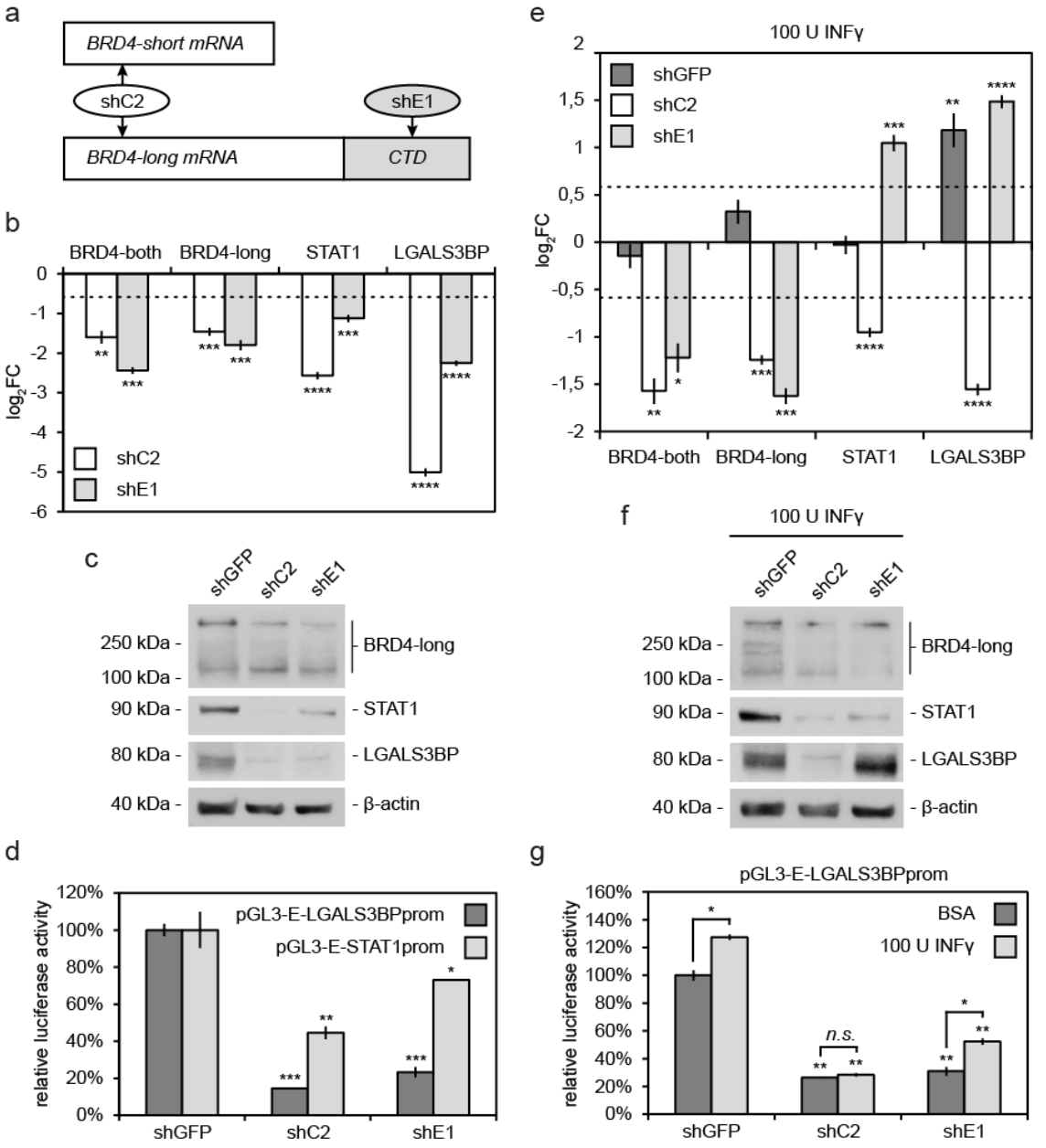

Figure 26: BRD4 regulates LGALS3BP expression and mediates the INFγ response of LGALS3BP
HEK293T cells were specifically depleted for two different BRD4 variants for 72 h. Additionally, this experiment was carried out with 100 U INFγ stimulation for 48 h. **(a)** The schematic illustrates two different shRNAs applied for isoform-specific depletion of BRD4. ShC2 targets an N-terminal region present in both isoforms of BRD4 and shE1 targets the C-terminal domain (CTD), which is only present in the long isoform of BRD4. **(b)** QPCR analysis of relative *BRD4*, *STAT1* and *LGALS3BP* expression after isoform-specific depletion of BRD4. C_T values were normalized to reference gene *HPRT1* and negative control-treatment with shGFP. Data are shown as log_2FC (fold change) and represent means ± standard deviation of four replicates. The non-log_2-transformed values of fold changes can be found in the main text. A two-tailed t-test was applied compared to shGFP-treated cells. **(c)** Immunoblotting of the long BRD4 variant, STAT1 and LGALS3BP after isoform-specific BRD4 knockdown with shGFP serving as a negative control and β-actin-immunolabelling as a loading control. **(d)** Dual luciferase reporter assay of *LGALS3BP* and *STAT1* promoter constructs after BRD4 knockdown. Firefly luciferase activity of pGL3-E-promoter constructs was normalized to sea pansy luciferase activity of co-expressed pRL-TK vector and to pGL3-E empty vector. The relative luciferase activities are presented as means ± standard deviation of two replicates with a two-tailed t-test being applied compared to shGFP-transfected cells. **(e)** QPCR analysis of *BRD4*, *STAT1* and *LGALS3BP* expression after BRD4 knockdown with INFγ

stimulation. C_T values were normalized to *HPRT1* and to shGFP-transfection with BSA-treatment as a negative control. Data represent means ± standard deviation of four replicates and are displayed as $\log_2$FC. The non-$\log_2$-transformed fold changes are stated in the main text. A two-tailed t-test was applied compared to the negative control. **(f)** Immunoblotting of BRD4, STAT1 and LGALS3BP after BRD4 knockdown with INFγ stimulation. Transfection of shGFP served as negative control and β-actin-labelling as loading control. Immunoblots in (c) and (f) show cuttings of the same membrane with the very same exposure times. **(g)** Dual luciferase reporter assay of the *LGALS3BP* promoter construct after BRD4 depletion with INFγ stimulation as opposed to BSA control-treatment. Firefly luciferase activity was normalized to sea pansy luciferase activity and to pGL3-E empty vector control. The relative luciferase activities are given as means ± standard deviation of two replicates with a two-tailed t-test being applied compared to shGFP-transfected cells. Raw data were provided by Andrea Wunderlich. Dotted lines in qPCR plots indicate the cut-off criterion for differential gene expression at $|\log_2 FC| \geq 0.6$. **** $p<0.0001$, *** $p<0.001$, ** $p<0.01$, * $p<0.05$ and *n.s.* not significant.

90 kDa after shE1-transfection did not appear as weak as after shC2-transfection but still weaker compared to the negative control, which could be explained by the slight 1.8 – 2.7 fold downregulation of the STAT1 mRNA levels. Furthermore, the analysis of *STAT1* and *LGALS3BP* promoter activities via luciferase reporter assay revealed reduced promoter activities after BRD4 knockdown as compared to negative control (Figure 26d). The *LGALS3BP* promoter activities were significantly reduced to 14 % after shC2-mediated BRD4 knockdown and to 23 % after shE1-mediated BRD4 knockdown as compared to the 100 % activity of the negative control. This fundamentally confirmed the results of the qPCR and western blot analysis. The *STAT1* promoter activities after BRD4 knockdown, however, were not as strongly reduced as the LGALS3BP promoter activities. ShC2-transfection of the cells led to a *STAT1* promoter activity of 44 % and shE1-transfection to a promoter activity of still 73 %. This might explain the weaker reduction in *STAT1* mRNA expression and the stronger STAT1 protein band observed by immunoblotting after shE1-transfection compared to shC2-mediated depletion of BRD4.

Subsequently, the experiments were repeated with INFγ stimulation. For this purpose, the shRNA-transfected cells were added 100 U of INFγ 48 h before harvest. ShGFP-transfection and 0.1 % BSA-treatment served as negative control.

First of all, qPCR was performed with following data normalization on the reference gene *HPRT1* and shGFP-transfection combined with BSA-treatment.

The analysis of mRNA expression via qPCR revealed no significant impact of INFγ on *BRD4* mRNA levels after shGFP-transfection in INFγ-stimulated cells (Figure 26e). BRD4 knockdown via shC2 as well as shE1-transfection led to a significant decrease in mRNA expression as detected with primers for either both *BRD4* isoforms (1.6 – 4.0 fold

downregulation) or for the long isoform of *BRD4* (2.1 – 3.7 fold downregulation) after INFγ stimulation. Surprisingly, INFγ did not increase *STAT1* mRNA expression under control knockdown conditions. Interestingly, shC2-transfection led to a significant reduction of *STAT1* mRNA levels (1.7 – 2.2 fold downregulation) whilst a significant increase was observed after shE1-transfection (1.7 – 2.5 fold upregulation). *LGALS3BP* expression was significantly upregulated (1.5 – 3.4 fold change) after INFγ stimulation in the control knockdown. However, INFγ stimulation in the shC2 background led to a significant 2.6 – 3.4 fold downregulation of *LGALS3BP* expression and a significant 2.4 – 3.3 fold upregulation in the shE1-transfected cells.

Western blot analysis of this experiment verified the isoform-specific depletion of BRD4 and the qPCR results as detected with an antibody targeting the long BRD4 variant (Figure 26f). Interestingly, the STAT1 protein levels appeared augmented in INFγ-stimulated and shGFP-transfected cells (Figure 26f) when compared to unstimulated cells (Figure 26c), which contradicted the qPCR results. On the other hand, both types of BRD4 depletion in INFγ-stimulated cells led to a decrease of STAT1 protein levels as compared to the stimulated and unstimulated shGFP control (Figure 26c, f). So again, at least the STAT1 protein levels of INFγ-stimulated and shE1-transfected cells countered the respective qPCR results. The detected LGALS3BP protein levels, however, supported the respective qPCR results. LGALS3BP protein expression was augmented after INFγ stimulation in the control knockdown when compared to the unstimulated background (Figure 26c, f) whilst shC2-transfected cells showed downregulation of LGALS3BP and LGALS3BP levels were increased even more after shE1-transfection as compared to the shGFP control.

Parts of these findings could be explained by the analysis of LGALS3BP promoter activity via luciferase reporter assay. As compared to the BSA-treated control cells, INFγ stimulation in shGFP-transfected cells led to a significant increase of *LGALS3BP* promoter activity up to ≈ 127 % (Figure 26g). ShC2-transfection significantly decreased the promoter activity although no difference was detected between INFγ-stimulated (≈ 28 %) and unstimulated cells (≈ 26 %). There was a significant difference in LGALS3BP promoter activity between INFγ-stimulated and unstimulated cells after shE1-mediated BRD4 knockdown (≈ 21 %), but promoter activities remained significantly decreased and INFγ stimulation did not lead to an activity greater than

100 % as it would have been expected regarding the immunoblots. Nevertheless, the short isoform of BRD4, which remained after shE1 transfection, seemed to mediate *LGALS3BP* promoter activation upon INFγ stimulation.

All in all, these findings suggested a role of BRD4 in the regulation of *STAT1* and *LGALS3BP* promoter activity, which in turn affected mRNA and protein expression. Concerning LGALS3BP, these results indicate that the INFγ response of LGALS3BP expression could be mediated by the short isoform of BRD4.

3.3.2 LGALS3BP expression was regulated through methylation

Quite recently, Börno *et al*. discovered differential global methylation patterns in *TMPRSS2:ERG* gene fusion-positive and -negative prostate cancers via microarray-based gene expression analysis (Affymetrix) and methylation profiling (MeDIP-Seq)[243]. The fusion-negative tumours showed significantly more methylation events on a global level compared to fusion-positive cancer and control tissue[243]. They confirmed an upregulation of the histone methyltransferase EZH2 in both cancer backgrounds and concluded that it is caused by either the well-described ERG-driven mechanism in fusion-positive prostate cancer[269] or by hypermethylation-mediated epigenetic silencing of the EZH2 negative regulator *miR26a* in fusion-negative prostate cancer that they identified in their study[237,243].

The collaboration with Stefan Börno *et al.* was started, because *LGALS3BP* downregulation correlated with the *EZH2* upregulation in their prostate cancer data set (not published).

Microarray-based gene expression profiling of normal and prostate cancer tissue revealed significantly elevated *EZH2* expression in the cancer tissues compared to normal samples. *EZH2* displayed even higher expression rates in fusion-negative samples when opposed to normal and fusion-positive tissue samples[243] (Figure 27a). *LGALS3BP* expression, on the other hand, showed significantly lowered expression in the fusion-negative samples as compared to normal and *TMPRSS2:ERG* fusion-positive prostate cancer tissue (Figure 27b). Due to these findings, we took a closer look on the LGALS3BP promoter region within the MeDIP-Seq data set. Correlating with the *EZH2* expression CpG methylation within the *LGALS3BP* promoter region (500 bp upstream

of transcription start site) was significantly increased in the cancer samples when compared to normal tissue. Compared to fusion-positive cancers, this *LGALS3BP* promoter region was even stronger methylated in fusion-negative samples, which could explain the low expression rates by promoter silencing (Figure 27c).

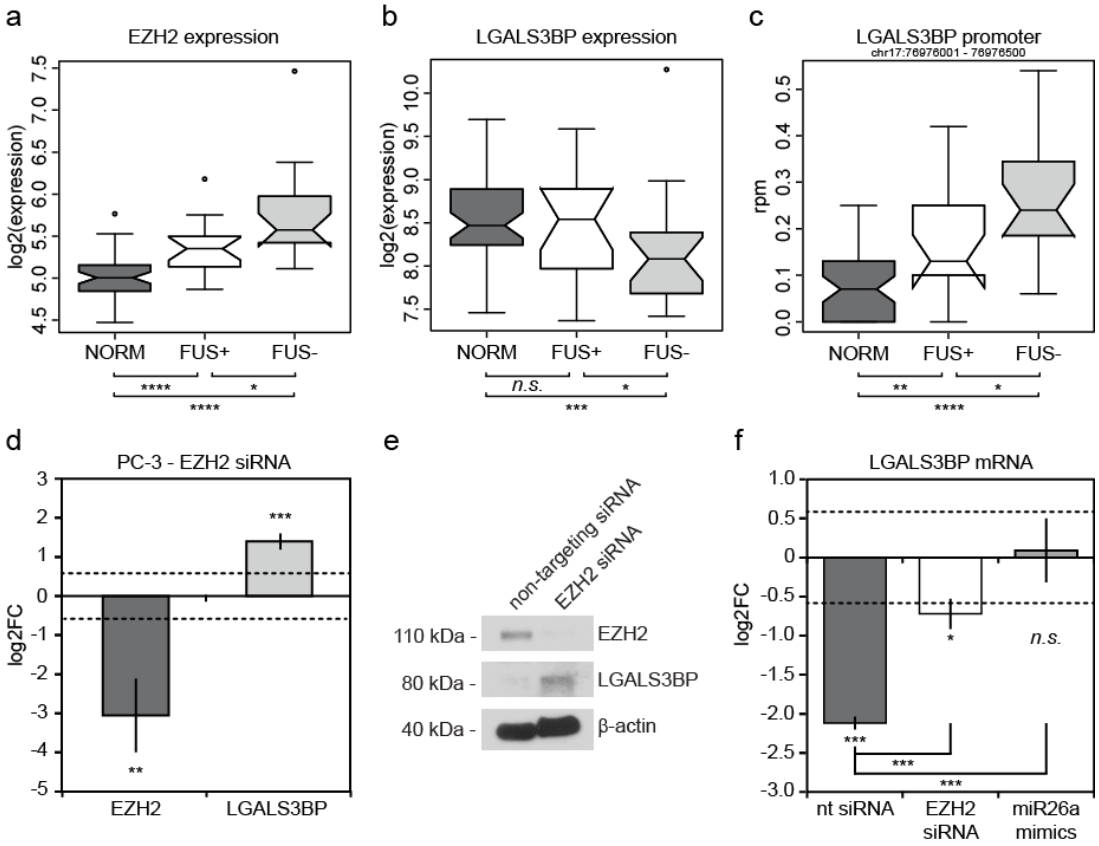

Figure 27: LGALS3BP expression is regulated by EZH2

(a,b) The boxplots show microarray-based analysis of *EZH2* (a) and *LGALS3BP* (b) gene expression in *TMPRSS2:ERG* fusion-positive (FUS+) and -negative (FUS-) prostate cancer samples in comparison to normal prostate control tissue (NORM). Data are given as $\log_2$ values of array signals. **(c)** Analysis of LGALS3BP promoter methylation via MeDIP-Seq revealed differential methylation among FUS+ and FUS- prostate cancer samples compared to normal prostate control tissue. Data show a region within the *LGALS3BP* promoter 500 bp upstream of the transcription start site and are given as MeDIP-Seq values (rpm). Sequence was mapped on human genome 19 (HG19). **(a-c)** Data displayed by boxplots show pools of FUS+ cancers (n = 17), FUS- cancers (n = 20) as well as normal prostate tissue (n = 53). Data were tested for significance by multiple 2-tailed Mann-Whitney tests with Benjamini-Hochberg-corrected values. **** p<0.0001, *** p<0.001, ** p<0.01, * p<0.05 and *n.s.* not significant. Experiments were performed by Börno *et al.*[243] **(d)** Data represent qPCR results of *EZH2* and *LGALS3BP* mRNA expression in PC-3 fusion-negative prostate cancer cells transfected for 72 h with siRNA targeting *EZH2*. Non-targeting siRNA served as a negative control in this experiment. C_T values were normalized to *GAPDH* and non-targeting siRNA control. **(e)** Analysis of EZH2 and LGALS3BP protein levels via immunoblotting of PC-3 cell lysates previously transfected with *EZH2*-targeting siRNA. Non-targeting siRNA served as a negative control and β-actin as a loading control. **(f)** *LGALS3BP* mRNA expression analysis via qPCR of PC-3 prostate cancer cells after 72 h of *EZH2* siRNA and *miR26a* mimics transfection. Non-targeting siRNA served as a negative control. C_T values were normalized to *GAPDH* and to the RWPE-1 prostate control cell line. **(d,f)** Data represent means ± standard deviation of three replicates and are displayed as log2 of fold change ($\log_2$FC). The non-$\log_2$-transformed fold changes are stated in the main text. A two-tailed t-test was applied compared to the respective negative control with *** p<0.001, ** p<0.01, * p<0.05 and *n.s.* not significant. Dotted lines indicate the cut-off for differential gene expression at $|\log_2 FC| \geq 0.6$. QPCRs were performed by Andrea Wunderlich.

Next, we asked whether EZH2 depletion in a *TMPRSS2:ERG* fusion-negative background could influence LGALS3BP expression. Considering that question, we analysed the fusion-negative prostate cancer cell line PC-3 because it showed elevated *EZH2* expression[243] and low *LGALS3BP* expression (Figure 23a, b).

Hence, PC-3 cells were transfected for 72 h with siRNA targeting *EZH2* and LGALS3BP expression was analysed by qPCR and western blotting. Non-targeting siRNA served as a negative control.

Thereby, *EZH2* mRNA expression was significantly lowered (4.4 – 15.7 fold downregulation) and *LGALS3BP* mRNA expression significantly increased (2.3 – 3.0 fold upregulation) as compared to the negative control (Figure 27d). These findings were confirmed by western blot analysis as EZH2 protein levels were distinctly decreased after EZH2 knockdown with LGALS3BP protein levels being clearly elevated in comparison to the negative control (Figure 27e).

Analysis of *LGALS3BP* mRNA levels by qPCR unveiled a 4.2 – 4.6 fold downregulation in non-targeting siRNA-transfected PC-3 prostate cancer cells when related to RWPE-1 prostate control cells (Figure 27f). A siRNA-mediated depletion of EZH2 in these cells led to a significant increase of *LGALS3BP* gene expression compared to non-targeting siRNA control albeit it was still 1.5 – 1.9 fold downregulated in relation to RWPE-1 cells. Transfection of PC-3 cells with *miR26a* mimics, on the other hand, significantly elevated *LGALS3BP* mRNA levels to an extent that was not significantly different to RWPE-1 prostate control cells anymore.

Finally, these findings indicate that LGALS3BP downregulation in a *TMPRSS2:ERG* fusion-negative prostate cancer background could be regulated by targeting the histone methyltransferase *EZH2* either directly or via *miR26a*.

4. Discussion

4.1 A protein interaction network identifies centrosomal LGALS3BP

LGALS3BP was identified by our group via tandem affinity purification mass spectrometry (TAP-MS) within a protein-protein interaction network among 23 centrosomal and cell cycle-regulatory proteins[128]. High confidence interactions with LGALS3BP were shown for C-Nap1 (CEP250), GCP3 (TUBGCP3) and the newly identified MAGED2, which were further verified by immunoprecipitation approaches.

TAP-MS represents a powerful tool for protein complex analysis, since native protein complexes can be isolated *in vivo* and highly enriched because of the two-step purification procedure[299,300]. However, epitope-tag affinity purification approaches display some limitations as reviewed by Chang[301]. Firstly, the expression of the tagged bait proteins must be high enough to enable an efficient protein purification yielding a sufficient amount of proteins for mass spectrometry analysis. Secondly, the epitope tag has to be sterically available to ensure affinity purification. Additionally, tagging either the N- or C-terminus of the bait protein may intervene in the natural localization and the interacting proteins may thus be different. Thirdly, it is possible that the tagged bait protein competes with the endogenous protein for binding to the interacting proteins, which may lower purification efficiency. Fourthly, the conformation of the bait protein or its charge state may be changed by tagging and may thus interfere with binding to the interaction partner.

Certain attempts were made by our group to address these limitations[128]. First of all, stably transfected FlpIn TRex 293 cells with high CMV promoter-driven bait expression were used for the study to ensure sufficient purification efficiencies. Afterwards, the complexity of interacting proteins as well as their enrichment in TAP eluates of bait proteins was strictly compared against the negative controls by Coomassie-staining of 1 cm SDS-PAGE gels and further analysed via mass spectrometry[128]. Our centrosomal protein interaction network is of high quality since also known interaction partners were found and reverse TAP experiments, bidirectional co-immunoprecipitation as well as tag-immunoprecipitation further validated the interactions[128].

LGALS3BP has previously been shown to interact with the γ-TuRC as detected by TAP-MS analysis of mitotic protein complexes in HeLa cells[282], however, neither centrosomal localization nor function has been reported before. The present study strikingly confirmed a centrosomal localization of LGALS3BP by several approaches and in several cell lines. In immunofluorescence microscopy, the localization close to the proximal part of centrioles, as given by the proximity of procentrioles, was shown in human osteosarcoma U2OS cells by antibody-labelling of endogenous LGALS3BP and by transient expression of the FLAG-tagged protein[128], which was further confirmed in the mammary epithelial cell line MCF-10A. Additionally, exogenously overexpressed myc- or FLAG-tagged LGALS3BP localized to centrosomes of HEK293 cells[128]. Transmission electron microscopy of pre- and post-embedding immunogold-labelling of LGALS3BP in U2OS cells independently validated the localization of LGALS3BP to the proximal part of centrioles[128]. Moreover, induction of centriole overduplication by PLK4 overexpression led to amplified LGALS3BP foci locating to the newly formed centrioles, which further confirms the connection of LGALS3BP to centrioles and indicates that LGALS3BP might be a relevant part of them.

Interestingly, antibody-labelling of endogenous LGALS3BP in U2OS cells appeared remarkably weak in mitosis as detected by immunofluorescence microscopy. This might be observed because centrosomes acquire additional PCM components upon maturation at the onset of mitosis and LGALS3BP was thus not reachable by the antibody[287]. However, this is unlikely as cells were pre-extracted before fixation to facilitate antibody accessibility. Another reason could be posttranslational modifications so that LGALS3BP is not recognised by the antibody or LGALS3BP itself loses its centrosomal association in a cell cycle-dependent manner. A more plausible explanation could be derived from the identified interaction between LGALS3BP and C-Nap1. To enable centrosome disjunction in late G2 phase, C-Nap1 at the proximal part of centrioles is removed by Nek2-mediated phosphorylation. Also within the present study, a reduced immunolabelling of C-Nap1 at mitotic centrosomes was observed by immunofluorescence microscopy (Supplemental Figure 2) and, importantly, LGALS3BP and C-Nap1 were shown to colocalize at the proximal part of centrioles. Together with the result that anti-LGALS3BP fluorescence intensities significantly decreased upon C-Nap1 knockdown, this suggests that centrosomal

localization of LGALS3BP depends on C-Nap1 and might therefore be reduced in mitosis due to C-Nap1 dissociation from centrosomes.

For the newly identified MAGED2 it is quite similar. MAGED2 was shown to interact with LGALS3BP, C-Nap1 (CEP250), GCP3 (TUBGCP3) and p53 (TP53) at high confidence level. Additionally, it showed candidate interactions with γ-tubulin (TUBG1) and tubulin polyglutamylase complex subunit 1 (TPGS1, c19orf20). The centrosomal localization of MAGED2 was confirmed by our group[128]. Additionally, MAGED2 showed speckled localization within the nucleus. Neither MAGED2 nor LGALS3BP depletion affected centrosomal localization of MAGED2. But again, C-Nap1 knockdown removed MAGED2-labelling at centrosomes. This might indicate that MAGED2 is a stable component of centrosomes with a probable slow turnover rate, which might explain the persistence at centrosomes upon MAGED2 depletion. LGALS3BP knockdown might not affect MAGED2 localization since LGALS3BP is still weakly present at centrosomes and MAGED2 yet interacted with C-Nap1 to reside there. C-Nap1 depletion, on the other hand, might disrupt the interaction to centrioles. However, detailed localization of MAGED2 to centrioles and to the nucleus has to be further validated to exclude non-specific labelling of the applied antibody. Although MAGED2 deregulation had no impact on centrosome structure, it might be an interesting target for additional studies since it interacted with p53 in our studies and it has been reported as a negative regulator of p53 activity[302].

In conclusion, the established TAP-MS protein-protein interaction network identified new centrosomal proteins, namely LGALS3BP and MAGED2, which were notably confirmed to localize at centrosomes with C-Nap1 being necessary to that end.

4.2 LGALS3BP is required for centrosome integrity

The functional characterization of LGALS3BP by overexpression and RNA interference studies in human cell culture revealed two different centrosomal phenotypes that correlated with LGALS3BP deregulation in cancer cells. PCM hypertrophy was caused by LGALS3BP overexpression possibly due to excess PCM recruitment whilst LGALS3BP depletion led to the accumulation of supernumerary centrin2-positive structures, which did not represent structurally intact centrioles.

4.2.1 LGALS3BP overexpression and PCM hypertrophy

Exogenous overexpression of LGALS3BP in HEK239T cells resulted in localization of the overexpressed fusion protein prominently to the cell cortex and to the centrosome as detected by immunofluorescence microscopy. The cortical localization of LGALS3BP might be explained by its reported function as a secreted extracellular matrix protein[120]. Hence, LGALS3BP accumulating at the cell membrane might be antibody-labelled while the extracellular fraction has been washed off during sample preparation or was lost through secretion. Importantly, cells overexpressing tagged LGALS3BP showed dispersed PCM accumulation while untransfected neighbouring cells possessed focused centrosomes. More than 70 % of HEK293 cells displayed this phenotype independently of the three different fusion tags being used[128], which validates this phenotype. A possible explanation for the PCM hypertrophy phenotype may be potential γ-TuRC acquisition capabilities of LGALS3BP since it interacted with the γ-TuRC via GCP3. However, this could be also mediated indirectly by other LGALS3BP interacting partners. Thus, it would be of interest and remains to be tested if other LGALS3BP-interacting proteins accumulate within the centrosomal region upon LGALS3BP overexpression in these cells.

Since PCM hypertrophies among other centrosomal anomalies are often observed in cancer and known to affect microtubule nucleation[104,283,303,304], the next step was to analyse microtubule nucleation performing a microtubule regrowth assay upon LGALS3BP overexpression. Thereby, the area covered by regrowing microtubules was significantly larger after 10 min of repolymerization in LGALS3BP-YFP expressing FlpIn TRex293 cells compared to EGFP-YFP expressing control cells. This was also the case in endogenously overexpressing SK-BR-3 breast cancer cells when compared to the non-cancer mammary epithelial cell line MCF-10A with normal LGALS3BP expression. Although the observations in SK-BR-3 and MCF-10A cells might be cell line-specific, the similar results in FlpIn TRex293 cells might argue for a role of LGALS3BP in centrosomal regulation of microtubule dynamics. The excessively recruited γ-tubulin alone would not explain a rapid microtubule nucleation but rather a denser microtubule aster organized by the centrosome. However, accumulated LGALS3BP at centrosomes may recruit other regulatory proteins to modulate

microtubule dynamics (e.g. via posttranslational tubulin modifications, minus end stabilization by γ-TuRCs or other anchoring proteins, promotion of plus end elongation) or to enhance microtubule nucleation activity of γ-TuRCs acting as a γ-TuRC-mediated nucleation activator (γ-TuNA). To address these hypotheses, microtubule stabilization could be analysed e.g. by antibody detection of acetylated or glutamylated tubulin[305] or the presence or absence of microtubule-associated proteins (MAPs), which regulate microtubule polymerization or depolymerization, could be analysed by immunofluorescence microscopy. Nevertheless, LGALS3BP overexpression might also lead to a centrosomal enrichment of the adenomatous polyposis coli (APC) tumour suppressor, which has been detected at centrosomes in interphase and mitosis[306,307]. Just recently, APC has been revealed to stimulate both the formation of the core aster and the subsequent microtubule elongation in interphase cells in microtubule regrowth experiments[308].

Within our publication, microtubule regrowth was not influenced by LGALS3BP overexpression in U2OS cells as judged by aster density[128]. However, PCM hypertrophy was not detected in U2OS cells after LGALS3BP overexpression and microtubule regrowth may thus not be affected. A reasonable explanation for LGALS3BP upregulation-mediated PCM hypertrophy in FlpIn TRex293 and SK-BR-3 cells but not in U2OS cells might be cell type-specific deregulation of certain proteins that are necessary to that end. Furthermore, the experimental approach and the kind of analysis differed: within this study, microtubules were depolymerized with nocodazole and regrowth upon washout showed differences in aster areas covered by microtubules compared to the controls after 10 min in LGALS3BP-YFP-overexpressing FlpIn TRex293 and in SK-BR-3 cells. Within our publication, microtubules of U2OS cells were depolymerized on ice and fluorescence intensities within a fixed circular region centring on asters were analysed 1 min after addition of warm medium[128]. The results of both studies are thus difficult to compare but do not contradict each other.

4.2.2 Multiple centriolar structures are generated upon LGALS3BP depletion

An initial functional analysis of LGALS3BP revealed a lack of astral microtubules occasionally accompanied by additional spindle pole-like structures as well as multiple centrosome-like structures in mitotic U2OS cells after LGALS3BP knockdown[128]. Subsequent examination of centriole structure and number, which would explain the supernumerary centrosomal structures and the loss of astral microtubules, revealed an accumulation of centrin2-positive structures in mitotic and interphase U2OS cells upon siRNA-mediated LGALS3BP depletion[128]. Additionally, these centriolar structures were partly not associated with the PCM as detected by γ-tubulin-labelling in immunofluorescence microscopy[128] indicating that these structures were not capable of recruiting PCM and thus also explaining the loss of astral microtubules. Since this phenotype was reproduced by siRNA-transfection targeting alternative regions of *LGALS3BP* mRNA and rescued by expression of exogenous LGALS3BP, these findings together strongly suggest that this phenotype depends on LGALS3BP.

As the analysis of cell proliferation and cell cycle by mitotic index determination, fluorescence-activated cell sorting (FACS) and quantitative densitometry on DAPI-stained nuclei did not reveal significant differences after LGALS3BP depletion in U2OS cells compared to the respective negative control[128], it can be concluded that the supernumerary centriolar structures are unlikely to be the consequence of cell cycle deregulation.

Ultrastructural analysis of LGALS3BP-depleted U2OS cells via transmission electron microscopy unveiled, in addition to centrioles of structural integrity, a high number of defect centriolar structures represented by malformed or incomplete cylinder-like structures as well as smaller substructures of microtubule-like aggregates[128]. The phenotype thus does not resemble amplification of intact procentrioles upon centriole overduplication but rather the accumulation of immature centriolar substructures or fragments. This goes along with the centriolar marker composition of these supernumerary structures appearing upon LGALS3BP depletion: additionally to centrin2, CPAP, acetylated α-tubulin and sometimes polyglutamylated tubulins were

present at these structures whilst other markers lacked[128] suggesting that these structures represent incomplete centrioles or aggregates of centriolar proteins.

Quite recently, ATF5 was shown to connect the PCM to the proximal part of the mother centriole with ATF5 depletion resulting in centriole fragmentation, multipolar spindles and genomic instability[309]. The authors claim that ATF5 links polyglutamylated tubulins present at the proximal end of the mother centriole to pericentrin thus promoting mother centriole-directed PCM acquisition and PCM-dependent centriole formation. Although the antibody-labelling of ATF5 and LGALS3BP at centrosomes throughout cell cycle are complementary, it could be possible that also LGALS3BP, which connects the PCM via γ-TuRCs (GCP3) with centrioles (C-Nap1), mediates procentriole formation and stability.

However, the analysis of markers for maturated centrioles (glutamylated tubulin) and daughter centrioles (centrobin[285]) revealed that the number of parental and daughter centrioles was maintained upon LGALS3BP depletion compared to the negative control, whereas centrin2-positive substructures were amplified[128]. This suggests that these structures are not likely to derive from parental or daughter centriole fragmentation as described for ATF5[309].

We further unveiled that the LGALS3BP depletion phenotype depended on the centriole duplication factor PLK4 because double knockdown of LGALS3BP and PLK4 lessened the occurrence of supernumerary centriolar structures by ≈ 40 %[128]. Additionally, PLK4 knockdown as well as PLK4/LGALS3BP double knockdown resulted in a large portion of cells (75 – 85 %) containing at least one centriole after 72 h of siRNA treatment indicating that centriole duplication is abrogated in both cases[128]. The observed decrease of supernumerary centriolar structures in PLK4/LGALS3BP double-depleted cells might therefore be due to the lack of procentrioles generated since PLK4 was absent. Quite unexpectedly, LGALS3BP depletion in stably PLK4-overexpressing U2OS cells did not lead to a further increase of amplified centrin2-positive structures and all supernumerary centriolar structures contained centrobin, a marker for procentrioles[128,285]. Since centrobin was not present at excess centriolar structures upon LGALS3BP knockdown alone, it could be concluded that PLK4 overexpression might compensate LGALS3BP depletion in these cells. Figure 28 describes a model of how the formation of supernumerary centriolar structures

depends on the expression of PLK4: the presence of PLK4 is necessary for the formation of supernumerary incomplete centriolar structures upon LGALS3BP knockdown since simultaneous PLK4 depletion reduces these aberrant structures and induces a shift towards one centriole per cell like PLK4 single knockdown does, too. Excess PLK4 expression, on the other hand, leads to an accumulation of procentrioles comprising all the respective markers. LGALS3BP depletion in a PLK4 overexpression background has no impact on procentriole accumulation and does not lead to additional incomplete substructures. Altogether, PLK4 expression levels might be crucial for either forming multiple centriolar structures or not and if they represent intact procentrioles or not. The LGALS3BP depletion phenotype only occurs at normal PLK4 levels whereas excess PLK4 levels overwrite this phenotype.

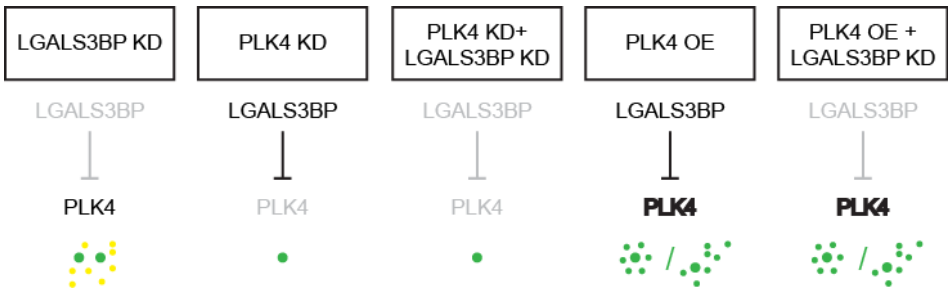

Figure 28: The formation of supernumerary centriolar structures depends on PLK4
The schematic illustrates the formation of supernumerary centriolar structures upon LGALS3BP-depletion depending on proper PLK4 expression. LGALS3BP knockdown in the background of normal PLK4 expression leads to multiple incomplete centriolar structures (displayed in yellow) additionally to normal centrioles (shown in green). Depletion of PLK4 results in a large fraction of cells containing at least one centriole, also in the background of LGALS3BP knockdown. Excess PLK4 levels evoke overduplication of centrioles thus leading to an accumulation of intact procentrioles (displayed by smaller green dots) in proximity to parental centrioles. This is also the case in the background of LGALS3BP-depletion suggesting that excess PLK4 levels overwrite the LGALS3BP-depletion phenotype. Depleted proteins are shown in grey. KD - knockdown, OE – overexpression

However, the question still remains why LGALS3BP single knockdown led to an accumulation of centriolar substructures and how PLK4 levels modulate their emergence. One possible explanation could be a structure-stabilizing role of LGALS3BP in centriole duplication. Interestingly, the supernumerary centriolar structures upon LGALS3BP depletion contained distal and central procentriolar markers (centrin2 and CPAP) as well as stabilized centriolar microtubules (acetylated and polyglutamylated tubulin) but lacked very proximal markers like PLK4, SAS6, CEP135 (localization of these markers shown in Figure 1b). It could therefore be that LGALS3BP depletion

leads to a fragmentation or breakup of distal procentrioles because LGALS3BP does not stabilize procentrioles anymore until they fully matured. It would thus be of interest to analyse CP110 localization to these structures since it is located to the very distal ends of centrioles[310]. However, centrobin, which localizes outside along the microtubule triplets of the daughter centrioles[285] and thus also to their distal parts, was not detected at these structures. Moreover, PLK4 overexpression in the background of LGALS3BP depletion resulted in amplification of intact procentrioles even though presumably stabilizing LGALS3BP was lacking.

Another explanation for the occurrence of multiple centriolar substructures could be an ectopic assembly of centriolar proteins upon LGALS3BP depletion. CPAP and its orthologues are known to bind tubulin dimers as well as microtubules[311–313] and are required for microtubule attachment to the initial procentriolar scaffold[314,315] as well as for centriole elongation[25,43]. It could therefore be that LGALS3BP depletion leads to an aberrant temporal and spatial acquisition of cytoplasmatic CPAP to centrosomes, which in turn binds tubulin dimers or microtubules and facilitates their stabilization e.g. via acetylation and polyglutamylation. These structures may also acquire centrin2 and other yet not detected centriolar proteins. Although these structures might be ectopically assembled upon LGALS3BP depletion, PLK4 could be able to induce normal procentriole formation in S phase of cell cycle. However, the LGALS3BP depletion phenotype depended on the presence of PLK4. It could therefore be that PLK4 induced procentriole assembly additionally at aberrant sites that were exposed due to LGALS3BP knockdown. These structures might be instable and thus lose certain early procentriolar marker proteins, e.g. PLK4, SAS6, CEP135 and centrobin, due to proteasomal degradation. Hence, it would be of interest to examine the marker composition of supernumerary centriolar structures in LGALS3BP-depleted cells after MG132 proteasome inhibitor treatment.

As overexpression of PLK4 leads to overduplication of procentrioles on multiple sites at the parental centrioles, the acquisition of more procentriolar proteins is necessary for the increased assembly rate[310,316]. A probable reason why supernumerary and incomplete centriole-like structures did not occur upon LGALS3BP depletion when PLK4 was overexpressed might be because these structures were recycled or assimilated into overduplicated procentrioles. The integration of preassembled

procentriolar complexes might be preferred rather than a consecutive assembly of procentrioles in this background. This hypothesis could be verified by live cell imaging of supernumerary centriole-like structures in LGALS3BP-depleted cells beginning at the time point when PLK4 overexpression is induced. Analysis of the spatial dynamics of the supernumerary centriolar structures might reveal whether they cluster to newly formed procentrioles or if they disappear. As centriolar substructures upon LGALS3BP depletion appeared malformed or incomplete, an incorporation of these structures into PLK4-dependently overduplicated procentrioles might also show structural defects[128]. An ultrastructural analysis of procentrioles by transmission electron microscopy in this experimental setup would therefore be instructive.

4.2.3 Synergistic effects of LGALS3BP and C-Nap1 on cell viability and proliferation

The examination of phenotypes resulting from simultaneous depletion of LGALS3BP and LGALS3BP-interacting proteins revealed no obvious effects regarding their ability to modulate the LGALS3BP single knockdown phenotype as judged by the presence of multiple centrin2-positive structures throughout all double knockdown experiments.
Interestingly, C-Nap1 as well as CEP55 single knockdown revealed frequently amplified centrin2 foci though their composition was distinct from that of LGALS3BP depletion with respect to the tested centriolar markers. However, a further validation and analysis of these phenotypes might provide additional molecular insight into centriolar duplication processes.
Simultaneous knockdown of LGALS3BP interactors and LGALS3BP, on the other hand, only led to additive phenotypes of the single knockdown experiments and did neither influence the occurrence of supernumerary centriolar structures nor the localization of CPAP and stabilized tubulins to them. Admittedly, double knockdown of LGALS3BP and C-Nap1 or CEP55 additionally led to occasionally amplified centrobin foci that, however, were not detected at all supernumerary centrin2-positive structures. All in all, it could be said that LGALS3BP-interacting proteins, at least those identified within this study, were not capable to modulate the LGALS3BP depletion phenotype. Anyhow, those results were not quantified but only qualitatively evaluated by eye and any

probable effect on the LGALS3BP phenotype as well as on the marker composition of excess centrin2-positive foci might be therefore missed. Secondly, it could not be assured that single cells examined were truly depleted for both targets in the double knockdown studies. The generation and investigation of a monoclonal knockdown cell line, which stably expresses LGALS3BP shRNA after induction, would consequently reduce the aforementioned limitation. Additionally, automated microscopy and image analysis represent powerful tools to perform large scale screenings for phenotypes. Both attempts were made in the present study. Unfortunately, the establishment of a stable LGALS3BP shRNA cell line failed because the clones lost their inducibility due to probable adaption and automated microscopy using the Cellomics™ pipeline was inappropriate for accurately detecting and counting the minute centriolar substructures upon LGALS3BP depletion. Probably, automated high resolution microscopy and image analysis on 3D samples would suit the given experimental requirements better[317].

Although the composition of supernumerary centrin2-positive structures was not affected, the double knockdown of LGALS3BP and C-Nap1 revealed a dramatic phenotype compared to the negative control and to the respective single knockdowns: mitotic cells were detected extremely rarely and a great fraction of cells was apoptotic. Incidentally, the apoptotic index of LGALS3BP and C-Nap1 single knockdown was also significantly elevated (≈ 3 % and ≈ 5 %) but not as extremely as in the double knockdown (≈ 11 %). Furthermore, quantitative densitometry on immunofluorescence micrographs of DAPI-stained DNA revealed significant decreases in G1 cell population as well as a prominent shift towards DNA contents greater than G2/M in double-depleted cells. Correspondingly, a portion of these cells appeared multinucleated or displayed huge, deformed or indented nuclei as opposed to the smoothly shaped nuclei of control cells. This outcome was also determined by an initial ImageJ analysis of nucleus shapes, which showed an increase in cell populations possessing lower values of form factor and roundness as well as larger nucleus areas. The irregular nucleus shapes might be explained by blebbing in the nuclear lamin meshwork, which is associated with a variety of pathologies like cancer but also with senescence[318–321]. The outcomes of nuclear shape description, however, have to be validated by biological replicates.

Hence, these findings suggest that LGALS3BP and C-Nap1 together are vital for cell proliferation and that a lack of both proteins induces apoptosis and alterations in the degree of ploidy, which might be due to cytokinesis or chromosome segregation errors. Besides disruption of the spindle assembly checkpoint (SAC) and mitotic slippage, cell fusion, DNA reduplication or cytokinesis failure for instance, centrosome abnormalities can cause aneuploidy[322–326]. Centrosome amplification can result in multipolar cell division leading to mitotic catastrophe or more than two aneuploid daughter cells that, however, are prone to die[108]. Importantly, cells can evade this by functional silencing or clustering of amplified centrosomes from multipolar spindles to form a bipolar spindle in mitosis[110,304,327–332]. The transient multipolar intermediate favours the formation of aberrant merotelic kinetochore-microtubule attachments before entering the bipolar stage[111,304,333]. Merotelic attachments can cause aneuploidy since they can escape the control of the SAC leading to chromosome missegregation events and abrogated cytokinesis due to lagging chromosomes[112,304]. A prolonged activity of the SAC as well as mitotic catastrophe might not be present in U2OS cells simultaneously depleted for LGALS3BP and C-Nap1 as a mitotic arrest, which is characteristic for both[29,108,322] was not detected by the analysis of cell cycle distribution and mitotic index determination.

However, there must be another explanation for the significant elevation of apoptotic indices in LGALS3BP and C-Nap1 single-depleted cells and the even greater increase in LGALS3BP and C-Nap1 double-depleted cells. Li *et al.* proposed an aneuploidy checkpoint after revealing that aneuploidy results in an increased formation of reactive oxygen species (ROS) in mouse embryonic fibroblasts (MEFs), which activates the ATM-p53 pathway leading to apoptosis in highly aneuploid cells[326,334]. As a consequence of ROS formation, ATM is activated either by oxidative DNA damage in a noncanonical way or directly[334–336]. Additionally, it has been revealed that the proliferation of aneuploid human cells is limited by a p53-dependent mechanism[337,338]. Furthermore, it has been shown that ROS decreases cell proliferation and induces premature senescence[339]. Since U2OS cells express wild type p53 as well as RB protein and are sensitive for p53-mediated growth arrest and apoptosis[340–342], the proposed model would work in this cell line.

Figure 29 explains how aneuploidy arising from centrosomal aberrations upon LGALS3BP and C-Nap1 double knockdown may lead to apoptosis and decreased proliferation in the aforementioned manner. According to Li *et al.*, slightly aneuploid cells with low p53 activation are genetically unfit and mildly aneuploid cells with medium p53 activation might enter p53-mediated cell cycle arrest or senescence[334]. As cells with nuclear shape irregularities were detected upon LGALS3BP/C-Nap1 double knockdown it could be assumed that these cells might be senescent since nuclear blebbing is characteristic for it[318,320,321]. Highly aneuploid cells, on the other hand, are not viable and are eliminated by p53-mediated apoptosis[334]. This fraction of cells might not be clearly definable by densitometric cell cycle analysis but rather by the increase of the apoptotic index.

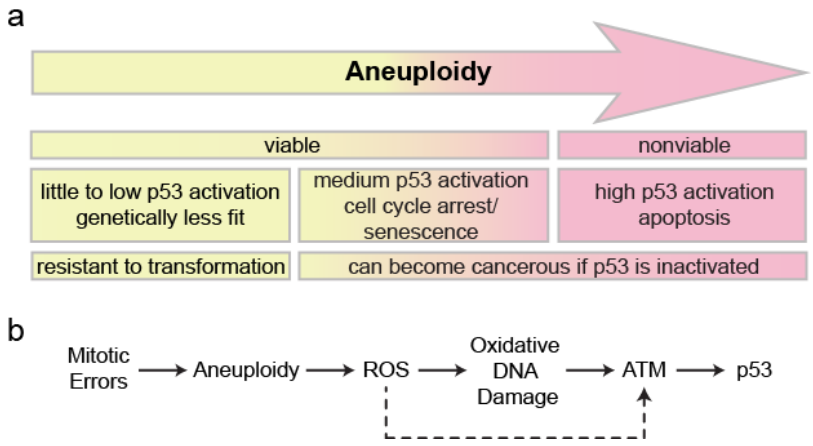

Figure 29: The outcome of aneuploidy
(a) Schematic representation of the cellular response to aneuploidy, which ranges from passive (unfitness) to active (activation of p53) depending on the grade of aneuploidy. **(b)** Proposal of an aneuploidy checkpoint. The dashed line indicates the possible direct activation of ATM by reactive oxygen species (ROS). Figure modified from Li *et al.*[334]

However, to verify this hypothesis, several follow-up studies have to be performed. Firstly, the effects of LGALS3BP and C-Nap1 double knockdown on cell cycle distribution have to be validated by fluorescence-activated cell sorting (FACS) and probable aneuploidies could be detected by fluorescence in situ hybridization (FISH). Secondly, it has to be investigated if merotelic kinetochore-microtubule attachments or cytokinesis failure are indeed the cause of aneuploidy in cells simultaneously depleted for LGALS3BP and C-Nap1. This could be addressed, for instance, by the analysis of immunolabelled kinetochores, by quantifying lagging chromosomes in

anaphase or via quantitative time-lapse microscopy in single cells. Thirdly, ROS levels as well as ATM and p53 activity have to be determined, e.g. by labelling ROS with a fluorescent dye and subsequent FACS analysis as well as examination of ATM and p53 activity via phospho-immunoblotting. It would be additionally of interest if the observations in double-depleted cells represent additive results of the single knockdowns or if they are uniquely the consequence of simultaneous loss of LGALS3BP and C-Nap1. Finally, it would be instructive to dissect in detail the pathway how p53 activation might lead to apoptosis in LGALS3BP/C-Nap1 double-depleted cells.

4.2.4 LGALS3BP – a phosphorylated protein?

LGALS3BP was further analysed concerning its ability to be phosphorylated since phosphorylation plays a crucial role for centrosome structures and function[40,49,52–54,92,284,287–293]. Additionally, it was of interest if phosphorylation appeared in a cell cycle-regulated manner.

To address this question, U2OS cells in mitosis and in interphase were analysed in the presence of phosphatase inhibitors as well as after incubation with calf-intestinal alkaline phosphatase (CIP). In addition to the usual LGALS3BP band, a ≈ 20 kDa higher molecular band at ≈ 100 kDa was detected by immunoblotting in the presence of phosphatase inhibitors, which appeared more prominently in interphase. To clarify if this band might be unspecific or represent phosphorylated fractions of LGALS3BP, cell lysates were dephosphorylated by CIP. For this purpose, however, different lysis buffers were used due to the requirements for CIP activity. This might be a reason why it was difficult to claim whether the band at ≈ 100 kDa weakened due to dephosphorylation or just because LGALS3BP protein levels appeared weaker in general in this approach. Another explanation could be that a large portion of LGALS3BP was slightly phosphorylated so that phosphorylation did not lead to a drastic shift towards higher molecular weights detectable in 10 % polyacrylamide gels. The band at ≈ 100 kDa might thus be unspecific and the weakened band at ≈ 80 kDa may result from dephosphorylation by CIP. Gels with lower amounts of acrylamide would better separate proteins at 80 kDa and may unveil shifts towards slightly higher

molecular weights due to minor phosphorylation. More accurately, mass spectrometry analysis could be performed on this.

The probable phosphorylation of LGALS3BP was further analysed by *in vitro* studies. Three predicted phosphorylation sites, T220, S256 and S444, were profiled by Kinexus against AKT1, CaMK4, CHK1, CHK2, CK1d and PLK1 kinases via radiometry. For this purpose, peptides containing the predicted wild type phosphorylation site were synthesized as well as phospho-mutant peptides, in which the respective serine or threonine was replaced by a non-phosphorylatable alanine.

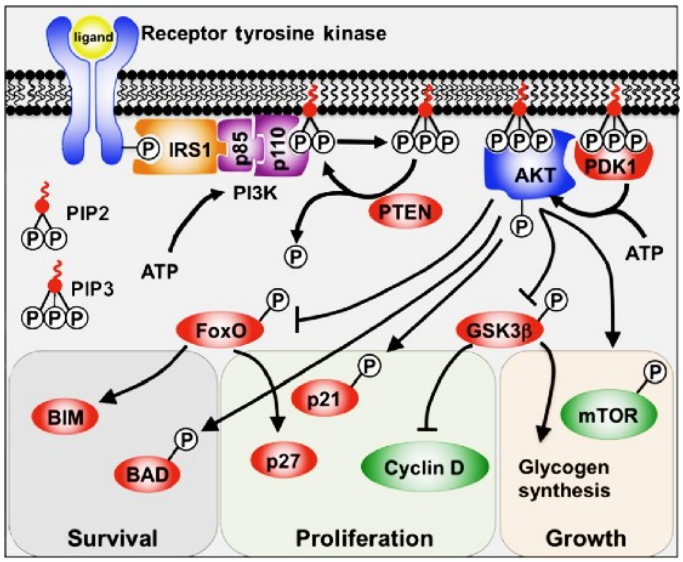

Figure 30: The PI3K/AKT signalling pathway
Ligand-binding to the receptor tyrosine kinase leads its auto-phosphorylation and to the acquisition of substrate proteins (e.g. IRS1) that recruit the regulatory (p85) and catalytic (p110) subunit of PI3K. PI3K phosphorylates PIP2 to PIP3, which acts as a secondary messenger within the inner surface of the cell membrane. AKT as well as PDK1 bind to PIP3 and PDK1 activates AKT by phosphorylation. Active AKT promotes cell survival, proliferation and growth by phosphorylation of key substrates. Figure adapted from McGonnell *et al.*[343]

The wild type T220 peptide was strongly phosphorylated by AKT1 (84 % compared to phospho-mutant). AKT1, one of three isoforms of the AKT/PKB family, is a proto-oncogene as its activation is associated with cell survival[344–346], growth[347], proliferation[348–352], migration and invasion[353–355]. Figure 30 briefly explains the phosphoinositide 3-kinase (PI3K)/AKT signalling pathway, which is activated via the receptor tyrosine kinase class of receptors. Interestingly, increased PI3K/AKT signalling additionally induces centrosome amplification and chromosomal instability[294,356–363]. Although AKT has not been found to localize to centrosomes, it may phosphorylate cytoplasmatic LGALS3BP *in vivo* and thereby regulating centrosomal localization of LGALS3BP and centrosome integrity as it has been recently shown for TEIF, which also colocalizes with C-Nap1[364]. As T220 is located within the BTB/POZ domain of LGALS3BP, phosphorylation by AKT might thus function in LGALS3BP dimerization[121,127]. Either by promoting or by interfering with LGALS3BP dimerization,

AKT phosphorylation could lead to LGALS3BP dissociation from centrosomes and thereby causing accumulation of aberrant centriolar structures.

The wild type S256 peptide only showed weak phosphorylation by CHK1 (37 %) compared to the phospho-mutant peptide. The S444 wild type peptide, however, was strongly phosphorylated by CHK1 and CHK2 (84 % and 98 %) and moderately by CaMK4 (59 %). Unlike CaMK2, no centrosomal function or localization has been reported for CaMK4 so far[365–367]. CaMK4 is activated by Ca^{2+}/calmodulin (Ca^{2+}/CaM) and Ca^{2+}/CaM-dependent kinase kinases (CaMKK) to induce transcription by phosphorylating transcription factors like CREB, for instance[368,369]. In its inactive form, CaMK4 is bound to the serine/threonine-protein phosphatase 2A (PP2A)[368,369]. As PP2A was identified at interphase centrosomes in human cells via mass spectrometry-based proteomic analysis[3], CaMK4 might be present in its inactive form at centrosomes bound to PP2A. Ca^{2+} signalling pathways are partially integrated at centrosomes and are thereby involved in cell cycle progression, proliferation as well as in centrosome duplication and integrity[367,370–373]. Hence, centrosomal Ca^{2+} levels may result in Ca^{2+}/CaM-dependent dissociation of PP2A and thereby leading to activation of CaMK4[368]. Active CaMK4 could be able to phosphorylate LGALS3BP at centrosomes prior to its nuclear relocation to support transcription. This model, however, is very hypothetical since CaMK4 was not shown to localize to centrosomes or to act in centrosome-related cellular functions yet.

CHK1 and CHK2 phosphorylation of the S256 and S444 wild type peptides suggests that LGALS3BP might be targeted by DNA damage checkpoints. Importantly, several DNA damage checkpoint proteins, such as ATM, ATR, CHK1, CHK2 and p53 for instance, localize to centrosomes[90–92]. Furthermore, it is known that DNA damage induces centrosome amplification[374–385]. Upon DNA damage, LGALS3BP phosphorylation by CHK1/2 may lead to its dissociation from centrosomes thereby causing centrosomal aberrations contributing to cell cycle arrest or apoptosis. This might be contingently important for the S256 phosphorylation site as it is located within the IVR domain of LGALS3BP, which mediates protein-protein interactions and which was unveiled by our group to be responsible for excess PCM acquisition upon LGALS3BP overexpression[127,128]. At least theoretically, S444 phosphorylation within the yet uncharacterized linker region of LGALS3BP could contribute to this, which would have

to be tested in future studies. Cell cycle arrest might be mediated by other CHK1/2 targets as it was not detected upon LGALS3BP depletion alone[128]. However, the apoptosis rate significantly increased following LGALS3BP knockdown.

In the absence of DNA damage, CHK1 is also involved in preventing premature mitotic entry and CHK2 is suggested to play a role in bipolar spindle formation, in proper mitotic progression and in maintaining chromosomal stability[69,295,386]. As CHK1 is localized to interphase and CHK2 to mitotic centrosomes, phosphorylation by these kinases might regulate cell cycle-dependent LGALS3BP localization to centrosomes[70,295,386–388]. CHK1 phosphorylation could stabilize LGALS3BP at centrosomes in interphase or CHK2 phosphorylation may lead to LGALS3BP dissociation in mitosis.

Nevertheless, the proposed LGALS3BP phosphorylation sites would have to be further validated by mass spectrometry, functionally characterized *in vitro* and *in vivo* with full length LGALS3BP phospho-mutant constructs to define if and into which of the aforementioned signalling pathways they can be integrated or not.

4.2.5 LGALS3BP deregulation and centrosome aberrations in cancer

Centrosome aberrations occur commonly in cancer and are linked to aneuploidy as well as chromosomal instability[16,94,95,104–106,389,390]. Furthermore, LGALS3BP is deregulated in a plethora of tumours and proposed as a potent tumour marker[141,143,146,147,391–400]. This, together with the centrosomal phenotypes observed upon exogenously induced LGALS3BP deregulation in the present study, demanded for the examination of centrosomes in cancer cells with endogenously deregulated levels of LGALS3BP.

The analysis of the *TMPRSS2:ERG* gene fusion-negative prostate cancer cell lines DU-145, LNCaP and PC-3 revealed decreased LGALS3BP expression when compared to the normal prostate epithelial cell line RWPE-1. Interestingly, these cells showed supernumerary centrin2-positive structures, similar to the LGALS3BP depletion phenotype detected in U2OS cells, which were not present in RWPE-1 control cells. Furthermore, the *TMPRSS2:ERG* fusion-positive prostate cancer cell line VCaP, which endogenously overexpresses LGALS3BP, exhibited hypertrophic PCM as given by

enlarged PCM areas. This might suggest a correlation between LGALS3BP expression and centrosome aberrations in prostate cancer cells. However, a direct impact of LGALS3BP deregulation on the occurrence of centrosome aberrations in the examined prostate cancer cell lines cannot be concluded from these data because a deregulation of other pathways leading to this cannot be excluded. Rescue experiments in these cell lines might elucidate a dependency of centrosomal integrity on LGALS3BP expression to this end. Furthermore, it would be interesting to clarify if LGALS3BP upregulation in prostate cancer directly correlates with ERG overexpression caused by *TMPRSS2:ERG* gene fusion and if LGALS3BP expression might be even directly regulated by ERG. If a correlation principally exists, LGALS3BP serum level measurements might be a convenient way to detect the *TMPRSS2:ERG* gene fusion state in prostate cancer patients. Supportingly, LGALS3BP levels, centrosome hypertrophies as well as CINs increase upon prostate cancer progression, and the *TMPRSS2:ERG* gene fusion is a valid progression marker of the disease as well as an indication of poor survival prognosis[95,389,392,401,402].

Centrosomal aberrations together with LGALS3BP deregulation were also detected in the examined breast cancer cell line SK-BR-3 and in seminoma tissue.

Patients' seminoma tissue with downregulated LGALS3BP expression compared to testis control tissue exhibited centriolar amplifications *in situ* that resembled the exogenous LGALS3BP depletion phenotype in U2OS cells[128]. Importantly, the endogenously LGALS3BP overexpressing breast cancer cell line SK-BR-3 showed hypertrophic PCM, which could be reverted by LGALS3BP depletion in these cells. This rescue was validated by biological replicates and by quantification of different PCM markers. Taken together, this evidence strongly suggests that LGALS3BP deregulation might indeed contribute to centrosome abnormalities at least in those cancer cells.

In conclusion, it would be of great interest to examine if centrosome aberrations in other cancer backgrounds are caused by LGALS3BP deregulation. Targeting LGALS3BP expression by drug treatment would then be a possibility to interfere with cancer progression.

4.3 Transcriptional regulation of LGALS3BP

The collaboration with Prof. Dr. Dr. med. Michal-Ruth Schweiger's group resulted in substantial outcomes on how LGALS3BP expression might be regulated.

Specifically, basal expression of LGALS3BP as well as its response to INFγ stimulation depended on the presence of the transcriptional regulator BRD4. Furthermore, methylation events mediated by the polycomb group protein EZH2 were found to silence *LGALS3BP* gene expression in *TMPRSS2:ERG* gene fusion-negative prostate cancer cells.

4.3.1 The transcriptional regulator BRD4 is required for LGALS3BP expression

According to Andrea Wunderlich's studies on the bromodomain-containing protein 4 (BRD4), *LGALS3BP* as well as signal transducers and activators of transcription (*STAT*s) were some of the top downregulated genes upon BRD4 depletion in HEK293T cells as revealed by mRNA sequencing analysis[296]. Moreover, a pathway analysis (IPA) on this data uncovered interferon signalling as the most significantly affected one[296]. As *LGALS3BP* represents an INFγ-stimulated gene[161,163], STAT1 was included into the further analysis because it mediates the cellular INFγ response as a phosphorylated homodimer[297,298].

The outcome of this work showed a significant downregulation of *STAT1* and *LGALS3BP* promoter activities, mRNA and protein levels, respectively, upon BRD4 depletion in HEK293T cells. INFγ stimulation, on the other hand, revealed increased *LGALS3BP* promoter activities and protein levels in the presence of both BRD4 isoforms as well as in the absence of the long BRD4 isoform caused by shE1 transfection. In cells lacking both BRD4 isoforms (shC2), *LGALS3BP* promoter activities, mRNA and protein levels were prominently downregulated upon INFγ-stimulation. Furthermore, INFγ upregulated STAT1 protein levels although *STAT1* mRNA expression remained unaffected. This suggests that INFγ might not induce *STAT1* mRNA expression but rather leads to stabilization of the STAT1 protein. However, an upregulation of *STAT1* gene expression upon INFγ-treatment has been previously shown[403,404]. STAT1 protein levels were depleted upon shC2- and shE1-mediated BRD4 knockdown in

INFγ-stimulated cells. Certainly, *STAT1* mRNA levels were upregulated in INFγ-stimulated and shE1-depleted cells. However, this disagreed with the depleted STAT1 protein levels. The discussion will therefore further focus on the expression of STAT1 protein as it exerts its cellular function. Taken together, these findings suggest that BRD4 regulates STAT1 as well as LGALS3BP expression independently. This goes along with the recent finding that BRD4 regulates transcription of interferon-stimulated genes[405].

Recently, BRD4 was also found associated with acetylated nucleosomes within the *LGALS3BP* promoter in HEK293 cells[406]. Furthermore, BRD4 is able to target promoters over SP1 transcription factor binding sites[407]. Importantly, the *LGALS3BP* promoter contains several proposed regulatory elements: besides a GAS, an ISRE and two NFκB binding sites, for instance, it features several SP1 binding sites[158]. Together, this indicates that BRD4 is able to target the *LGALS3BP* promoter and might even regulate *LGALS3BP* transcription. BRD4-association to DNA via SP1 might induce basal expression of *LGALS3BP* mRNA as BRD4 knockdown results in LGALS3BP depletion (Figure 31).

Upon INFγ stimulation, BRD4 might recruit INFγ-specific transcription factors that enhance *LGALS3BP* expression. Such as the phosphorylated STAT1 homodimer, which binds to GAS elements of DNA and thereby acts as a transcription factor in response to INFγ stimulation[408–411]. Furthermore, STAT1 was found to be acetylated depending on the balance between STAT1-associated histone deacetylases (HDACs) and histone acetyltransferases (HATs)[412]. This is of particular interest here as BRD4 binds to acetylated proteins via its bromodomains[413]. STAT1 activation upon INFγ stimulation might therefore lead to a BRD4-STAT1 complex formation that may enhance *LGALS3BP* expression (Figure 31).

Following shC2-mediated knockdown of both BRD4 isoforms, *STAT1* and *LGALS3BP* expression is downregulated in unstimulated as well as in INFγ-stimulated conditions as the transcriptional regulation by BRD4 is missing.

Upon shE1 transfection, the short isoform of BRD4 remains expressed and may bind to acetylated histones within the *LGALS3BP* promoter. However, this isoform may lack SP1 binding capabilities, for instance. The short BRD4 isoform might thus not properly align to the *LGALS3BP* promoter, which inhibits the start of transcriptional elongation

by RNA polymerase II (RNA Pol II) mediated by the recruitment and activation of the positive transcription elongation factor b (pTEFb)[188–193]. Besides STAT1, INFγ stimulation also activates other STAT1-independent transcription factors that function in parallel[411]. NFκB, for instance, is activated via INFγ in a STAT1-independent way[414–416]. Interestingly, LGALS3BP possesses two NFκB binding sites within its promoter region, and BRD4 is able to interact with the acetylated RelA (p65) subunit of NFκB to promote transcriptional activation[158,417]. Furthermore, NFκB was shown to induce *LGALS3BP* expression[164]. Together, this might explain elevated *LGALS3BP* expression in the absence of STAT1 that was detected in shE1-transfected and INFγ-stimulated cells: NFκB binding to the remaining short isoform of BRD4 as well as to the *LGALS3BP* promoter might facilitate the proper alignment of this complex to induce pTEFb-mediated RNA Pol II phosphorylation, which initiates transcriptional elongation (Figure 31).

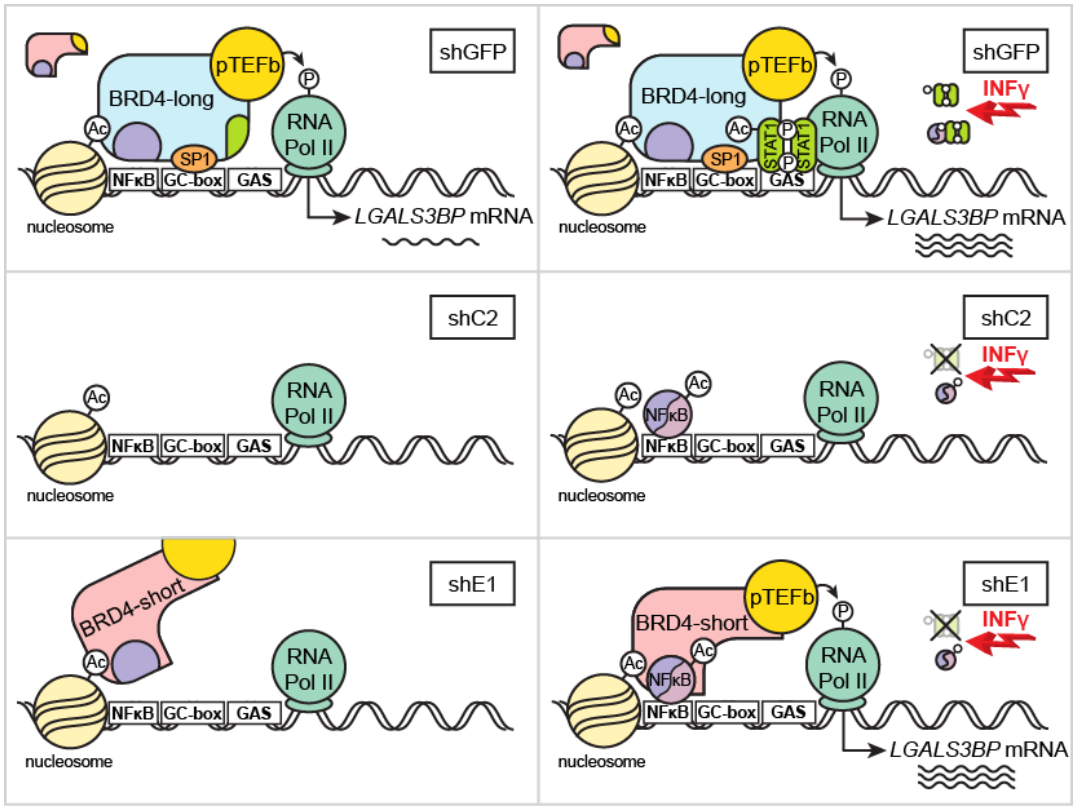

Figure 31: Model on how BRD4 may regulate *LGALS3BP* expression
Schematic illustration of *LGALS3BP* expression regulation upon isoform-specific BRD4 knockdown in unstimulated (left column) and INFγ-stimulated conditions (right column). Both BRD4 isoforms are depleted upon shC2 transfection while the short BRD4 isoform persists upon shE1 transfection. ShGFP diplays a non-targeting control. Detailed information on the transcriptional regulation of LGALS3BP is given in the main text.

In fact, the proposed model suggests that NFκB functions as a backup of STAT1 in INFγ-induced *LGALS3BP* expression. This might be supported by the finding that acetylated STAT1 interacts with the RelA (p65) subunit of NFκB, which decreases NFκB DNA binding and target gene expression (Figure 31)[412]. However, if STAT1 is not expressed, NFκB might drive INFγ-stimulated *LGALS3BP* transcription (Figure 31).

To support the aforementioned model on BRD4-mediated transcriptional regulation of *LGALS3BP* expression, additional experiments are definitively needed. It should be investigated if the short isoform of BRD4 interacts with NFκB and if NFκB associates with the *LGALS3BP* promoter, respectively upon depletion of the long BRD4 isoform with simultaneous INFγ stimulation. Furthermore, it would be of interest to unveil the proposed SP1 protein binding domain within the long BRD4 isoform and if the short BRD4 isoform might be able to bind SP1. This could be performed by immunoprecipitation approaches on the short BRD4 isoform as well as on domain or deletion constructs of the long variant, for instance. A specific SP1 binding site might be harboured by the C-terminus of the long BRD4 isoform that is absent in the short one. Regarding the short BRD4 isoform, this might then be an explanation for a deficiency in DNA binding via SP1 motifs. Moreover, STAT1 dimer interaction with BRD4 should be examined upon INFγ stimulation and if STAT1 acetylation might be necessary to that end.

As a conclusion, BRD4 plays a crucial role in regulating *LGALS3BP* gene expression as well as in mediating its response to INFγ exposure.

4.3.2 LGALS3BP expression is regulated through promoter methylation

Börno *et al*. discovered significantly higher global methylation patterns correlating with a prominent upregulation of histone methyltransferase *EZH2* expression in *TMPRSS2:ERG* gene fusion-negative prostate cancer tissues when compared to control tissue[243]. The outcome of significantly decreased *LGALS3BP* expression together with enhanced CpG methylation within the *LGALS3BP* promoter in *TMPRSS2:ERG* fusion-negative prostate cancer tissue asked for a dependency of *LGALS3BP* expression on EZH2. Elevated *EZH2* expression and *LGALS3BP* promoter methylation was also detected in fusion-positive prostate cancer samples. However, this outcome was

significant but not as prominent as detected in fusion-negative samples when compared to control tissue. An increased *EZH2* expression in *TMPRSS2:ERG* fusion-positive prostate cancer is caused by ERG overexpression as ERG directly targets the *EZH2* promoter[418]. EZH2 overexpression in *ERG* fusion-negative prostate cancer, on the other hand, is a result of DNA methylation-mediated silencing of the *EZH2* negative regulator *miR26a*[243]. Here, it should be noticed again that EZH2 is able to repress gene expression via binding and activating DNA methyltransferases (DNMTs) additionally to its histone methyltransferase activity[201,230]. To answer the question of EZH2-mediated *LGALS3BP* silencing, the *TMPRSS2:ERG* fusion-negative prostate cancer cell line PC-3 was investigated as it shows simultaneous *EZH2* upregulation and *LGALS3BP* downregulation[243]. EZH2 knockdown in these cells revealed a significant increase of *LGALS3BP* gene expression and LGALS3BP protein levels as compared to control cells. This outcome was further validated by *miR26a* mimics transfection.

It could be assumed that the loss of EZH2-mediated gene silencing might lead to re-expression of positive LGALS3BP regulators. If so, this would indicate an indirect regulation of *LGALS3BP* expression by EZH2. However, this would not explain the enhanced methylation detected within the *LGALS3BP* promoter.

It was quite surprising to detect DNA methylation-mediated silencing of the *LGALS3BP* promoter as it is not particularly GC-rich and does not contain CpG islands[158]. However, the prostate cancer MeDIP-Seq data set of Börno *et al*. clearly revealed differential methylation at CpGs within the *LGALS3BP* promoter as redundant reads and reads with no CpGs were excluded from further analysis[243]. In support of these findings, DNA methylation at CpG-poor promoters without CpG islands was shown to directly silence the respective gene expression[222].

Therefore, these results collectively suggest that *LGALS3BP* gene expression is silenced by EZH2-mediated promoter methylation in *TMPRSS2:ERG* fusion-negative prostate cancer.

4.4 Conclusions and perspectives

This study focussed on the molecular and functional characterization of LGALS3BP in cancer and centrosome biology. Thereby, several approaches validated the presence of

LGALS3BP at centrosomes and its localization to the proximal part of centrioles in detail. So far, only extracellular functions of LGALS3BP have been reported. The present study, however, provides striking evidence that LGALS3BP is further involved in the maintenance of centrosome integrity: LGALS3BP causes centrosome hypertrophy when upregulated and the accumulation of defective centriolar structures when depleted. Supportingly, LGALS3BP deregulation correlated with centrosome abnormalities detected in prostate cancer and breast cancer cell lines as well as in seminoma tissue[128]. Importantly, two rescue experiments revealed a reversion of these phenotypes towards control cells upon restoration of normal LGALS3BP levels. Furthermore, the presence of C-Nap1 together with LGALS3BP was found to be crucial for cell proliferation and viability as simultaneous loss of these proteins caused aneuploidy and apoptosis.

Together, these findings asked for mechanisms that control LGALS3BP expression as it is commonly deregulated in cancer and centrosomal aberrations contribute to genetic instability, a hallmark of cancer[16,94,95,104–106,141,143,146,147,389–400].

The present study revealed the long BRD4 isoform as a positive regulator of basal *LGALS3BP* gene expression and as a mediator of INFγ-induced LGALS3BP upregulation. Interestingly, the short isoform of BRD4 was still able to mediate LGALS3BP upregulation as a response to INFγ stimulation although it failed to regulate basal LGALS3BP expression in unstimulated conditions. This outcome indicates different functions of the two BRD4 isoforms in regulating *LGALS3BP* expression. The maintenance of the short BRD4 isoform might therefore be of interest in disease if treating elevated LGALS3BP levels with keeping its response to INFγ stimulation is demanded. Regarding the proposed model on BRD4-regulated *LGALS3BP* expression (Figure 31), small molecule-mediated inhibition of the SP1 binding site within the long BRD4 isoform might constitute a situation similar to that observed upon shE1 transfection. Inhibition of the SP1 binding site would only target the long isoform of BRD4 while the short isoform may still act in the INFγ response of *LGALS3BP* expression via NFκB. However, no inhibitor targeting this specific binding site of BRD4 has been developed so far because this interaction has not been characterized yet. Otherwise, treatment with the well-established BET inhibitors JQ1 or I-BET, for instance, which block the bromodomains of BRD4 to inhibit acetyl-lysine binding, will

target both isoforms of BRD4[419–421]. This would lead to depletion of LGALS3BP and insensitivity to INFγ stimulation as it is detected upon shC2 transfection (Figure 31).

The outcome of *LGALS3BP* promoter silencing via EZH2-mediated DNA methylation in *TMPRSS2:ERG* fusion-negative prostate cancer displayed another path to regulate *LGALS3BP* expression. This study further revealed high EZH2 expression accompanied by LGALS3BP downregulation and centriolar amplifications in *TMPRSS2:ERG* fusion-negative prostate cancer cells. Supportingly, breast cancer tumours with endogenously upregulated EZH2 levels exhibited amplifications of centrosomal structures[203]. Moreover, EZH2 upregulation in patients' cancer tissue was found to correlate with high tumour grade, aggressiveness and genomic instability[203,204]. The recent finding that EZH2 epigenetically represses interferon γ receptor 1 (*INFGR1*) expression together with the present finding of EZH2-mediated silencing of INFγ-inducible *LGALS3BP* indicates that EZH2 might be involved in global repression of the cellular INFγ response or even of the immune system as a whole[422]. At least in MYC-driven prostate cancer, drug-mediated inhibition of EZH2 with simultaneous INFγ treatment led to remarkable anti-tumour effects[422]. Furthermore, drug-mediated inhibition of EZH2 was shown to block tumour growth and to increase chemotherapeutic sensitivity in certain cancer types[209–211]. Together, this suggests that also EZH2-mediated downregulation of LGALS3BP might contribute to cancer aggressiveness probably via affecting centrosome integrity.

The identification of potential kinases targeting LGALS3BP by *in vitro* kinase profiling on LGALS3BP peptides might establish LGALS3BP-targeting by certain signalling pathways. Hence, CHK1/2-mediated phosphorylation may integrate LGALS3BP into DNA damage checkpoints or unperturbed G2/M cell cycle transition. Furthermore, AKT-mediated phosphorylation of LGALS3BP could contribute to AKT signalling-implicated cellular roles in cell proliferation, growth, migration and survival, for instance, in which centrosomes are involved as well[354,363]. LGALS3BP-targeting by CaMK4 may further link Ca^{2+} signalling pathways to centrosomes and might contribute to its recently discovered function in the negative regulation of cell proliferation[423]. Hence, LGALS3BP phosphorylation by the proposed kinases should be validated *in vivo* by future experiments and the centrosomal association of the presented signalling pathways via LGALS3BP should be tested.

Figure 32 summarizes the outcome of this study and presents a graphic model on the centrosomal phenotypes provoked by LGALS3BP deregulation as well as on how LGALS3BP is transcriptionally or post-translationally targeted.

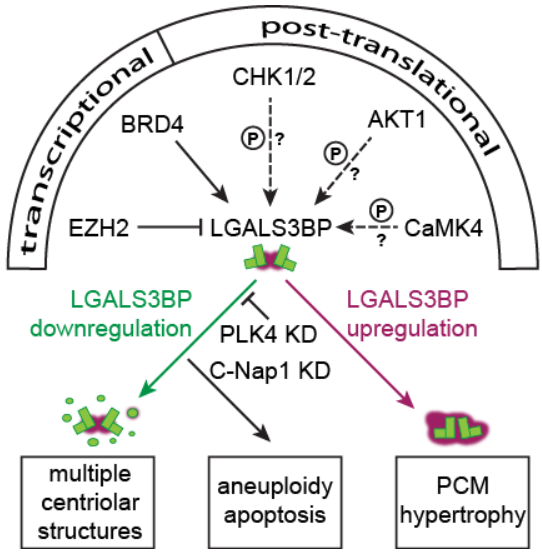

Figure 32: Schematic integration of the outcomes of this study
LGALS3BP gene expression is negatively regulated by EZH2-mediated promoter methylation while BRD4 promotes *LGALS3BP* basal expression as well as its INFγ induction by acting as a transcription co-factor. The LGALS3BP protein might be further modified post-translationally by CHK1/2, AKT1 and CaMK4 kinases. Upregulation of LGALS3BP leads to hypertrophic centrosomes as given by enlarged PCM areas. Downregulation of LGALS3BP, however, gives rise to multiple incomplete centriolar structures that are abrogated by PLK4 co-depletion. Moreover, simultaneous depletion of LGALS3BP and its interaction partner C-Nap1 resulted in decreased cell proliferation, aneuploidy and apoptosis.

The gained knowledge about LGALS3BP regulation provided by this study but also by others[137,161,164,167,424–426] might consequently allow a reversion of centrosomal aberrations caused by LGALS3BP deregulation. Relating to the transcriptional regulators of *LGALS3BP* gene expression presented by this study, several small molecule inhibitors have already been developed that target BRD4, NFκB, EZH2 and DNMTs, for instance[209–211,419–422,427–432]. But also the proposed post-translational modification via phosphorylation of LGALS3BP by CHK1/2, AKT1 and CaMK4 kinases can be inhibited by specific drugs[433–439]. Restoration of contextually normal LGALS3BP expression in cancer with LGALS3BP deregulation or targeting LGALS3BP phosphorylation might therefore antagonize cancer progression. Hence, future experiments on cellular cancer models targeting the aforementioned kinases and transcriptional regulators with the respective drugs should focus on LGALS3BP and centrosome aberrations as well to explain possible outcomes relating to proliferation, aneuploidy, apoptosis or centrosome-associated signalling pathways.

In conclusion, the presented study provides a substantial functional characterization of centrosome-associated LGALS3BP and new insights into its transcriptional regulation as well as a comprehensive set of information for prospective research to be based on.

5. References

1. Scheer, U. Historical roots of centrosome research: discovery of Boveri's microscope slides in Würzburg. *Philos. Trans. R. Soc. Lond. B. Biol. Sci.* **369,** 20130469– (2014).
2. Paintrand, M., Moudjou, M., Delacroix, H., *et al.* Centrosome organization and centriole architecture: Their sensitivity to divalent cations. *J. Struct. Biol.* **108,** 107–128 (1992).
3. Andersen, J., Wilkinson, C. & Mayor, T. Proteomic characterization of the human centrosome by protein correlation profiling. *Nature* **426,** 570–574 (2003).
4. Jakobsen, L., Vanselow, K., Skogs, M., *et al.* Novel asymmetrically localizing components of human centrosomes identified by complementary proteomics methods. *EMBO J.* **30,** 1520–1535 (2011).
5. Alves-Cruzeiro, J. M. D. C., Nogales-Cadenas, R. & Pascual-Montano, A. D. CentrosomeDB: a new generation of the centrosomal proteins database for Human and Drosophila melanogaster. *Nucleic Acids Res.* **42,** D430–6 (2014).
6. Edde, B., Rossier, J., Le Caer, J., *et al.* Posttranslational glutamylation of alpha-tubulin. *Science (80-.).* **247,** 83–85 (1990).
7. Piperno, G. Monoclonal antibodies specific for an acetylated form of alpha-tubulin recognize the antigen in cilia and flagella from a variety of organisms. *J. Cell Biol.* **101,** 2085–2094 (1985).
8. Kodani, A., Salomé Sirerol-Piquer, M., Seol, A., *et al.* Kif3a interacts with Dynactin subunit p150Glued to organize centriole subdistal appendages. *EMBO J.* **32,** 597–607 (2013).
9. Tanos, B. E., Yang, H.-J., Soni, R., *et al.* Centriole distal appendages promote membrane docking, leading to cilia initiation. *Genes Dev.* **27,** 163–168 (2013).
10. Nigg, E. a. & Stearns, T. The centrosome cycle: Centriole biogenesis, duplication and inherent asymmetries. *Nat. Cell Biol.* **13,** 1154–1160 (2011).
11. Lawo, S., Hasegan, M., Gupta, G. D., *et al.* Subdiffraction imaging of centrosomes reveals higher-order organizational features of pericentriolar material. *Nat. Cell Biol.* **14,** 1148–1158 (2012).
12. Sonnen, K. F., Schermelleh, L., Leonhardt, H., *et al.* 3D-structured illumination microscopy provides novel insight into architecture of human centrosomes. *Biol. Open* **1,** 965–976 (2012).
13. Mennella, V., Keszthelyi, B., McDonald, K. L., *et al.* Subdiffraction-resolution fluorescence microscopy reveals a domain of the centrosome critical for pericentriolar material organization. *Nat. Cell Biol.* **14,** 1159–1168 (2012).
14. Mennella, V., Agard, D. A., Huang, B., *et al.* Amorphous no more: subdiffraction view of the pericentriolar material architecture. *Trends Cell Biol.* **24,** 188–197 (2014).
15. Kollman, J. M., Merdes, A., Mourey, L., *et al.* Microtubule nucleation by γ-tubulin complexes. *Nat. Rev. Mol. Cell Biol.* **12,** 709–721 (2011).
16. Pihan, G. a. Centrosome Dysfunction Contributes to Chromosome Instability, Chromoanagenesis, and Genome Reprograming in Cancer. *Front. Oncol.* **3,** 1–26 (2013).
17. DePamphilis, M. L., Blow, J. J., Ghosh, S., *et al.* Regulating the licensing of DNA replication origins in metazoa. *Curr. Opin. Cell Biol.* **18,** 231–239 (2006).
18. Tsou, M.-F. B. & Stearns, T. Controlling centrosome number: licenses and blocks. *Curr. Opin. Cell Biol.* **18,** 74–78 (2006).
19. Lacey, K. R., Jackson, P. K. & Stearns, T. Cyclin-dependent kinase control of centrosome duplication. *Proc. Natl. Acad. Sci.* **96,** 2817–2822 (1999).
20. Meraldi, P., Lukas, J., Fry, A. M., *et al.* Centrosome duplication in mammalian somatic cells requires E2F and Cdk2-cyclin A. *Nat. Cell Biol.* **1,** 88–93 (1999).
21. Matsumoto, Y., Hayashi, K. & Nishida, E. Cyclin-dependent kinase 2 (Cdk2) is required for centrosome duplication in mammalian cells. *Curr. Biol.* **9,** 429–432 (1999).
22. Hinchcliffe, E. H. Requirement of Cdk2-Cyclin E Activity for Repeated Centrosome

Reproduction in Xenopus Egg Extracts. *Science (80-.).* **283,** 851–854 (1999).

23. Arquint, C., Sonnen, K. F., Stierhof, Y.-D., *et al.* Cell-cycle-regulated expression of STIL controls centriole number in human cells. *J. Cell Sci.* **125,** 1342–1352 (2012).

24. Strnad, P., Leidel, S., Vinogradova, T., *et al.* Regulated HsSAS-6 Levels Ensure Formation of a Single Procentriole per Centriole during the Centrosome Duplication Cycle. *Dev. Cell* **13,** 203–213 (2007).

25. Tang, C.-J. C., Fu, R.-H., Wu, K.-S., *et al.* CPAP is a cell-cycle regulated protein that controls centriole length. *Nat. Cell Biol.* **11,** 825–831 (2009).

26. Seki, A., Coppinger, J. a, Jang, C.-Y., *et al.* Bora and the Kinase Aurora A Cooperatively Activate the Kinase Plk1 and Control Mitotic Entry. *Science (80-.).* **320,** 1655–1658 (2008).

27. Macůrek, L., Lindqvist, A., Lim, D., *et al.* Polo-like kinase-1 is activated by aurora A to promote checkpoint recovery. *Nature* **455,** 119–123 (2008).

28. Fry, A. M. Solving the centriole disengagement puzzle. *Nat. Cell Biol.* **17,** 3–5 (2015).

29. Musacchio, A. & Salmon, E. D. The spindle-assembly checkpoint in space and time. *Nat. Rev. Mol. Cell Biol.* **8,** 379–93 (2007).

30. Graser, S., Stierhof, Y.-D. & Nigg, E. a. Cep68 and Cep215 (Cdk5rap2) are required for centrosome cohesion. *J. Cell Sci.* **120,** 4321–4331 (2007).

31. Bahe, S., Stierhof, Y. D., Wilkinson, C. J., *et al.* Rootletin forms centriole-associated filaments and functions in centrosome cohesion. *J. Cell Biol.* **171,** 27–33 (2005).

32. Gönczy, P. Centrosomes and cancer: revisiting a long-standing relationship. *Nat. Rev. Cancer* **15,** 639–652 (2015).

33. Sir, J.-H., Barr, A. R., Nicholas, A. K., *et al.* A primary microcephaly protein complex forms a ring around parental centrioles. *Nat. Genet.* **43,** 1147–1153 (2011).

34. Brown, N. J., Marjanović, M., Lüders, J., *et al.* Cep63 and Cep152 Cooperate to Ensure Centriole Duplication. *PLoS One* **8,** e69986 (2013).

35. Lukinavičius, G., Lavogina, D., Orpinell, M., *et al.* Selective Chemical Crosslinking Reveals a Cep57-Cep63-Cep152 Centrosomal Complex. *Curr. Biol.* **23,** 265–270 (2013).

36. Sonnen, K. F., Gabryjonczyk, A.-M., Anselm, E., *et al.* Human Cep192 and Cep152 cooperate in Plk4 recruitment and centriole duplication. *J. Cell Sci.* **126,** 3223–3233 (2013).

37. Van Breugel, M., Hirono, M., Andreeva, A., *et al.* Structures of SAS-6 Suggest Its Organization in Centrioles. *Science (80-.).* **331,** 1196–1199 (2011).

38. Kitagawa, D., Vakonakis, I., Olieric, N., *et al.* Structural Basis of the 9-Fold Symmetry of Centrioles. *Cell* **144,** 364–375 (2011).

39. Ohta, M., Ashikawa, T., Nozaki, Y., *et al.* Direct interaction of Plk4 with STIL ensures formation of a single procentriole per parental centriole. *Nat. Commun.* **5,** 5267 (2014).

40. Moyer, T. C., Clutario, K. M., Lambrus, B. G., *et al.* Binding of STIL to Plk4 activates kinase activity to promote centriole assembly. *J. Cell Biol.* **209,** 863–878 (2015).

41. Arquint, C., Gabryjonczyk, A.-M., Imseng, S., *et al.* STIL binding to Polo-box 3 of PLK4 regulates centriole duplication. *Elife* **4,** 1–22 (2015).

42. Cottee, M. a, Muschalik, N., Wong, Y. L., *et al.* Crystal structures of the CPAP/STIL complex reveal its role in centriole assembly and human microcephaly. *Elife* **2,** 1–23 (2013).

43. Lin, Y. N., Wu, C. T., Lin, Y. C., *et al.* CEP120 interacts with CPAP and positively regulates centriole elongation. *J. Cell Biol.* **202,** 211–219 (2013).

44. Gudi, R., Haycraft, C. J., Bell, P. D., *et al.* Centrobin-mediated Regulation of the Centrosomal Protein 4.1-associated Protein (CPAP) Level Limits Centriole Length during Elongation Stage. *J. Biol. Chem.* **290,** 6890–6902 (2015).

45. Schmidt, T. I., Kleylein-Sohn, J., Westendorf, J., *et al.* Control of Centriole Length by CPAP and CP110. *Curr. Biol.* **19,** 1005–1011 (2009).

46. Lane, H. a. Antibody microinjection reveals an essential role for human polo-like kinase 1 (Plk1) in the functional maturation of mitotic centrosomes. *J. Cell Biol.* **135,** 1701–1713 (1996).

47. Berdnik, D. & Knoblich, J. a. Drosophila Aurora-A Is Required for Centrosome Maturation and Actin-Dependent Asymmetric Protein Localization during Mitosis. *Curr. Biol.* **12,** 640–647 (2002).

48. Fry, A. M., Mayor, T., Meraldi, P., *et al.* C-Nap1, a novel centrosomal coiled-coil protein and candidate substrate of the cell cycle-regulated protein kinase Nek2. *J. Cell Biol.* **141,** 1563–1574 (1998).

49. Fry, A. M., Meraldi, P. & Nigg, E. a. A centrosomal function for the human Nek2 protein kinase, a member of the NIMA family of cell cycle regulators. *EMBO J.* **17,** 470–481 (1998).

50. Mayor, T., Stierhof, Y. D., Tanaka, K., *et al.* The centrosomal protein C-Nap1 is required for cell cycle-regulated centrosome cohesion. *J. Cell Biol.* **151,** 837–846 (2000).

51. Mayor, T., Hacker, U., Stierhof, Y.-D., *et al.* The mechanism regulating the dissociation of the centrosomal protein C-Nap1 from mitotic spindle poles. *J. Cell Sci.* **115,** 3275–3284 (2002).

52. Faragher, A. J. Nek2A kinase stimulates centrosome disjunction and is required for formation of bipolar mitotic spindles. *Mol. Biol. Cell* **14,** 2876–2889 (2003).

53. Mardin, B. R., Agircan, F. G., Lange, C., *et al.* Plk1 controls the Nek2A-PP1γ Antagonism in centrosome disjunction. *Curr. Biol.* **21,** 1145–1151 (2011).

54. Hardy, T., Lee, M., Hames, R. S., *et al.* Multisite phosphorylation of C-Nap1 releases it from Cep135 to trigger centrosome disjunction. *J. Cell Sci.* **127,** 2493–2506 (2014).

55. Slangy, A., Lane, H. a, D'Hérin, P., *et al.* Phosphorylation by p34cdc2 regulates spindle association of human Eg5, a kinesin-related motor essential for bipolar spindle formation in vivo. *Cell* **83,** 1159–1169 (1995).

56. Tanenbaum, M. E. & Medema, R. H. Mechanisms of Centrosome Separation and Bipolar Spindle Assembly. *Dev. Cell* **19,** 797–806 (2010).

57. Fırat-karalar, E. N. & Stearns, T. The centriole duplication cycle. *Philos. Trans. R. Soc. Lond. B. Biol. Sci.* **369,** 1–10 (2014).

58. Arquint, C., Gabryjonczyk, A.-M. & Nigg, E. a. Centrosomes as signalling centres. *Philos. Trans. R. Soc. B Biol. Sci.* **369,** 20130464–20130464 (2014).

59. Alfaro-Aco, R. & Petry, S. Building the Microtubule Cytoskeleton Piece by Piece. *J. Biol. Chem.* **290,** 17154–17162 (2015).

60. Stehbens, S. & Wittmann, T. Targeting and transport: How microtubules control focal adhesion dynamics. *J. Cell Biol.* **198,** 481–489 (2012).

61. Wadsworth, P. & Khodjakov, A. E pluribus unum: towards a universal mechanism for spindle assembly. *Trends Cell Biol.* **14,** 413–419 (2004).

62. Roubinet, C. & Cabernard, C. Control of asymmetric cell division. *Curr. Opin. Cell Biol.* **31,** 84–91 (2014).

63. Ke, Y.-N. & Yang, W.-X. Primary cilium: an elaborate structure that blocks cell division? *Gene* **547,** 175–185 (2014).

64. Sluder, G. Two-way traffic: centrosomes and the cell cycle. *Nat. Rev. Mol. Cell Biol.* **6,** 743–748 (2005).

65. Doxsey, S., Zimmerman, W. & Mikule, K. Centrosome control of the cell cycle. *Trends Cell Biol.* **15,** 303–311 (2005).

66. Doxsey, S., McCollum, D. & Theurkauf, W. Centrosomes in cellular regulation. *Annu. Rev. Cell Dev. Biol.* **21,** 411–434 (2005).

67. Jackman, M., Lindon, C., Nigg, E. a, *et al.* Active cyclin B1–Cdk1 first appears on centrosomes in prophase. *Nat. Cell Biol.* **5,** 143–148 (2003).

68. Dutertre, S., Cazales, M., Quaranta, M., *et al.* Phosphorylation of CDC25B by Aurora-A at the centrosome contributes to the G2-M transition. *J. Cell Sci.* **117,** 2523–31 (2004).

69. Löffler, H., Rebacz, B., Ho, A. D., *et al.* Chk1-Dependent Regulation of Cdc25B Functions to Coordinate Mitotic Events. *Cell Cycle* **5,** 2543–2547 (2006).

70. Krämer, A., Mailand, N., Lukas, C., *et al.* Centrosome-associated Chk1 prevents

premature activation of cyclin-B-Cdk1 kinase. *Nat. Cell Biol.* **6,** 884–891 (2004).

71. Piel, M. Centrosome-Dependent Exit of Cytokinesis in Animal Cells. *Science (80-.).* **291,** 1550–1553 (2001).

72. Hinchcliffe, E. H. 'It Takes Two to Tango': understanding how centrosome duplication is regulated throughout the cell cycle. *Genes Dev.* **15,** 1167–1181 (2001).

73. Khodjakov, a. Centrosomes Enhance the Fidelity of Cytokinesis in Vertebrates and Are Required for Cell Cycle Progression. *J. Cell Biol.* **153,** 237–242 (2001).

74. Bastos, R. N. & Barr, F. a. Plk1 negatively regulates Cep55 recruitment to the midbody to ensure orderly abscission. *J. Cell Biol.* **191,** 751–760 (2010).

75. Gromley, A. A novel human protein of the maternal centriole is required for the final stages of cytokinesis and entry into S phase. *J. Cell Biol.* **161,** 535–545 (2003).

76. Gromley, A., Yeaman, C., Rosa, J., *et al.* Centriolin Anchoring of Exocyst and SNARE Complexes at the Midbody Is Required for Secretory-Vesicle-Mediated Abscission. *Cell* **123,** 75–87 (2005).

77. Fabbro, M., Zhou, B.-B., Takahashi, M., *et al.* Cdk1/Erk2- and Plk1-Dependent Phosphorylation of a Centrosome Protein, Cep55, Is Required for Its Recruitment to Midbody and Cytokinesis. *Dev. Cell* **9,** 477–488 (2005).

78. Hinchcliffe, E. H. Requirement of a Centrosomal Activity for Cell Cycle Progression Through G1 into S Phase. *Science (80-.).* **291,** 1547–1550 (2001).

79. Maniotis, a & Schliwa, M. Microsurgical removel of centrosomes blocks cell reproduction and centriole regeneration in BSC-1 cells. *Trends Cell Biol.* **2,** 39 (1992).

80. Uetake, Y., Loncarek, J., Nordberg, J. J., *et al.* Cell cycle progression and de novo centriole assembly after centrosomal removal in untransformed human cells. *J. Cell Biol.* **176,** 173–182 (2007).

81. Srsen, V. Inhibition of centrosome protein assembly leads to p53-dependent exit from the cell cycle. *J. Cell Biol.* **174,** 625–630 (2006).

82. Mikule, K., Delaval, B., Kaldis, P., *et al.* Loss of centrosome integrity induces p38-p53-p21-dependent G1-S arrest. *Nat. Cell Biol.* **9,** 160–170 (2007).

83. Hoeijmakers, J. H. Genome maintenance mechanisms for preventing cancer. *Nature* **411,** 366–74 (2001).

84. Bartek, J. & Lukas, J. DNA damage checkpoints: from initiation to recovery or adaptation. *Curr. Opin. Cell Biol.* **19,** 238–245 (2007).

85. Kastan, M. B. & Bartek, J. Cell-cycle checkpoints and cancer. *Nature* **432,** 316–323 (2004).

86. Stracker, T. H., Roig, I., Knobel, P. a., *et al.* The ATM signaling network in development and disease. *Front. Genet.* **4,** 1–19 (2013).

87. Smits, V. a. J. & Gillespie, D. a. DNA damage control: regulation and functions of checkpoint kinase 1. *FEBS J.* **282,** 3681–3692 (2015).

88. Shaltiel, I. a., Krenning, L., Bruinsma, W., *et al.* The same, only different - DNA damage checkpoints and their reversal throughout the cell cycle. *J. Cell Sci.* **128,** 607–620 (2015).

89. Bouwman, P. & Jonkers, J. The effects of deregulated DNA damage signalling on cancer chemotherapy response and resistance. *Nat. Rev. Cancer* **12,** 587–598 (2012).

90. Tsvetkov, L. Polo-like Kinase 1 and Chk2 Interact and Co-localize to Centrosomes and the Midbody. *J. Biol. Chem.* **278,** 8468–8475 (2003).

91. Zhang, S., Hemmerich, P. & Grosse, F. Centrosomal localization of DNA damage checkpoint proteins. *J. Cell. Biochem.* **101,** 451–465 (2007).

92. Van Vugt, M. a T. M., Gardino, A. K., Linding, R., *et al.* A mitotic phosphorylation feedback network connects Cdk1, Plk1, 53BP1, and Chk2 to inactivate the G2/M DNA damage checkpoint. *PLoS Biol.* **8,** (2010).

93. Löffler, H., Bochtler, T., Fritz, B., *et al.* DNA Damage-Induced Accumulation of Centrosomal Chk1 Contributes to its Checkpoint Function. *Cell Cycle* **6,** 2541–2548 (2007).

94. Hanahan, D. & Weinberg, R. A. Hallmarks of Cancer: The Next Generation. *Cell* **144,** 646–674 (2011).

95. Chan, J. Y. A clinical overview of centrosome amplification in human cancers. *Int. J. Biol. Sci.* **7,** 1122–1144 (2011).

96. Fukasawa, K., Choi, T., Kuriyama, R., *et al.* Abnormal Centrosome Amplification in the Absence of p53. *Science (80-.).* **271,** 1744–1747 (1996).

97. Salisbury, J. L., D'Assoro, A. B. & Lingle, W. L. Centrosome Amplification and the Origin of Chromosomal Instability in Breast Cancer. *J. Mammary Gland Biol. Neoplasia* **9,** 275–283 (2004).

98. D'Assoro, A. B., Lingle, W. L. & Salisbury, J. L. Centrosome amplification and the development of cancer. *Oncogene* **21,** 6146–6153 (2002).

99. La Terra, S. The de novo centriole assembly pathway in HeLa cells: cell cycle progression and centriole assembly/maturation. *J. Cell Biol.* **168,** 713–722 (2005).

100. Khodjakov, A. De novo formation of centrosomes in vertebrate cells arrested during S phase. *J. Cell Biol.* **158,** 1171–1181 (2002).

101. Fujiwara, T., Bandi, M., Nitta, M., *et al.* Cytokinesis failure generating tetraploids promotes tumorigenesis in p53-null cells. *Nature* **437,** 1043–1047 (2005).

102. Meraldi, P. Aurora-A overexpression reveals tetraploidization as a major route to centrosome amplification in p53-/- cells. *EMBO J.* **21,** 483–492 (2002).

103. Kleylein-Sohn, J., Pollinger, B., Ohmer, M., *et al.* Acentrosomal spindle organization renders cancer cells dependent on the kinesin HSET. *J. Cell Sci.* **125,** 5391–5402 (2012).

104. Lingle, W. L., Lutz, W. H., Ingle, J. N., *et al.* Centrosome hypertrophy in human breast tumors: implications for genomic stability and cell polarity. *Proc. Natl. Acad. Sci. U. S. A.* **95,** 2950–2955 (1998).

105. Lingle, W. L. & Salisbury, J. L. Altered centrosome structure is associated with abnormal mitoses in human breast tumors. *Am. J. Pathol.* **155,** 1941–51 (1999).

106. Pihan, G. a., Wallace, J., Zhou, Y., *et al.* Centrosome abnormalities and chromosome instability occur together in pre-invasive carcinomas. *Cancer Res.* **63,** 1398–1404 (2003).

107. Gisselsson, D., Håkanson, U., Stoller, P., *et al.* When the Genome Plays Dice: Circumvention of the Spindle Assembly Checkpoint and Near-Random Chromosome Segregation in Multipolar Cancer Cell Mitoses. *PLoS One* **3,** e1871 (2008).

108. Vitale, I., Galluzzi, L., Castedo, M., *et al.* Mitotic catastrophe: a mechanism for avoiding genomic instability. *Nat. Rev. Mol. Cell Biol.* **12,** 385–392 (2011).

109. Varmark, H., Sparks, C. a, Nordberg, J. J., *et al.* DNA damage-induced cell death is enhanced by progression through mitosis. *Cell Cycle* **8,** 2952–2964 (2009).

110. Brinkley, B. R. Managing the centrosome numbers game: From chaos to stability in cancer cell division. *Trends Cell Biol.* **11,** 18–21 (2001).

111. Ganem, N. J., Godinho, S. a. & Pellman, D. A mechanism linking extra centrosomes to chromosomal instability. *Nature* **460,** 278–282 (2009).

112. Gregan, J., Polakova, S., Zhang, L., *et al.* Merotelic kinetochore attachment: causes and effects. *Trends Cell Biol.* **21,** 374–381 (2011).

113. Salmon, E. D., Cimini, D., Cameron, L. a, *et al.* Merotelic kinetochores in mammalian tissue cells. *Philos. Trans. R. Soc. B Biol. Sci.* **360,** 553–568 (2005).

114. Cimini, D. Merotelic kinetochore orientation occurs frequently during early mitosis in mammalian tissue cells and error correction is achieved by two different mechanisms. *J. Cell Sci.* **116,** 4213–4225 (2003).

115. Leber, B., Maier, B., Fuchs, F., *et al.* Proteins required for centrosome clustering in cancer cells. *Sci. Transl. Med.* **2,** 33ra38 (2010).

116. Bakhoum, S. F., Genovese, G. & Compton, D. a. Deviant Kinetochore Microtubule Dynamics Underlie Chromosomal

Instability. *Curr. Biol.* **19,** 1937–1942 (2009).

117. Yao, Y. & Dai, W. Shugoshins function as a guardian for chromosomal stability in nuclear division. *Cell Cycle* **11,** 2631–2642 (2012).

118. Sagona, A. P. & Stenmark, H. Cytokinesis and cancer. *FEBS Lett.* **584,** 2652–2661 (2010).

119. Rieder, C. L. Mitosis in vertebrates: the G2/M and M/A transitions and their associated checkpoints. *Chromosom. Res.* **19,** 291–306 (2011).

120. Sasaki, T., Brakebusch, C., Engel, J., *et al.* Mac-2 binding protein is a cell-adhesive protein of the extracellular matrix which self-assembles into ring-like structures and binds β1 integrins, collagens and fibronectin. *EMBO J.* **17,** 1606–1613 (1998).

121. Müller, S. a, Sasaki, T., Bork, P., *et al.* Domain organization of Mac-2 binding protein and its oligomerization to linear and ring-like structures. *J. Mol. Biol.* **291,** 801–813 (1999).

122. Martínez, V. G., Moestrup, S. K., Holmskov, U., *et al.* The conserved scavenger receptor cysteine-rich superfamily in therapy and diagnosis. *Pharmacol. Rev.* **63,** 967–1000 (2011).

123. Lodermeyer, V., Suhr, K., Schrott, N., *et al.* 90K, an interferon-stimulated gene product, reduces the infectivity of HIV-1. *Retrovirology* **10,** 111 (2013).

124. Robinson, D. N. Drosophila Kelch Is an Oligomeric Ring Canal Actin Organizer. *J. Cell Biol.* **138,** 799–810 (1997).

125. Ahmad, K. F., Engel, C. K. & Prive, G. G. Crystal structure of the BTB domain from PLZF. *Proc. Natl. Acad. Sci.* **95,** 12123–12128 (1998).

126. Li, X., Peng, H., Schultz, D. C., *et al.* Structure-function studies of the BTB/POZ transcriptional repression domain from the promyelocytic leukemia zinc finger oncoprotein. *Cancer Res.* **59,** 5275–82 (1999).

127. Hellstern, S. Functional Studies on Recombinant Domains of Mac-2-binding Protein. *J. Biol. Chem.* **277,** 15690–15696 (2002).

128. Fogeron, M.-L., Müller, H., Schade, S., *et al.* LGALS3BP regulates centriole biogenesis and centrosome hypertrophy in cancer cells. *Nat. Commun.* **4,** 1531 (2013).

129. Grassadonia, A., Tinari, N., Iurisci, I., *et al.* 90K (Mac-2 BP) and galectins in tumor progression and metastasis. *Glycoconj. J.* **19,** 551–6 (2004).

130. Inohara, H., Akahani, S., Koths, K., *et al.* Interactions between Galectin-3 and Mac-2-Binding Protein Mediate Cell-Cell adhedion. *Cancer Res* **56,** 4530–4534 (1996).

131. Ullrich, A., Sures, I., D'Egidio, M., *et al.* The secreted tumor-associated antigen 90K is a potent immune stimulator. *J. Biol. Chem.* **269,** 18401–18407 (1994).

132. Powell, T. J., Schreck, R., McCall, M., *et al.* A tumor-derived protein which provides T-cell costimulation through accessory cell activation. *J. Immunother. Emphasis Tumor Immunol.* **17,** 209–221 (1995).

133. Natoli, C., Iacobelli, S. & Kohn, L. The immune stimulatory protein 90K increases major histocompatibility complex class I expression in a human breast cancer cell line. *Biochem. Biophys. Res. Commun.* **225,** 617–20 (1996).

134. Koths, K., Taylor, E., Halenbeck, R., *et al.* Cloning and characterization of a human Mac-2-binding protein, a new member of the superfamily defined by the macrophage scavenger receptor cysteine-rich domain. *J. Biol. Chem.* **268,** 14245–9 (1993).

135. Iacobelli, S., Arnò, E., D'Orazio, A., *et al.* Detection of antigens recognized by a novel monoclonal antibody in tissue and serum from patients with breast cancer. *Cancer Res.* **46,** 3005–10 (1986).

136. D'Ostilio, N., Sabatino, G., Natoli, C., *et al.* 90K (Mac-2 BP) in human milk. *Clin. Exp. Immunol.* **104,** 543–6 (1996).

137. Warke, R. V, Becerra, A., Zawadzka, A., *et al.* Efficient dengue virus (DENV) infection of human muscle satellite cells upregulates type I interferon response genes and differentially modulates MHC I expression on bystander and DENV-infected cells. *J. Gen. Virol.* **89,** 1605–1615 (2008).

138. Kittl, E. M., Hofmann, J., Hartmann, G., *et al.* Serum Protein 90K/Mac-2BP Is an Independent Predictor of Disease Severity during Hepatitis C Virus Infection. *Clin. Chem. Lab. Med.* **38,** 205–208 (2000).

139. Natoli, C., Dianzani, F., Mazzotta, F., *et al.* 90K protein: a new predictor marker of disease progression in human immunodeficiency virus infection. *J. Acquir. Immune Defic. Syndr.* **6,** 370–5 (1993).

140. Pelliccia, P., Galli, L., De Martino, M., *et al.* Lack of mother-to-child HIV-1 transmission is associated with elevated serum levels of 90 K immune modulatory protein. *AIDS* **14,** F41–F45 (2000).

141. Iacobelli, S., Sismondi, P., Giai, M., *et al.* Prognostic value of a novel circulating serum 90K antigen in breast cancer. *Br. J. Cancer* **69,** 172–6 (1994).

142. Tinari, N., Lattanzio, R., Querzoli, P., *et al.* High expression of 90K (Mac-2 BP) is associated with poor survival in node-negative breast cancer patients not receiving adjuvant systemic therapies. *Int. J. Cancer* **124,** 333–338 (2009).

143. Iacovazzi, P. a, Trisolini, a, Barletta, D., *et al.* Serum 90K/MAC-2BP glycoprotein in patients with liver cirrhosis and hepatocellular carcinoma: a comparison with alpha-fetoprotein. *Clin. Chem. Lab. Med.* **39,** 961–965 (2001).

144. Kunzli, B. M., Berberat, P. O., Zhu, Z. W., *et al.* Influences of the lysosomal associated membrane proteins (Lamp-1, Lamp-2) and Mac-2 binding protein (Mac-2-BP) on the prognosis of pancreatic carcinoma. *Cancer* **94,** 228–239 (2002).

145. Marchetti, A., Tinari, N., Buttitta, F., *et al.* Expression of 90K (Mac-2 BP) correlates with distant metastasis and predicts survival in stage I non-small cell lung cancer patients. *Cancer Res.* **62,** 2535–2539 (2002).

146. Ozaki, Y., Kontani, K., Hanaoka, J., *et al.* Expression and immunogenicity of a tumor-associated antigen, 90K/Mac-2 binding protein, in lung carcinoma. *Cancer* **95,** 1954–62 (2002).

147. Park, Y. P., Choi, S.-C., Kim, J. H., *et al.* Up-regulation of Mac-2 binding protein by hTERT in gastric cancer. *Int. J. Cancer* **120,** 813–20 (2007).

148. Shirure, V. S., Reynolds, N. M. & Burdick, M. M. Mac-2 Binding Protein Is a Novel E-Selectin Ligand Expressed by Breast Cancer Cells. *PLoS One* **7,** (2012).

149. Weng, L.-P., Wu, C.-C., Hsu, B.-L., *et al.* Secretome-based identification of Mac-2 binding protein as a potential oral cancer marker involved in cell growth and motility. *J. Proteome Res.* **7,** 3765–75 (2008).

150. Kim, Y.-S., Jung, J.-A., Kim, H.-J., *et al.* Galectin-3 binding protein promotes cell motility in colon cancer by stimulating the shedding of protein tyrosine phosphatase kappa by proprotein convertase 5. *Biochem. Biophys. Res. Commun.* **404,** 96–102 (2011).

151. Fornarini, B., Ambrosio, C. D., Natoli, C., *et al.* Adhesion to 90K (Mac-2 BP) as a mechanism for lymphoma drug resistance in vivo. *Blood* **96,** 3282–3285 (2000).

152. Laubli, H., Alisson-Silva, F., Stanczak, M. a, *et al.* Lectin Galactoside-binding Soluble 3 Binding Protein (LGALS3BP) Is a Tumor-associated Immunomodulatory Ligand for CD33-related Siglecs. *J. Biol. Chem.* **289,** 33481–33491 (2014).

153. Stampolidis, P., Ullrich, a & Iacobelli, S. LGALS3BP, lectin galactoside-binding soluble 3 binding protein, promotes oncogenic cellular events impeded by antibody intervention. *Oncogene* **34,** 39–52 (2015).

154. Zambelli, D., Zuntini, M., Nardi, F., *et al.* Biological indicators of prognosis in Ewing's sarcoma: An emerging role for lectin galactoside-binding soluble 3 binding protein (LGALS3BP). *Int. J. Cancer* **126,** 41–52 (2010).

155. Lee, J. H., Bae, J. a, Lee, J. H., *et al.* Glycoprotein 90K, downregulated in advanced colorectal cancer tissues, interacts with CD9/CD82 and suppresses the Wnt/ -catenin signal via ISGylation of -catenin. *Gut* **59,** 907–917 (2010).

156. Jallal, B., Powell, J., Zachwieja, J., *et al.* Suppression of Tumor Growth in Vivo by Local and Systemic 90K Level Increase Advances in Brief Suppression of Tumor

Growth in Vivo by Local and Systemic 90K Level Increase1. *Cell* 3223–3227 (1995).

157. Piccolo, E., Tinari, N., D'Addario, D., *et al.* Prognostic relevance of LGALS3BP in human colorectal carcinoma. *J. Transl. Med.* **13,** 248 (2015).

158. Brakebusch, C., Sures, I., Jallal, B., *et al.* Isolation and functional characterization of the human 90K promoter. *Genomics* **57,** 268–278 (1999).

159. Yan, B., Yang, X., Lee, T.-L., *et al.* Genome-wide identification of novel expression signatures reveal distinct patterns and prevalence of binding motifs for p53, nuclear factor-κB and other signal transcription factors in head and neck squamous cell carcinoma. *Genome Biol.* **8,** R78 (2007).

160. Iacobelli, S., Scambia, G., Natoli, C., *et al.* Recombinant human leukocyte interferon-alpha 2b stimulates the synthesis and release of a 90K tumor-associated antigen in human breast cancer cells. *Int J Cancer* **42,** 182–184 (1988).

161. Marth, C., Dreps, A., Natoli, C., *et al.* Effects of type-I and -II interferons on 90K antigen expression in ovarian carcinoma cells. *Int J Cancer* **59,** 808–813 (1994).

162. D'Ostilio, N., Natoli, C., Grassadonia, A., *et al.* Prognostic Value of a Novel Interferon-inducible 90K Tumor Antigen. *Ann. N. Y. Acad. Sci.* **784,** 288–293 (1996).

163. Grassadonia, A., Tinari, N., Fiorentino, B., *et al.* The 90K Protein Increases Major Histocompatibility Complex Class I Expression and Is Regulated by Hormones, γ-Interferon, and Double-Strand Polynucleotides. *Endocrinology* **145,** 4728–4736 (2004).

164. Noma, N., Simizu, S., Kambayashi, Y., *et al.* Involvement of NF-κB-mediated expression of galectin-3-binding protein in TNF-α-induced breast cancer cell adhesion. *Oncol. Rep.* **27,** 2080–4 (2012).

165. Park, Y. P., Choi, S.-C., Kim, B.-Y., *et al.* Induction of Mac-2BP by nerve growth factor is regulated by the PI3K/Akt/NF-kappaB-dependent pathway in the HEK293 cell line. *BMB Rep.* **41,** 784–9 (2008).

166. Rivenbark, A. G., Jones, W. D., Risher, J. D., *et al.* DNA Methylation-Dependent Epigenetic Regulation of Gene Expression in MCF-7 Breast Cancer Cells. *Epigenetics* **1,** 33–45 (2006).

167. Endo, H., Muramatsu, T., Furuta, M., *et al.* Potential of tumor-suppressive miR-596 targeting LGALS3BP as a therapeutic agent in oral cancer. *Carcinogenesis* **34,** 560–9 (2013).

168. Feinberg, A. P., Ohlsson, R. & Henikoff, S. The epigenetic progenitor origin of human cancer. *Nat. Rev. Genet.* **7,** 21–33 (2006).

169. Tsai, H.-C. & Baylin, S. B. Cancer epigenetics: linking basic biology to clinical medicine. *Cell Res.* **21,** 502–517 (2011).

170. Kanwal, R., Gupta, K. & Gupta, S. in *Cancer Epigenetics* (ed. Verma, M.) **1238,** 3–25 (Springer New York, 2015).

171. Portela, A. & Esteller, M. Epigenetic modifications and human disease. *Nat. Biotechnol.* **28,** 1057–1068 (2010).

172. Shinjo, K. & Kondo, Y. Targeting cancer epigenetics: Linking basic biology to clinical medicine. *Adv. Drug Deliv. Rev.* (2015). doi:10.1016/j.addr.2015.10.006

173. McGhee, J. D. & Felsenfeld, G. Nucleosome Structure. *Annu. Rev. Biochem.* **49,** 1115–1156 (1980).

174. Simpson, R. T. Structure of the chromatosome, a chromatin particle containing 160 base pairs of DNA and all the histones. *Biochemistry* **17,** 5524–5531 (1978).

175. Kouzarides, T. Chromatin Modifications and Their Function. *Cell* **128,** 693–705 (2007).

176. Bannister, A. J. & Kouzarides, T. Regulation of chromatin by histone modifications. *Cell Res.* **21,** 381–395 (2011).

177. Tessarz, P. & Kouzarides, T. Histone core modifications regulating nucleosome structure and dynamics. *Nat. Rev. Mol. Cell Biol.* **15,** 703–708 (2014).

178. Rodríguez-Paredes, M. & Esteller, M. Cancer epigenetics reaches mainstream oncology. *Nat. Med.* **17,** 330–339 (2011).

179. Lee, T. I. & Young, R. A. Transcriptional Regulation and Its Misregulation in Disease. *Cell* **152,** 1237–1251 (2013).

180. Zhang, T., Cooper, S. & Brockdorff, N. The interplay of histone modifications - writers that read. *EMBO Rep.* **16,** 1467–1481 (2015).

181. Annalisa, I. & Robert, S. The role of linker histone H1 modifications in the regulation of gene expression and chromatin dynamics. *Biochim. Biophys. Acta - Gene Regul. Mech.* 1–10 (2015). doi:10.1016/j.bbagrm.2015.09.003

182. Bartke, T., Vermeulen, M., Xhemalce, B., *et al.* Nucleosome-Interacting Proteins Regulated by DNA and Histone Methylation. *Cell* **143,** 470–484 (2010).

183. Vermeulen, M., Eberl, H. C., Matarese, F., *et al.* Quantitative Interaction Proteomics and Genome-wide Profiling of Epigenetic Histone Marks and Their Readers. *Cell* **142,** 967–980 (2010).

184. Wu, S.-Y. & Chiang, C.-M. The Double Bromodomain-containing Chromatin Adaptor Brd4 and Transcriptional Regulation. *J. Biol. Chem.* **282,** 13141–13145 (2007).

185. Jung, M., Gelato, K. a., Fernández-Montalván, A., *et al.* Targeting BET bromodomains for cancer treatment. *Epigenomics* **7,** 487–501 (2015).

186. Dey, A., Chitsaz, F., Abbasi, A., *et al.* The double bromodomain protein Brd4 binds to acetylated chromatin during interphase and mitosis. *Proc. Natl. Acad. Sci.* **100,** 8758–8763 (2003).

187. Nishiyama, A. Brd4 Is Required for Recovery from Antimicrotubule Drug-induced Mitotic Arrest: Preservation of Acetylated Chromatin. *Mol. Biol. Cell* **17,** 814–823 (2005).

188. Yang, Z., Yik, J. H. N., Chen, R., *et al.* Recruitment of P-TEFb for Stimulation of Transcriptional Elongation by the Bromodomain Protein Brd4. *Mol. Cell* **19,** 535–545 (2005).

189. Peng, J., Marshall, N. F. & Price, D. H. Identification of a Cyclin Subunit Required for the Function of Drosophila P-TEFb. *J. Biol. Chem.* **273,** 13855–13860 (1998).

190. Price, D. H. P-TEFb, a Cyclin-Dependent Kinase Controlling Elongation by RNA Polymerase II. *Mol. Cell. Biol.* **20,** 2629–2634 (2000).

191. Zhou, M., Halanski, M. a, Radonovich, M. F., *et al.* Tat Modifies the Activity of CDK9 To Phosphorylate Serine 5 of the RNA Polymerase II Carboxyl-Terminal Domain during Human Immunodeficiency Virus Type 1 Transcription. *Mol. Cell. Biol.* **20,** 5077–5086 (2000).

192. Itzen, F., Greifenberg, A. K., Bösken, C. a., *et al.* Brd4 activates P-TEFb for RNA polymerase II CTD phosphorylation. *Nucleic Acids Res.* **42,** 7577–7590 (2014).

193. Jang, M. K., Mochizuki, K., Zhou, M., *et al.* The Bromodomain Protein Brd4 Is a Positive Regulatory Component of P-TEFb and Stimulates RNA Polymerase II-Dependent Transcription. *Mol. Cell* **19,** 523–534 (2005).

194. Devaiah, B. N., Lewis, B. a., Cherman, N., *et al.* BRD4 is an atypical kinase that phosphorylates Serine2 of the RNA Polymerase II carboxy-terminal domain. *Proc. Natl. Acad. Sci.* **109,** 6927–6932 (2012).

195. Lovén, J., Hoke, H. A., Lin, C. Y., *et al.* Selective Inhibition of Tumor Oncogenes by Disruption of Super-Enhancers. *Cell* **153,** 320–334 (2013).

196. Devaiah, B. N. & Singer, D. S. Two faces of brd4: mitotic bookmark and transcriptional lynchpin. *Transcription* **4,** 13–7 (2012).

197. Fowler, T., Ghatak, P., Price, D. H., *et al.* Regulation of MYC Expression and Differential JQ1 Sensitivity in Cancer Cells. *PLoS One* **9,** e87003 (2014).

198. Kuzmichev, a. Histone methyltransferase activity associated with a human multiprotein complex containing the Enhancer of Zeste protein. *Genes Dev.* **16,** 2893–2905 (2002).

199. Ferrari, K. J., Scelfo, A., Jammula, S., *et al.* Polycomb-Dependent H3K27me1 and H3K27me2 Regulate Active Transcription and Enhancer Fidelity. *Mol. Cell* **53,** 49–62 (2014).

200. Marchesi, I., Giordano, A. & Bagella, L. Roles of enhancer of zeste homolog 2: From skeletal muscle differentiation to rhabdomyosarcoma carcinogenesis. *Cell Cycle* **13,** 516–527 (2014).

201. Cao, R. Role of Histone H3 Lysine 27 Methylation in Polycomb-Group Silencing. *Science (80-.).* **298,** 1039–1043 (2002).

202. Simon, J. a & Lange, C. a. Roles of the EZH2 histone methyltransferase in cancer epigenetics. *Mutat. Res. Mol. Mech. Mutagen.* **647,** 21–29 (2008).

203. Chang, C.-J., Yang, J.-Y., Xia, W., *et al.* EZH2 Promotes Expansion of Breast Tumor Initiating Cells through Activation of RAF1-β-Catenin Signaling. *Cancer Cell* **19,** 86–100 (2011).

204. Melling, N., Thomsen, E., Tsourlakis, M. C., *et al.* Overexpression of enhancer of zeste homolog 2 (EZH2) characterizes an aggressive subset of prostate cancers and predicts patient prognosis independently from pre- and postoperatively assessed clinicopathological parameters. *Carcinogenesis* **36,** 1333–1340 (2015).

205. Mills, A. a. Throwing the cancer switch: reciprocal roles of polycomb and trithorax proteins. *Nat. Rev. Cancer* **10,** 669–682 (2010).

206. Kleer, C. G., Cao, Q., Varambally, S., *et al.* EZH2 is a marker of aggressive breast cancer and promotes neoplastic transformation of breast epithelial cells. *Proc. Natl. Acad. Sci.* **100,** 11606–11611 (2003).

207. Gonzalez, M. E., DuPrie, M. L., Krueger, H., *et al.* Histone Methyltransferase EZH2 Induces Akt-Dependent Genomic Instability and BRCA1 Inhibition in Breast Cancer. *Cancer Res.* **71,** 2360–2370 (2011).

208. Varambally, S., Dhanasekaran, S. M., Zhou, M., *et al.* The polycomb group protein EZH2 is involved in progression of prostate cancer. *Nature* **419,** 624–629 (2002).

209. Qi, W., Chan, H., Teng, L., *et al.* Selective inhibition of Ezh2 by a small molecule inhibitor blocks tumor cells proliferation. *Proc. Natl. Acad. Sci.* **109,** 21360–21365 (2012).

210. Fan, T.-Y., Wang, H., Xiang, P., *et al.* Inhibition of EZH2 reverses chemotherapeutic drug TMZ chemosensitivity in glioblastoma. *Int. J. Clin. Exp. Pathol.* **7,** 6662–70 (2014).

211. McCabe, M. T., Ott, H. M., Ganji, G., *et al.* EZH2 inhibition as a therapeutic strategy for lymphoma with EZH2-activating mutations. *Nature* **492,** 108–112 (2012).

212. Wang, Y. & Leung, F. C. C. An evaluation of new criteria for CpG islands in the human genome as gene markers. *Bioinformatics* **20,** 1170–1177 (2004).

213. Bird, A. DNA methylation patterns and epigenetic memory. *Genes Dev.* **16,** 6–21 (2002).

214. Bird, A. P. CpG-rich islands and the function of DNA methylation. *Nature* **321,** 209–213 (1986).

215. Mohandas, T., Sparkes, R. & Shapiro, L. Reactivation of an inactive human X chromosome: evidence for X inactivation by DNA methylation. *Science (80-.).* **211,** 393–396 (1981).

216. Li, E., Beard, C. & Jaenisch, R. Role for DNA methylation in genomic imprinting. *Nature* **366,** 362–365 (1993).

217. Illingworth, R., Kerr, A., DeSousa, D., *et al.* A Novel CpG Island Set Identifies Tissue-Specific Methylation at Developmental Gene Loci. *PLoS Biol.* **6,** e22 (2008).

218. Bird, A. P. Gene number, noise reduction and biological complexity. *Trends Genet.* **11,** 94–100 (1995).

219. Smith, Z. D. & Meissner, A. DNA methylation: roles in mammalian development. *Nat. Rev. Genet.* **14,** 204–220 (2013).

220. Futscher, B. W., Oshiro, M. M., Wozniak, R. J., *et al.* Role for DNA methylation in the control of cell type–specific maspin expression. *Nat. Genet.* **31,** 175–179 (2002).

221. Hattori, N., Nishino, K., Ko, Y. G., *et al.* Epigenetic control of mouse Oct-4 gene expression in embryonic stem cells and trophoblast stem cells. *J. Biol. Chem.* **279,** 17063–17069 (2004).

222. Han, H., Cortez, C. C., Yang, X., *et al.* DNA methylation directly silences genes with non-CpG island promoters and establishes a nucleosome occupied promoter. *Hum. Mol. Genet.* **20,** 4299–4310 (2011).

223. Okano, M., Bell, D. W., Haber, D. a, *et al.* DNA Methyltransferases Dnmt3a and Dnmt3b Are Essential for De Novo Methylation and Mammalian Development. *Cell* **99,** 247–257 (1999).

224. Kim, G.-D. Co-operation and communication between the human maintenance and de novo DNA (cytosine-5) methyltransferases. *EMBO J.* **21,** 4183–4195 (2002).

225. Sharma, S., Kelly, T. K. & Jones, P. a. Epigenetics in cancer. *Carcinogenesis* **31,** 27–36 (2010).

226. Prendergast, G. & Ziff, E. Methylation-sensitive sequence-specific DNA binding by the c-Myc basic region. *Science (80-.).* **251,** 186–189 (1991).

227. Watt, F. & Molloy, P. L. Cytosine methylation prevents binding to DNA of a HeLa cell transcription factor required for optimal expression of the adenovirus major late promoter. *Genes Dev.* **2,** 1136–1143 (1988).

228. Jones, P. L., Veenstra, G. J., Wade, P. a, *et al.* Methylated DNA and MeCP2 recruit histone deacetylase to repress transcription. *Nat. Genet.* **19,** 187–191 (1998).

229. Nan, X., Ng, H. H., Johnson, C. a, *et al.* Transcriptional repression by the methyl-CpG-binding protein MeCP2 involves a histone deacetylase complex. *Nature* **393,** 386–389 (1998).

230. Viré, E., Brenner, C., Deplus, R., *et al.* The Polycomb group protein EZH2 directly controls DNA methylation. *Nature* **439,** 871–874 (2005).

231. Sana, J., Faltejskova, P., Svoboda, M., *et al.* Novel classes of non-coding RNAs and cancer. *J. Transl. Med.* **10,** 103 (2012).

232. He, L. & Hannon, G. J. MicroRNAs: small RNAs with a big role in gene regulation. *Nat. Rev. Genet.* **5,** 522–531 (2004).

233. Lee, Y., Kim, M., Han, J., *et al.* MicroRNA genes are transcribed by RNA polymerase II. *EMBO J.* **23,** 4051–4060 (2004).

234. Saito, Y. & Jones, P. M. Epigenetic Activation of Tumor Suppressor MicroRNAs in Human Cancer Cells. *Cell Cycle* **5,** 2220–2222 (2006).

235. Fabbri, M., Garzon, R., Cimmino, A., *et al.* MicroRNA-29 family reverts aberrant methylation in lung cancer by targeting DNA methyltransferases 3A and 3B. *Proc. Natl. Acad. Sci.* **104,** 15805–15810 (2007).

236. Friedman, J. M., Liang, G., Liu, C.-C., *et al.* The Putative Tumor Suppressor microRNA-101 Modulates the Cancer Epigenome by Repressing the Polycomb Group Protein EZH2. *Cancer Res.* **69,** 2623–2629 (2009).

237. Alajez, N. M., Shi, W., Hui, a B. Y., *et al.* Enhancer of Zeste homolog 2 (EZH2) is overexpressed in recurrent nasopharyngeal carcinoma and is regulated by miR-26a, miR-101, and miR-98. *Cell Death Dis.* **1,** e85 (2010).

238. Lu, J., He, M.-L., Wang, L., *et al.* MiR-26a Inhibits Cell Growth and Tumorigenesis of Nasopharyngeal Carcinoma through Repression of EZH2. *Cancer Res.* **71,** 225–233 (2011).

239. Jansen, M. P. H. M., Reijm, E. a., Sieuwerts, a. M., *et al.* High miR-26a and low CDC2 levels associate with decreased EZH2 expression and with favorable outcome on tamoxifen in metastatic breast cancer. *Breast Cancer Res. Treat.* **133,** 937–947 (2012).

240. Koh, C. M., Iwata, T., Zheng, Q., *et al.* MYC enforces overexpression of EZH2 in early prostatic neoplasia via transcriptional and posttranscriptional mechanisms. *Cancer Res.* **71,** 263–263 (2011).

241. Sander, S., Bullinger, L., Klapproth, K., *et al.* MYC stimulates EZH2 expression by repression of its negative regulator miR-26a. *Blood* **112,** 4202–4212 (2008).

242. Salvatori, B., Iosue, I., Djodji Damas, N., *et al.* Critical Role of c-Myc in Acute Myeloid Leukemia Involving Direct Regulation of miR-26a and Histone Methyltransferase EZH2. *Genes Cancer* **2,** 585–592 (2011).

243. Börno, S. T., Fischer, A., Kerick, M., *et al.* Genome-wide DNA Methylation Events in TMPRSS2-ERG Fusion-Negative Prostate Cancers Implicate an EZH2-Dependent Mechanism with miR-26a Hypermethylation. *Cancer Discov.* **2,** 1024–1035 (2012).

244. Davidovich, C. & Cech, T. R. The recruitment of chromatin modifiers by long noncoding RNAs: lessons from PRC2. *RNA* **21,** 2007–2022 (2015).

245. Jiang, C. & Pugh, B. F. Nucleosome positioning and gene regulation: advances

through genomics. *Nat. Rev. Genet.* **10,** 161–172 (2009).

246. Schones, D. E., Cui, K., Cuddapah, S., *et al.* Dynamic Regulation of Nucleosome Positioning in the Human Genome. *Cell* **132,** 887–898 (2008).

247. Sarma, K. & Reinberg, D. Histone variants meet their match. *Nat. Rev. Mol. Cell Biol.* **6,** 139–149 (2005).

248. Burgess, R. J. & Zhang, Z. Histone chaperones in nucleosome assembly and human disease. *Nat. Struct. Mol. Biol.* **20,** 14–22 (2013).

249. Ausio, J. Histone variants--the structure behind the function. *Briefings Funct. Genomics Proteomics* **5,** 228–243 (2006).

250. Hake, S. B., Garcia, B. a, Kauer, M., *et al.* Serine 31 phosphorylation of histone variant H3.3 is specific to regions bordering centromeres in metaphase chromosomes. *Proc. Natl. Acad. Sci.* **102,** 6344–6349 (2005).

251. Elsässer, S. J., Huang, H., Lewis, P. W., *et al.* DAXX envelops a histone H3.3–H4 dimer for H3.3-specific recognition. *Nature* **491,** 560–565 (2012).

252. Wen, H., Li, Y., Xi, Y., *et al.* ZMYND11 links histone H3.3K36me3 to transcription elongation and tumour suppression. *Nature* **508,** 263–268 (2014).

253. Ahmad, K. & Henikoff, S. The Histone Variant H3.3 Marks Active Chromatin by Replication-Independent Nucleosome Assembly. *Mol. Cell* **9,** 1191–1200 (2002).

254. Chen, P., Zhao, J., Wang, Y., *et al.* H3.3 actively marks enhancers and primes gene transcription via opening higher-ordered chromatin. *Genes Dev.* **27,** 2109–2124 (2013).

255. Jin, C. & Felsenfeld, G. Nucleosome stability mediated by histone variants H3.3 and H2A.Z. *Genes Dev.* **21,** 1519–1529 (2007).

256. Yuan, J., Adamski, R. & Chen, J. Focus on histone variant H2AX: To be or not to be. *FEBS Lett.* **584,** 3717–3724 (2010).

257. De Rop, V., Padeganeh, A. & Maddox, P. S. CENP-A: the key player behind centromere identity, propagation, and kinetochore assembly. *Chromosoma* **121,** 527–538 (2012).

258. Ling, J. Q. & Hoffman, A. R. Epigenetics of Long-Range Chromatin Interactions. *Pediatr. Res.* **61,** 11R–16R (2007).

259. Parada, L. a, McQueen, P. G. & Misteli, T. Tissue-specific spatial organization of genomes. *Genome Biol.* **5,** R44 (2004).

260. Cremer, T., Cremer, M., Dietzel, S., *et al.* Chromosome territories – a functional nuclear landscape. *Curr. Opin. Cell Biol.* **18,** 307–316 (2006).

261. Zink, D., Fische, A. H. & Nickerson, J. a. Nuclear structure in cancer cells. *Nat. Rev. Cancer* **4,** 677–687 (2004).

262. Osborne, C. S., Chakalova, L., Brown, K. E., *et al.* Active genes dynamically colocalize to shared sites of ongoing transcription. *Nat. Genet.* **36,** 1065–1071 (2004).

263. Nikiforova, M. N. Proximity of Chromosomal Loci That Participate in Radiation-Induced Rearrangements in Human Cells. *Science (80-.).* **290,** 138–141 (2000).

264. Roix, J. J., McQueen, P. G., Munson, P. J., *et al.* Spatial proximity of translocation-prone gene loci in human lymphomas. *Nat. Genet.* **34,** 287–291 (2003).

265. Parada, L. a, Sotiriou, S. & Misteli, T. Spatial genome organization. *Exp. Cell Res.* **296,** 64–70 (2004).

266. Tomlins, S. a. Recurrent Fusion of TMPRSS2 and ETS Transcription Factor Genes in Prostate Cancer. *Science (80-.).* **310,** 644–648 (2005).

267. Klezovitch, O., Risk, M., Coleman, I., *et al.* A causal role for ERG in neoplastic transformation of prostate epithelium. *Proc. Natl. Acad. Sci.* **105,** 2105–2110 (2008).

268. Mani, R.-S., Tomlins, S. a, Callahan, K., *et al.* Induced Chromosomal Proximity and Gene Fusions in Prostate Cancer. *Science (80-.).* **326,** 1230–1230 (2009).

269. Kunderfranco, P., Mello-Grand, M., Cangemi, R., *et al.* ETS Transcription Factors Control Transcription of EZH2 and Epigenetic Silencing of the Tumor Suppressor Gene Nkx3.1 in Prostate Cancer. *PLoS One* **5,** e10547 (2010).

270. Jones, P. a. & Baylin, S. B. The Epigenomics of Cancer. *Cell* **128,** 683–692 (2007).

271. Choi, J. D. & Lee, J.-S. Interplay between Epigenetics and Genetics in Cancer. *Genomics Inform.* **11,** 164 (2013).

272. Lee, D.-H. Oxidative DNA damage induced by copper and hydrogen peroxide promotes CG->TT tandem mutations at methylated CpG dinucleotides in nucleotide excision repair-deficient cells. *Nucleic Acids Res.* **30,** 3566–3573 (2002).

273. Soussi, T. & Béroud, C. Significance of TP53 mutations in human cancer: A critical analysis of mutations at CPG dinucleotides. *Hum. Mutat.* **21,** 192–200 (2003).

274. Parry, T. E. Mutagenic mechanisms in leukemia and cancer: A new concept. *Leuk. Res.* **30,** 1079–1083 (2006).

275. Ning, B., Li, W., Zhao, W., *et al.* Targeting epigenetic regulations in cancer. *Acta Biochim. Biophys. Sin. (Shanghai).* 1–13 (2015). doi:10.1093/abbs/gmv116

276. Sanders, M. a. & Salisbury, J. L. Centrin plays an essential role in microtubule severing during flagellar excision in Chlamydomonas reinhardtii. *J Cell Biol.* **124,** 795–805 (1994).

277. Laferté, S., Loh, L. C. & Keeler, V. Monoclonal antibodies specific for human tumor-associated antigen 90K/Mac-2 binding protein: Tools to examine protein conformation and function. *J. Cell. Biochem.* **77,** 540–559 (2000).

278. Schweiger, M.-R., You, J. & Howley, P. M. Bromodomain Protein 4 Mediates the Papillomavirus E2 Transcriptional Activation Function. *J. Virol.* **80,** 4276–4285 (2006).

279. Laemmli, U. K. Cleavage of structural proteins during the assembly of the head of bacteriophage T4. *Nature* **227,** 680–685 (1970).

280. Towbin, H., Staehelin, T. & Gordon, J. Electrophoretic transfer of proteins from polyacrylamide gels to nitrocellulose sheets: procedure and some applications. *Proc. Natl. Acad. Sci. U. S. A.* **76,** 4350–4354 (1979).

281. Qian, J., Lesage, B., Beullens, M., *et al.* PP1/repo-man dephosphorylates mitotic histone H3 at T3 and regulates chromosomal aurora B targeting. *Curr. Biol.* **21,** 766–773 (2011).

282. Hutchins, J. R. a, Toyoda, Y., Hegemann, B., *et al.* Systematic Analysis of Human Protein Complexes Identifies Chromosome Segregation Proteins. *Science (80-.).* **328,** 593–599 (2010).

283. Badano, J. L., Teslovich, T. M. & Katsanis, N. The centrosome in human genetic disease. *Nat. Rev. Genet.* **6,** 194–205 (2005).

284. Chang, J., Cizmecioglu, O., Hoffmann, I., *et al.* PLK2 phosphorylation is critical for CPAP function in procentriole formation during the centrosome cycle. *EMBO J.* **29,** 2395–2406 (2010).

285. Zou, C., Li, J., Bai, Y., *et al.* Centrobin: A novel daughter centriole-associated protein that is required for centriole duplication. *J. Cell Biol.* **171,** 437–445 (2005).

286. Conroy, P. C., Saladino, C., Dantas, T. J., *et al.* C-NAP1 and rootletin restrain DNA damage-induced centriole splitting and facilitate ciliogenesis. *Cell Cycle* **11,** 3769–3778 (2012).

287. Lee, K. & Rhee, K. PLK1 phosphorylation of pericentrin initiates centrosome maturation at the onset of mitosis. *J. Cell Biol.* **195,** 1093–1101 (2011).

288. Kishi, K., van Vugt, M. a T. M., Okamoto, K., *et al.* Functional dynamics of Polo-like kinase 1 at the centrosome. *Mol. Cell. Biol.* **29,** 3134–3150 (2009).

289. Haren, L., Stearns, T. & Lüders, J. Plk1-dependent recruitment of γ-tubulin complexes to mitotic centrosomes involves multiple PCM components. *PLoS One* **4,** (2009).

290. Santamaria, A., Wang, B., Elowe, S., *et al.* The Plk1-dependent phosphoproteome of the early mitotic spindle. *Mol. Cell. Proteomics* **10,** M110.004457 (2011).

291. Mayor, T., Meraldi, P., Stierhof, Y. D., *et al.* Protein kinases in control of the centrosome cycle. *FEBS Lett.* **452,** 92–95 (1999).

292. Bruinsma, W., Aprelia, M., Kool, J., *et al.* Spatial Separation of Plk1 Phosphorylation and Activity. *Front. Oncol.* **5,** 1–8 (2015).

293. Meraldi, P. & Nigg, E. a. Centrosome cohesion is regulated by a balance of

kinase and phosphatase activities. *J. Cell Sci.* **114,** 3749–3757 (2001).

294. Plo, I. & Lopez, B. AKT1 represses gene conversion induced by different genotoxic stresses and induces supernumerary centrosomes and aneuploidy in hamster ovary cells. *Oncogene* **28,** 2231–2237 (2009).

295. Chouinard, G., Clément, I., Lafontaine, J., *et al.* Cell cycle-dependent localization of CHK2 at centrosomes during mitosis. *Cell Div.* **8,** 7 (2013).

296. Wunderlich, A. Direct regulation of the interferon signaling pathway by the bromodomain containing protein 4. (Freie Universität Berlin, 2012).

297. Decker, T., Lew, D. J., Mirkovitch, J., *et al.* Cytoplasmic activation of GAF, an IFN-gamma-regulated DNA-binding factor. *EMBO J.* **10,** 927–932 (1991).

298. Eilers, a, Georgellis, D., Klose, B., *et al.* Differentiation-regulated serine phosphorylation of STAT1 promotes GAF activation in macrophages. *Mol. Cell. Biol.* **15,** 3579–86 (1995).

299. Rigaut, G., Shevchenko, A., Rutz, B., *et al.* A generic protein purification method for protein complex characterization and proteome exploration. *Nat. Biotechnol.* **17,** 1030–1032 (1999).

300. Xu, X., Song, Y., Li, Y., *et al.* The tandem affinity purification method: An efficient system for protein complex purification and protein interaction identification. *Protein Expr. Purif.* **72,** 149–156 (2010).

301. Chang, I. F. Mass spectrometry-based proteomic analysis of the epitope-tag affinity purified protein complexes in eukaryotes. *Proteomics* **6,** 6158–6166 (2006).

302. Papageorgio, C., Brachmann, R., Zeng, J., *et al.* MAGED2: A novel p53-dissociator. *Int. J. Oncol.* **31,** 1205–1211 (2007).

303. Zyss, D. & Gergely, F. Centrosome function in cancer: guilty or innocent? *Trends Cell Biol.* **19,** 334–346 (2009).

304. Godinho, S. a & Pellman, D. Causes and consequences of centrosome abnormalities in cancer. *Phil. Trans. R. Soc. B* **369,** 189–203 (2014).

305. Wloga, D. & Gaertig, J. Post-translational modifications of microtubules. *J. Cell Sci.* **124,** 154–154 (2010).

306. Dikovskaya, D., Newton, I. P. & Näthke, I. S. The adenomatous polyposis coli protein is required for the formation of robust spindles formed in CSF Xenopus extracts. *Mol. Biol. Cell* **15,** 2978–2991 (2004).

307. Louie, R. K. Adenomatous polyposis coli and EB1 localize in close proximity of the mother centriole and EB1 is a functional component of centrosomes. *J. Cell Sci.* **117,** 1117–1128 (2004).

308. Lui, C., Ashton, C., Sharma, M., *et al.* APC functions at the centrosome to stimulate microtubule growth. *Int. J. Biochem. Cell Biol.* **70,** 39–47 (2016).

309. Madarampalli, B., Yuan, Y., Liu, D., *et al.* ATF5 Connects the Pericentriolar Materials to the Proximal End of the Mother Centriole. *Cell* **162,** 580–592 (2015).

310. Kleylein-Sohn, J., Westendorf, J., Le Clech, M., *et al.* Plk4-Induced Centriole Biogenesis in Human Cells. *Dev. Cell* **13,** 190–202 (2007).

311. Cormier, A., Clément, M. J., Knossow, M., *et al.* The PN2-3 domain of centrosomal P4.1-associated protein implements a novel mechanism for tubulin sequestration. *J. Biol. Chem.* **284,** 6909–6917 (2009).

312. Hsu, W.-B., Hung, L.-Y., Tang, C.-J. C., *et al.* Functional characterization of the microtubule-binding and -destabilizing domains of CPAP and d-SAS-4. *Exp. Cell Res.* **314,** 2591–2602 (2008).

313. Hung, L.-Y. Identification of a Novel Microtubule-destabilizing Motif in CPAP That Binds to Tubulin Heterodimers and Inhibits Microtubule Assembly. *Mol. Biol. Cell* **15,** 2697–2706 (2004).

314. Hatzopoulos, G. N., Erat, M. C., Cutts, E., *et al.* Structural analysis of the G-box domain of the microcephaly protein CPAP suggests a role in centriole architecture. *Structure* **21,** 2069–2077 (2013).

315. Pelletier, L., O'Toole, E., Schwager, A., *et al.* Centriole assembly in Caenorhabditis elegans. *Nature* **444,** 619–623 (2006).

316. Duensing, A., Liu, Y., Perdreau, S. a, *et al.* Centriole overduplication through the concurrent formation of multiple daughter centrioles at single maternal templates. *Oncogene* **26,** 6280–6288 (2007).

317. Dorval, T., Ogier, A., Genovesio, A., *et al.* Contextual Automated 3D Analysis of Subcellular Organelles Adapted to High-Content Screening. *J. Biomol. Screen.* **15,** 847–857 (2010).

318. Shimi, T., Butin-Israeli, V., Adam, S. a, *et al.* The role of nuclear lamin B1 in cell proliferation and senescence. *Genes Dev.* **25,** 2579–93 (2011).

319. Vargas, J. D., Hatch, E. M., Anderson, D. J., *et al.* Transient nuclear envelope rupturing during interphase in human cancer cells. *Nucleus* **3,** 88–100 (2012).

320. Ivanov, a., Pawlikowski, J., Manoharan, I., *et al.* Lysosome-mediated processing of chromatin in senescence. *J. Cell Biol.* **202,** 129–143 (2013).

321. Funkhouser, C. M., Sknepnek, R., Shimi, T., *et al.* Mechanical model of blebbing in nuclear lamin meshworks. *Proc. Natl. Acad. Sci. U. S. A.* **110,** 3248–53 (2013).

322. Bharadwaj, R. & Yu, H. The spindle checkpoint, aneuploidy, and cancer. *Oncogene* **23,** 2016–2027 (2004).

323. Fukasawa, K. Centrosome amplification, chromosome instability and cancer development. *Cancer Lett.* **230,** 6–19 (2005).

324. Duensing, S. & Münger, K. Centrosome abnormalities, genomic instability and carcinogenic progression. *Biochim. Biophys. Acta - Rev. Cancer* **1471,** (2001).

325. Duensing, A. & Duensing, S. Centrosomes, polyploidy and cancer. *Adv. Exp. Med. Biol.* **676,** 93–103 (2010).

326. Fang, X. & Zhang, P. Aneuploidy and tumorigenesis. *Semin. Cell Dev. Biol.* **22,** 595–601 (2011).

327. Gordon, D. J., Resio, B. & Pellman, D. Causes and consequences of aneuploidy in cancer. *Nat. Publ. Gr.* **13,** 189–203 (2012).

328. Sluder, G. & Nordberg, J. J. The good, the bad and the ugly: the practical consequences of centrosome amplification. *Curr. Opin. Cell Biol.* **16,** 49–54 (2004).

329. Quintyne, N. J., Reing, J. E., Hoffelder, D. R., *et al.* Spindle multipolarity is prevented by centrosomal clustering. *Science* **307,** 127–129 (2005).

330. Chow, J. P. H. & Poon, R. Y. C. in *Advances in experimental medicine and biology* **676,** 57–71 (2010).

331. Borel, F., Lohez, O. D., Lacroix, F. B., *et al.* Multiple centrosomes arise from tetraploidy checkpoint failure and mitotic centrosome clusters in p53 and RB pocket protein-compromised cells. *Proc. Natl. Acad. Sci. U. S. A.* **99,** 9819–24 (2002).

332. Kwon, M., Godinho, S. a., Chandhok, N. S., *et al.* Mechanisms to suppress multipolar divisions in cancer cells with extra centrosomes. *Genes Dev.* **22,** 2189–2203 (2008).

333. Silkworth, W. T., Nardi, I. K., Scholl, L. M., *et al.* Multipolar Spindle Pole Coalescence Is a Major Source of Kinetochore Mis-Attachment and Chromosome Mis-Segregation in Cancer Cells. *PLoS One* **4,** e6564 (2009).

334. Li, M., Fang, X., Baker, D. J., *et al.* The ATM – p53 pathway suppresses aneuploidy-induced tumorigenesis. *Pnas* **107,** 14188–14193 (2010).

335. Alexander, A., Cai, S.-L., Kim, J., *et al.* ATM signals to TSC2 in the cytoplasm to regulate mTORC1 in response to ROS. *Proc. Natl. Acad. Sci. U. S. A.* **107,** 4153–4158 (2010).

336. Yan, S., Sorrell, M. & Berman, Z. Functional interplay between ATM/ATR-mediated DNA damage response and DNA repair pathways in oxidative stress. *Cell. Mol. Life Sci.* **71,** 3951–3967 (2014).

337. Thompson, S. L. & Compton, D. a. Proliferation of aneuploid human cells is limited by a p53-dependent mechanism. *J. Cell Biol.* **188,** 369–381 (2010).

338. Williams, B. R., Prabhu, V. R., Hunter, K. E., *et al.* Aneuploidy Affects Proliferation and Spontaneous Immortalization in Mammalian Cells. *Science (80-.).* **322,** 703–709 (2008).

339. Dimozi, A., Mavrogonatou, E., Sklirou, A., *et al.* Oxidative stress inhibits the

proliferation, induces premature senescence and promotes a catabolic phenotype in human nucleus pulposus intervertebral disc cells. *Eur. Cell. Mater.* **30,** 89–103 (2015).

340. Allan, L. a & Fried, M. p53-dependent apoptosis or growth arrest induced by different forms of radiation in U2OS cells: p21WAF1/CIP1 repression in UV induced apoptosis. *Oncogene* **18,** 5403–5412 (1999).

341. Diller, L., Kassel, J., Nelson, C. E., *et al.* P53 Functions As a Cell Cycle Control Protein in Osteosarcomas. *Mol. Cell. Biol.* **10,** 5772–5781 (1990).

342. Isfort, R. J., Cody, D. B., Lovell, G., *et al.* Analysis of oncogenes, tumor suppressor genes, autocrine growth-factor production, and differentiation state of human osteosarcoma cell lines. *Mol. Carcinog.* **14,** 170–178 (1995).

343. McGonnell, I. M., Grigoriadis, A. E., Lam, E. W. F., *et al.* A specific role for phosphoinositide 3-kinase and AKT in osteoblasts? *Front. Endocrinol. (Lausanne).* **3,** 1–8 (2012).

344. Dijkers, P. F. FKHR-L1 can act as a critical effector of cell death induced by cytokine withdrawal: protein kinase B-enhanced cell survival through maintenance of mitochondrial integrity. *J. Cell Biol.* **156,** 531–542 (2002).

345. Sunters, a., Fernandez de Mattos, S., Stahl, M., *et al.* FoxO3a Transcriptional Regulation of Bim Controls Apoptosis in Paclitaxel-treated Breast Cancer Cell Lines. *J. Biol. Chem.* **278,** 49795–49805 (2003).

346. Datta, S. R., Ranger, A. M., Lin, M. Z., *et al.* Survival factor-mediated BAD phosphorylation raises the mitochondrial threshold for apoptosis. *Dev. Cell* **3,** 631–643 (2002).

347. Wullschleger, S., Loewith, R. & Hall, M. N. TOR Signaling in Growth and Metabolism. *Cell* **124,** 471–484 (2006).

348. Dijkers, P. F., Medema, R. H., Pals, C., *et al.* Forkhead transcription factor FKHR-L1 modulates cytokine-dependent transcriptional regulation of p27(KIP1). *Mol. Cell. Biol.* **20,** 9138–48 (2000).

349. Ho, K. K., Myatt, S. S. & Lam, E. W.-F. Many forks in the path: cycling with FoxO. *Oncogene* **27,** 2300–2311 (2008).

350. Zhou, B. P., Liao, Y., Xia, W., *et al.* Cytoplasmic localization of p21Cip1/WAF1 by Akt-induced phosphorylation in HER-2/neu-overexpressing cells. *Nat. Cell Biol.* **3,** 245–252 (2001).

351. Liang, J., Zubovitz, J., Petrocelli, T., *et al.* PKB/Akt phosphorylates p27, impairs nuclear import of p27 and opposes p27-mediated G1 arrest. *Nat. Med.* **8,** 1153–1160 (2002).

352. El-Deiry, W. S. Akt takes centre stage in cell-cycle deregulation. *Nat. Cell Biol.* **3,** E71–3 (2001).

353. Liang, J. & Slingerland, J. M. Multiple Roles of the PI3K/PKB (Akt) Pathway in Cell Cycle Progression. *Cell Cycle* **2,** 336–342 (2003).

354. Manning, B. D. & Cantley, L. C. AKT/PKB Signaling: Navigating Downstream. *Cell* **129,** 1261–1274 (2007).

355. Toker, A. & Marmiroli, S. Signaling specificity in the Akt pathway in biology and disease. *Adv. Biol. Regul.* **55,** 28–38 (2014).

356. Sherline, P. & Mascardo, R. N. Epidermal growth factor induces rapid centrosomal separation in HeLa and 3T3 cells. *J Cell Biol* **63,** 507–511 (1982).

357. Sherline, P. & Mascardo, R. Epidermal growth factor-induced centrosomal separation: mechanism and relationship to mitogenesis. *J. Cell Biol.* **95,** 316–322 (1982).

358. Liu, X., Shi, Y., Woods, K. W., *et al.* Akt Inhibitor A-443654 Interferes with Mitotic Progression by Regulating Aurora A Kinase Expression. *Biotechnology* **10,** 828–837 (2008).

359. Gan, H. K., Kaye, A. H. & Luwor, R. B. The EGFRvIII variant in glioblastoma multiforme. *J. Clin. Neurosci.* **16,** 748–754 (2009).

360. Li, L., Dutra, A., Pak, E., *et al.* EGFRvIII expression and PTEN loss synergistically induce chromosomal instability and glial tumors. *Neuro. Oncol.* **11,** 9–21 (2009).

361. Nam, H.-J., Chae, S., Jang, S.-H., *et al.* The PI3K-Akt mediates oncogenic Met-induced

centrosome amplification and chromosome instability. *Carcinogenesis* **31,** 1531–40 (2010).

362. Mardin, B., Isokane, M., Cosenza, M., *et al.* EGF-Induced Centrosome Separation Promotes Mitotic Progression and Cell Survival. *Dev. Cell* **25,** 229–240 (2013).

363. Leonard, M. K., Hill, N. T., Bubulya, P. a, *et al.* The PTEN-Akt pathway impacts the integrity and composition of mitotic centrosomes. *Cell Cycle* **12,** 1406–15 (2013).

364. Zhao, J., Zou, Y., Liu, H., *et al.* TEIF associated centrosome activity is regulated by EGF/PI3K/Akt signaling. *Biochim. Biophys. Acta* **1843,** 1851–1864 (2014).

365. Pietromonaco, S. F., Seluja, G. a & Elias, L. Identification of enzymatically active ca2+/calmodulin-dependent protein-kinase in centrosomes of hematopoietic-cells . *Blood Cells Mol. Dis.* **21,** 34–41 (1995).

366. Matsumoto, Y. & Maller, J. L. Calcium, calmodulin, and CaMKII requirement for initiation of centrosome duplication in Xenopus egg extracts. *Science (80-.).* **295,** 499–502 (2002).

367. Puram, S. V, Kim, A. H., Ikeuchi, Y., *et al.* A CaMKIIβ signaling pathway at the centrosome regulates dendrite patterning in the brain. *Nat. Neurosci.* **14,** 973–83 (2011).

368. Racioppi, L. & Means, A. R. Calcium/calmodulin-dependent kinase IV in immune and inflammatory responses: novel routes for an ancient traveller. *Trends Immunol.* **29,** 600–607 (2008).

369. Means, A. R. Regulatory Cascades Involving Calmodulin-Dependent Protein Kinases. *Mol. Endocrinol.* **14,** 4–13 (2000).

370. Plotnikova, O. V., Nikonova, a. S., Loskutov, Y. V., *et al.* Calmodulin activation of Aurora-A kinase (AURKA) is required during ciliary disassembly and in mitosis. *Mol. Biol. Cell* **23,** 2658–2670 (2012).

371. Dai, G., Qian, Y., Chen, J., *et al.* Calmodulin activation of polo-like kinase 1 is required during mitotic entry. *Biochem. cell Biol.* **91,** 287–94 (2013).

372. Galletta, B. J., Guillen, R. X., Fagerstrom, C. J., *et al.* Drosophila pericentrin requires interaction with calmodulin for its function at centrosomes and neuronal basal bodies but not at sperm basal bodies. *Mol. Biol. Cell* **25,** 2682–94 (2014).

373. Roderick, H. L. & Cook, S. J. Ca2+ signalling checkpoints in cancer: remodelling Ca2+ for cancer cell proliferation and survival. *Nat. Rev. Cancer* **8,** 361–375 (2008).

374. Sato, N., Mizumoto, K., Nakamura, M., *et al.* A possible role for centrosome overduplication in radiation-induced cell death. *Oncogene* **19,** 5281–5290 (2000).

375. Sato, N., Mizumoto, K., Nakamura, M., *et al.* Radiation-Induced Centrosome Overduplication and Multiple Mitotic Spindles in Human Tumor Cells. *Exp. Cell Res.* **255,** 321–326 (2000).

376. Hut, H. M. J. Centrosomes Split in the Presence of Impaired DNA Integrity during Mitosis. *Mol. Biol. Cell* **14,** 1993–2004 (2003).

377. Dodson, H., Wheatley, S. P. & Morrison, C. G. Involvement of Centrosome Amplification in Radiation-Induced Mitotic Catastrophe. *Cell Cycle* **6,** 364–370 (2007).

378. Bourke, E., Dodson, H., Merdes, A., *et al.* DNA damage induces Chk1-dependent centrosome amplification. *EMBO Rep.* **8,** 603–609 (2007).

379. Eriksson, D., Lofroth, P.-O., Johansson, L., *et al.* Cell Cycle Disturbances and Mitotic Catastrophes in HeLa Hep2 Cells following 2.5 to 10 Gy of Ionizing Radiation. *Clin. Cancer Res.* **13,** 5501s–5508s (2007).

380. Yih, L.-H. Induction of Centrosome Amplification during Arsenite-Induced Mitotic Arrest in CGL-2 Cells. *Cancer Res.* **66,** 2098–2106 (2006).

381. Holmes, A. L. Chronic Exposure to Lead Chromate Causes Centrosome Abnormalities and Aneuploidy in Human Lung Cells. *Cancer Res.* **66,** 4041–4048 (2006).

382. Robinson, H. M. R., Black, E. J., Brown, R., *et al.* DNA Mismatch Repair and Chk1-Dependent Centrosome Amplification in Response to DNA Alkylation Damage. *Cell Cycle* **6,** 982–992 (2007).

383. Saladino, C., Bourke, E., Conroy, P. C., *et al.* Centriole separation in DNA damage-induced centrosome amplification. *Environ. Mol. Mutagen.* **50,** 725–732 (2009).

384. Löffler, H., Fechter, A., Liu, F. Y., *et al.* DNA damage-induced centrosome amplification occurs via excessive formation of centriolar satellites. *Oncogene* **32,** 2963–2972 (2013).

385. Wang, C.-Y., Huang, E. Y.-H., Huang, S.-C., *et al.* DNA-PK/Chk2 induces centrosome amplification during prolonged replication stress. *Oncogene* **34,** 1–7 (2014).

386. Zachos, G. & Gillespie, D. a F. Exercising restraints: role of Chk1 in regulating the onset and progression of unperturbed mitosis in vertebrate cells. *Cell Cycle* **6,** 810–813 (2007).

387. Krämer, A., Lukas, J. & Bartek, J. Checking Out the Centrosome. *Cell Cycle* **3,** 1390–1393 (2004).

388. Bartek, J. & Lukas, J. Chk1 and Chk2 kinases in checkpoint control and cancer. *Cancer Cell* **3,** 421–9 (2003).

389. Pihan, G. a, Purohit, a, Wallace, J., *et al.* Centrosome defects can account for cellular and genetic changes that characterize prostate cancer progression. *Cancer Res.* **61,** 2212–9 (2001).

390. Pihan, G. a, Purohit, A., Wallace, J., *et al.* Centrosome defects and genetic instability in malignant tumors. *Cancer Res.* **58,** 3974–3985 (1998).

391. Grassadonia, A., Tinari, N., Natoli, C., *et al.* Circulating autoantibodies to LGALS3BP: A novel biomarker for cancer. *Dis. Markers* **35,** 747–752 (2013).

392. Sardana, G., Marshall, J. & Diamandis, E. P. Discovery of candidate tumor markers for prostate cancer via proteomic analysis of cell culture-conditioned medium. *Clin. Chem.* **53,** 429–437 (2007).

393. Xue, H., Lu, B. & Lai, M. The cancer secretome: a reservoir of biomarkers. *J. Transl. Med.* **6,** 52 (2008).

394. Wu, C.-C., Hsu, C.-W., Chen, C.-D., *et al.* Candidate serological biomarkers for cancer identified from the secretomes of 23 cancer cell lines and the human protein atlas. *Mol. Cell. Proteomics* **9,** 1100–17 (2010).

395. Ulmer, T. a, Keeler, V., Loh, L., *et al.* Tumor-associated antigen 90K/Mac-2-binding protein: possible role in colon cancer. *J. Cell. Biochem.* **98,** 1351–66 (2006).

396. Scambia, G., Panici, P. B., Baiocchi, G., *et al.* Measurement of a monoclonal-antibody-defined antigen (90K) in the sera of patients with ovarian cancer. *Anticancer Res.* **8,** 761–764 (1988).

397. Cesinaro, A. M., Natoli, C., Grassadonia, A., *et al.* Expression of the 90K tumor-associated protein in benign and malignant melanocytic lesions. *J. Invest. Dermatol.* **119,** 187–90 (2002).

398. Kashyap, M. K., Harsha, H. C., Renuse, S., *et al.* SILAC-based quantitative proteomic approach to identify potential biomarkers from the esophageal squamous cell carcinoma secretome. *Cancer Biol. Ther.* **10,** 796–810 (2010).

399. Koopmann, J., Thuluvath, P. J., Zahurak, M. L., *et al.* Mac-2-binding protein is a diagnostic marker for biliary tract carcinoma. *Cancer* **101,** 1609–15 (2004).

400. Srirajaskanthan, R., Caplin, M. E., Waugh, M. G., *et al.* Identification of Mac-2-binding protein as a putative marker of neuroendocrine tumors from the analysis of cell line secretomes. *Mol. Cell. Proteomics* **9,** 656–66 (2010).

401. Velonas, V., Woo, H., Remedios, C., *et al.* Current Status of Biomarkers for Prostate Cancer. *Int. J. Mol. Sci.* **14,** 11034–11060 (2013).

402. Hägglöf, C., Hammarsten, P., Strömvall, K., *et al.* TMPRSS2-ERG expression predicts prostate cancer survival and associates with stromal biomarkers. *PLoS One* **9,** e86824 (2014).

403. Lehtonen, a, Matikainen, S. & Julkunen, I. Interferons up-regulate STAT1, STAT2, and IRF family transcription factor gene expression in human peripheral blood mononuclear cells and macrophages. *J. Immunol.* **159,** 794–803 (1997).

404. Wong, L. H., Sim, H., Chatterjee-Kishore, M., *et al.* Isolation and characterization of a human STAT1 gene regulatory element. Inducibility by interferon (IFN) types I and

II and role of IFN regulatory factor-1. *J. Biol. Chem.* **277,** 19408–19417 (2002).

405. Patel, M. C., Debrosse, M., Smith, M., *et al.* BRD4 Coordinates Recruitment of Pause Release Factor P-TEFb and the Pausing Complex NELF/DSIF To Regulate Transcription Elongation of Interferon-Stimulated Genes. *Mol. Cell. Biol.* **33,** 2497–2507 (2013).

406. LeRoy, G., Chepelev, I., DiMaggio, P. a, *et al.* Proteogenomic characterization and mapping of nucleosomes decoded by Brd and HP1 proteins. *Genome Biol.* **13,** R68 (2012).

407. Hussong, M., Börno, S. T., Kerick, M., *et al.* The bromodomain protein BRD4 regulates the KEAP1/NRF2-dependent oxidative stress response. *Cell Death Dis.* **5,** e1195 (2014).

408. Darnell, J., Kerr, I. & Stark, G. Jak-STAT pathways and transcriptional activation in response to IFNs and other extracellular signaling proteins. *Science (80-.).* **264,** 1415–1421 (1994).

409. Decker, T., Kovarik, P. & Meinke, A. GAS elements: a few nucleotides with a major impact on cytokine-induced gene expression. *J. Interferon Cytokine Res.* **17,** 121–134 (1997).

410. Schroder, K., Hertzog, P. J., Ravasi, T., *et al.* Interferon-gamma: an overview of signals, mechanisms and functions. *J. Leukoc. Biol.* **75,** 163–89 (2004).

411. Gough, D. J., Levy, D. E., Johnstone, R. W., *et al.* IFNgamma signaling-does it mean JAK-STAT? *Cytokine Growth Factor Rev.* **19,** 383–94 (2008).

412. Krämer, O. H., Baus, D., Knauer, S. K., *et al.* Acetylation of Stat1 modulates NF-κB activity. *Genes Dev.* **20,** 473–485 (2006).

413. Zeng, L. & Zhou, M.-M. Bromodomain: an acetyl-lysine binding domain. *FEBS Lett.* **513,** 124–128 (2002).

414. Deb, a, Haque, S. J., Mogensen, T., *et al.* RNA-dependent protein kinase PKR is required for activation of NF-kappa B by IFN-gamma in a STAT1-independent pathway. *J Immunol* **166,** 6170–6180 (2001).

415. Sizemore, N., Agarwal, A., Das, K., *et al.* Inhibitor of B kinase is required to activate a subset of interferon -stimulated genes. *Proc. Natl. Acad. Sci.* **101,** 7994–7998 (2004).

416. Shultz, D. B., Fuller, J. D., Yang, Y., *et al.* Activation of a Subset of Genes by IFN- *γ* Requires IKK *β* but Not Interferon-Dependent Activation of NF- *κ* B. *J. Interf. Cytokine Res.* **27,** 875–884 (2007).

417. Huang, B., Yang, X. D., Zhou, M. M., *et al.* Brd4 coactivates transcriptional activation of NF-kappaB via specific binding to acetylated RelA. *Mol Cell Biol* **29,** 1375–1387 (2009).

418. Yu, J., Yu, J., Mani, R.-S., *et al.* An Integrated Network of Androgen Receptor, Polycomb, and TMPRSS2-ERG Gene Fusions in Prostate Cancer Progression. *Cancer Cell* **17,** 443–454 (2010).

419. Nicodeme, E., Jeffrey, K. L., Schaefer, U., *et al.* Suppression of inflammation by a synthetic histone mimic. *Nature* **468,** 1119–1123 (2010).

420. Muller, S., Filippakopoulos, P. & Knapp, S. Bromodomains as therapeutic targets. *Expert Rev. Mol. Med.* **13,** e29 (2011).

421. Filippakopoulos, P., Qi, J., Picaud, S., *et al.* Selective inhibition of BET bromodomains. *Nature* **468,** 1067–73 (2010).

422. Wee, Z., Li, Z., Lee, P., *et al.* EZH2-mediated inactivation of IFN-γ-JAK-STAT1 signaling is an effective therapeutic target in MYC-driven prostate cancer. *Cell Rep.* **8,** 204–216 (2014).

423. Monaco, S., Rusciano, M. R., Maione, A. S., *et al.* A novel crosstalk between calcium/calmodulin kinases II and IV regulates cell proliferation in myeloid leukemia cells. *Cell. Signal.* **27,** 204–14 (2015).

424. Scambia, G., Panici, P. B., Iacobelli, S., *et al.* Recombinant alpha-2b-interferon enhances the circulating levels of a 90-kilodalton (K) tumor-associated antigen in patients with gynecologic and breast malignancies. *Cancer* **65,** 1325–1328 (1990).

425. Van Baarsen, L. G., Wijbrandts, C. a, Rustenburg, F., *et al.* Regulation of IFN response gene activity during infliximab treatment in rheumatoid arthritis is associated with clinical response to

treatment. *Arthritis Res. Ther.* **12,** R11 (2010).

426. Nielsen, C. T., Lood, C., Ostergaard, O., *et al.* Plasma levels of galectin-3-binding protein reflect type I interferon activity and are increased in patients with systemic lupus erythematosus. *Lupus Sci. Med.* **1,** e000026–e000026 (2014).

427. Matsumoto, G., Namekawa, J. I., Muta, M., *et al.* Targeting of nuclear factor κB pathways by dehydroxymethylepoxyquinomicin, a novel inhibitor of breast carcinomas: Antitumor and antiangiogenic potential in vivo. *Clin. Cancer Res.* **11,** 1287–1293 (2005).

428. Gilmore, T. D. & Herscovitch, M. Inhibitors of NF-κB signaling: 785 and counting. *Oncogene* **25,** 6887–6899 (2006).

429. Tan, J., Yang, X., Zhuang, L., *et al.* Pharmacologic disruption of Polycomb-repressive complex 2-mediated gene repression selectively induces apoptosis in cancer cells. *Genes Dev.* **21,** 1050–1063 (2007).

430. Knutson, S. K., Wigle, T. J., Warholic, N. M., *et al.* A selective inhibitor of EZH2 blocks H3K27 methylation and kills mutant lymphoma cells. *Nat. Chem. Biol.* **8,** 890–896 (2012).

431. Samlowski, W. E., Leachman, S. a., Wade, M., *et al.* Evaluation of a 7-day continuous intravenous infusion of decitabine: Inhibition of promoter-specific and global genomic DNA methylation. *J. Clin. Oncol.* **23,** 3897–3905 (2005).

432. Villar-Garea, A., Fraga, M. F., Espada, J., *et al.* Procaine is a DNA-demethylating agent with growth-inhibitory effects in human cancer cells. *Cancer Res.* **63,** 4984–4989 (2003).

433. Zhang, X., Wheeler, D., Tang, Y., *et al.* Calcium/calmodulin-dependent protein kinase (CaMK) IV mediates nucleocytoplasmic shuttling and release of HMGB1 during lipopolysaccharide stimulation of macrophages. *J. Immunol.* **181,** 5015–23 (2008).

434. Persaud, S. J., Liu, B., Sampaio, H. B., *et al.* Calcium/calmodulin-dependent kinase IV controls glucose-induced Irs2 expression in mouse beta cells via activation of cAMP response element-binding protein. *Diabetologia* **54,** 1109–1120 (2011).

435. Reece, K. M., Mazalouskas, M. D. & Wadzinski, B. E. The Bα and Bδ regulatory subunits of PP2A are necessary for assembly of the CaMKIV·PP2A signaling complex. *Biochem. Biophys. Res. Commun.* **386,** 582–587 (2009).

436. Kumar, C. C. & Madison, V. AKT crystal structure and AKT-specific inhibitors. *Oncogene* **24,** 7493–7501 (2005).

437. Ma, C. X., Janetka, J. W. & Piwnica-Worms, H. Death by releasing the breaks: CHK1 inhibitors as cancer therapeutics. *Trends Mol. Med.* **17,** 88–96 (2011).

438. Yu, Q., La Rose, J., Zhang, H., *et al.* UCN-01 inhibits p53 up-regulation and abrogates γ-radiation-induced G2-M checkpoint independently of p53 by targeting both of the checkpoint kinases, Chk2 and Chk1. *Cancer Res.* **62,** 5743–5748 (2002).

439. Gadhikar, M. a, Sciuto, M. R., Alves, M. V. O., *et al.* Chk1/2 Inhibition Overcomes the Cisplatin Resistance of Head and Neck Cancer Cells Secondary to the Loss of Functional p53. *Mol. Cancer Ther.* **12,** 1860–1873 (2013).

List of Figures

List of Tables

List of Abbreviations

3'UTR	3' untranslated region
A	alanine
aa	amino acid(s)
AKT1	Ak strain transforming, RAC-alpha serine/threonine-protein kinase
APC/C	anaphase-promoting complex/cyclosome
APS	ammonium persulfate
ATM	ataxia telangiectasia mutated
ATR	ATM-and Rad3-related
bp	base pair
BRD4	bromodomain-containing protein 4
BSA	bovine serum albumin
CaMK4	calcium/calmodulin-dependent protein kinase type IV
CBS	calmodulin-binding site
CDC25	cell division cycle 25
CDC25	cell division cycle 25
CDK1/2	cyclin-dependent kinase 1/2
cDNA	complementary DNA
CEP55	centrosomal protein of 55 kDa
CFC	change from control
CGI	CpG island
ChIP-Seq	chromatin immunoprecipitation sequencing
CHK1	checkpoint kinase 1
CHK2	checkpoint kinase 2
CIN	chromosomal instability
CIP	calf-intestinal alkaline phosphatase
CK1d	casein kinase 1 isoform delta
C-Nap1	centrosomal Nek2-associated protein 1
CO_2	carbon dioxide
CP110	centriolar coiled-coil protein of 110 kDa
CPAP	centrosomal P4.1-associated protein
CPAP	centrosomal P4.1-associated protein
CpG	cytosine-(phosphate)-guanine dinucleotide
CREB	cAMP response element-binding protein
DAPI	4', 6-diamidino-2-phenylindole
dH_2O	distilled water
DMEM	Dulbecco's modified Eagle's medium
DNA	deoxyribonucleic acid
DNMT	DNA methyltransferase
dNTPs	deoxyribonucleotide triphosphates
e.g.	exempli gratia, for example
ERG	ETS (erythroblast transformation-specific)-related gene
et al.	et alii, and others
EZH2	enhancer of zeste homolog 2

FACS	fluorescence-activated cell sorting
FCS	fetal calf serum
GAPDH	glyceraldehyde-3-phosphate dehydrogenase
GAS	gamma interferon activation site
GCP3	gamma-tubulin complex component 3
HPRT1	hypoxanthine phosphoribosyltransferase 1
HRPO	horseradish peroxidase
INFα	interferon alpha
INFβ	interferon beta
INFγ	interferon gamma
IPA	Ingenuity Pathway Analysis
ISRE	interferon-sensitive response element
K	lysine
LGALS3BP	lectin galactoside-binding soluble 3-binding protein
MAGED2	melanoma-associated antigen D2
MeOH	methanol
miRNA	microRNA
mRNA	messenger RNA
MS	mass spectrometry
MTOC	microtubule organizing centre
ncRNA	noncoding RNA
NEB	nuclear envelope breakdown
NEK2	NIMA (never in mitosis gene a)-related kinase 2
NFR	nucleosome-free region
NFκB	nuclear factor kappa-light-chain-enhancer of activated B cells
nt	nucleotide(s)
PCM	pericentriolar material
PDK1	phosphoinositide-dependent kinase 1
PFA	paraformaldehyde
PI3K	phosphatidylinositide 3-kinase
PIP2	phosphatidylinositol 4,5-bisphosphate
PIP3	phosphatidylinositol 3,4,5-trisphosphate
PKB	protein kinase B
PKB	protein kinase B
PLK1	polo-like kinase 1
PLK4	polo-like kinase 4
PLL	poly-L-lysine
PP2A	protein phosphatase 2 A
PRC1/2	polycomb repressive complex 1/2
pTEFb	positive transcription elongation factor b
qPCR	quantitative real-time polymerase chain reaction
RB	retinoblastoma protein
RISC	RNA-induced silencing complex
RNA Pol II	RNA polymerase II
RNA	ribonucleic acid
RNAi	RNA interference
RNase	ribonuclease
ROS	reactive oxygen species
S	serine

SAC	spindle assembly checkpoint
SAS6	spindle assembly abnormal protein 6 homolog
SDS-PAGE	sodium dodecyl sulphate-polyacrylamide gel electrophoresis
shRNA	short hairpin RNA
siRNA	small interfering RNA
SP1	specificity protein 1
STAT1	signal transducer and activator of transcription 1
STIL	SCL-interrupting locus protein
T	threonine
TAP	tandem affinity purification
TEIF	transcriptional element-interacting factor
TEMED	tetramethylethylenediamine
TMPRSS2	transmembrane protease, serine 2
TNFα	tumor necrosis factor alpha
TSS	transcription start site
TUNEL	terminal deoxynucleotidyl transferase dUTP nick end labelling
γ-TuRC	γ-tubulin ring complex

Units

cpm	count(s) per minute
C_T	cycle threshold
h	hour(s)
kDa	kilodalton(s)
kV	kilovolt(s)
µF	microfarad(s)
µg	microgram(s)
µl	microlitre(s)
µM	micromolar
mA	milliampere
mg	milligram(s)
ml	millilitre(s)
mM	millimolar
mV	millivolts
min	minute(s)
nM	nanomolar
ng	nanogram(s)
Ω	ohm
rpm	read(s) per million/ revolution(s) per minute
s	second(s)
U	unit(s)

Supplement

List of Supplemental Figures

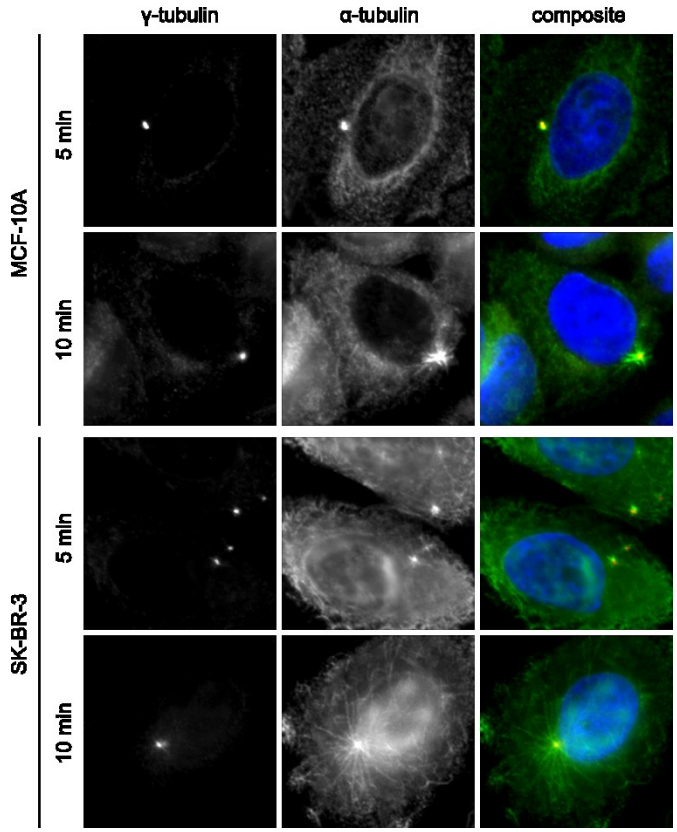

Supplemental Figure 1: Microtubule regrowth in MCF-10A and SK-BR-3 cells
Example micrographs of the microtubule regrowth assay performed in MCF-10A and SK-BR-3 cells. Microtubules were depolymerized with nocodazole and allowed to regrow after washout with the respective culturing medium for 5 or 10 min. Anti-γ-tubulin-labelled centrosomes are shown in red, anti-α-tubulin-labelled microtubules in green and DAPI-stained DNA in blue in the composite images.

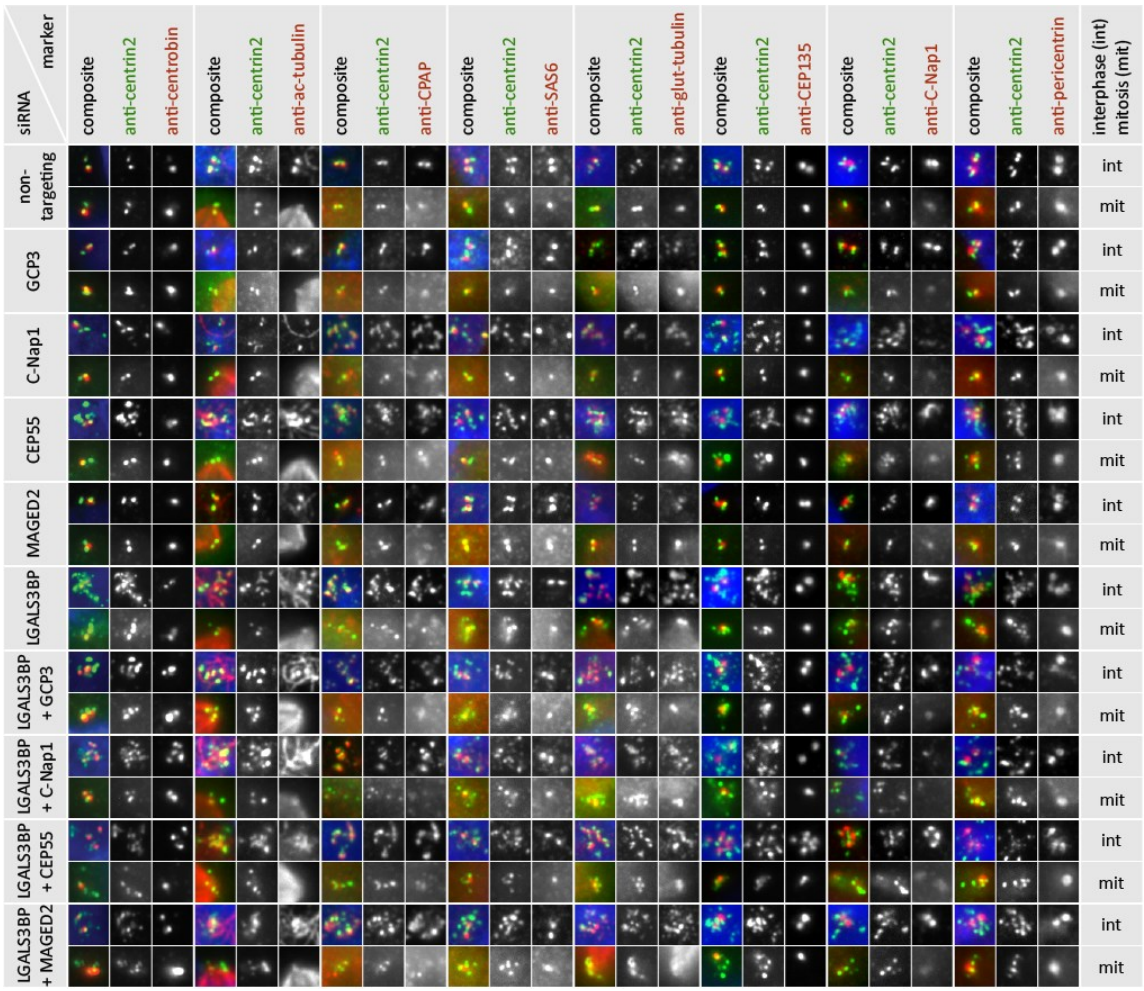

Supplemental Figure 2: Centriolar phenotypes and marker compositions upon RNAi
Centriolar phenotypes as well as localization of certain centriolar and pericentriolar markers were analysed in immunofluorescence microscopy in mitosis and interphase upon single and double knockdown of LGALS3BP and its interacting partners for 72 h in U2OS cells. Non-targeting siRNA served as a negative control. The tested markers centrobin, acetylated tubulin (ac-tubulin), CPAP, SAS6, glutamylated tubulin (glut-tubulin), CEP135, C-Nap1 and pericentrin were antibody-labelled and are shown in red, anti-centrin2-labelling is shown in green and DAPI-stained DNA in blue in the composite images. Micrographs show magnifications of the centrosomal area.

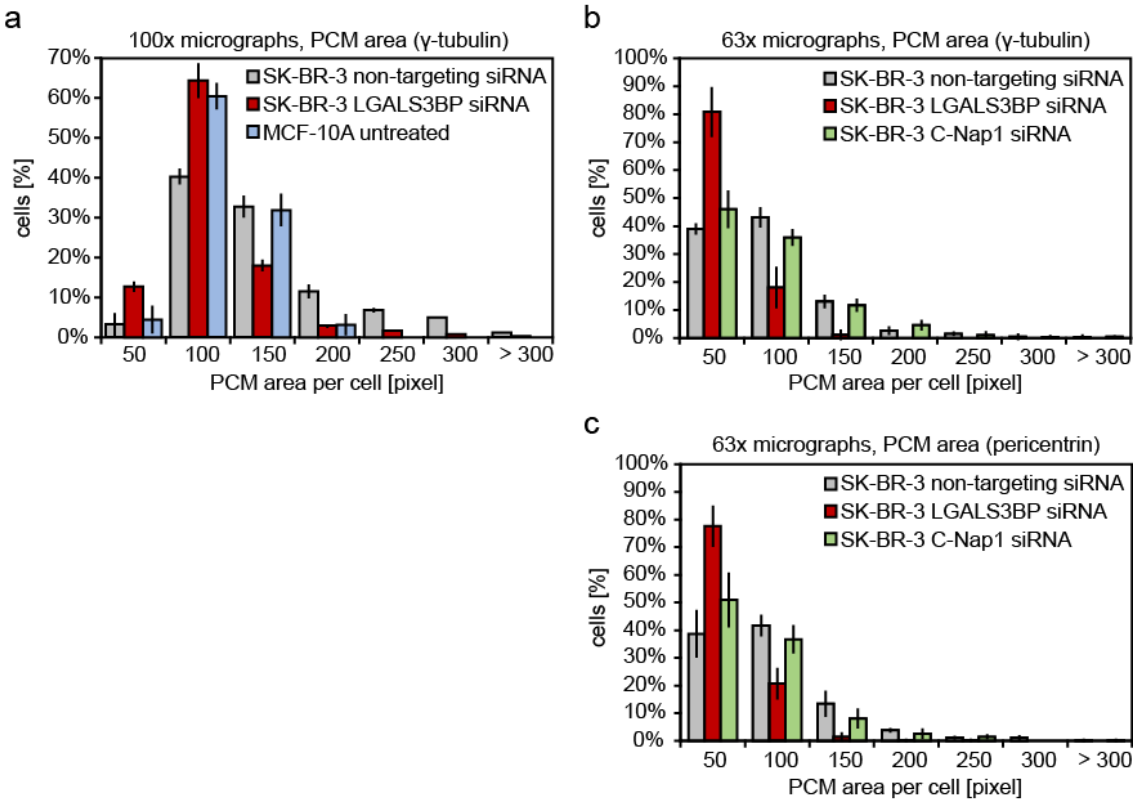

Supplemental Figure 3: PCM hypertrophy is rescued by LGALS3BP depletion in SK-BR-3 cells
(a-c) SK-BR-3 cells that endogenously overexpress LGALS3BP and display PCM hypertrophy were transfected for 72 h with siRNA targeting LGALS3BP or C-Nap1. Non-targeting siRNA served as a negative control. Samples were antibody-labelled for the PCM markers γ-tubulin (a, b) or pericentrin (c) and analysed by immunofluorescence microscopy. The data represent means ± standard deviation of triplicates with each n > 200. **(a)** ImageJ quantification of γ-tubulin area per cell on 100x micrographs revealed a reduction of PCM area in SK-BR-3 cells after LGALS3BP depletion up to control ranges of MCF-10A cells. **(b)** PCM area quantification on 63x micrographs in a second experiment also unveiled a PCM area reduction in SK-BR-3 cells compared to non-targeting siRNA control. Depletion of the LGALS3BP interaction partner C-Nap1, however, did not rescue PCM hypertrophy. **(c)** This was also validated by analysis of pericentrin-labelling.

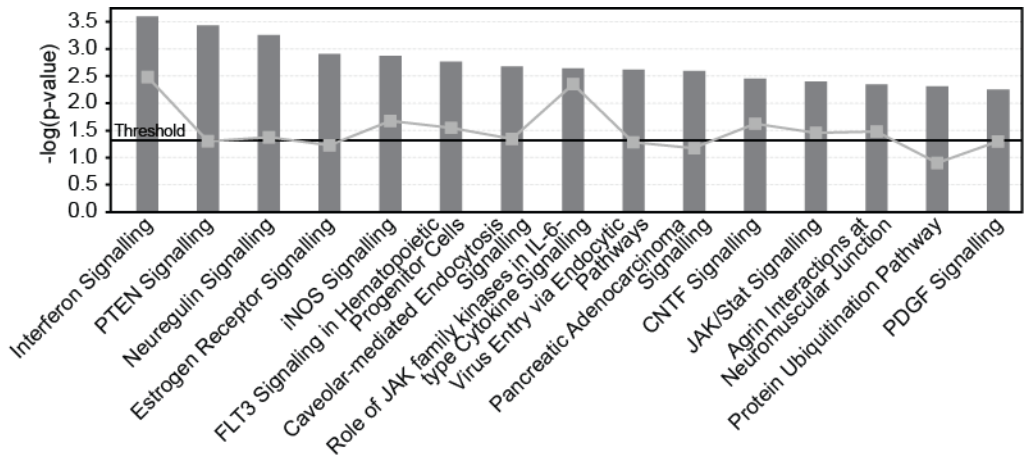

Supplemental Figure 4: IPA of mRNA sequencing data upon BRD4 knockdown
The most significantly affected canonical pathways were identified by Ingenuity Pathway Analysis (IPA) within mRNA sequencing data of a Brd4 knockdown (shC2) in HEK293T cells. The pathways are ranked according to the number of identified differentially expressed genes in a certain pathway in relation to the total number of genes belonging to that specific pathway. Data were obtained from Andrea Wunderlich.

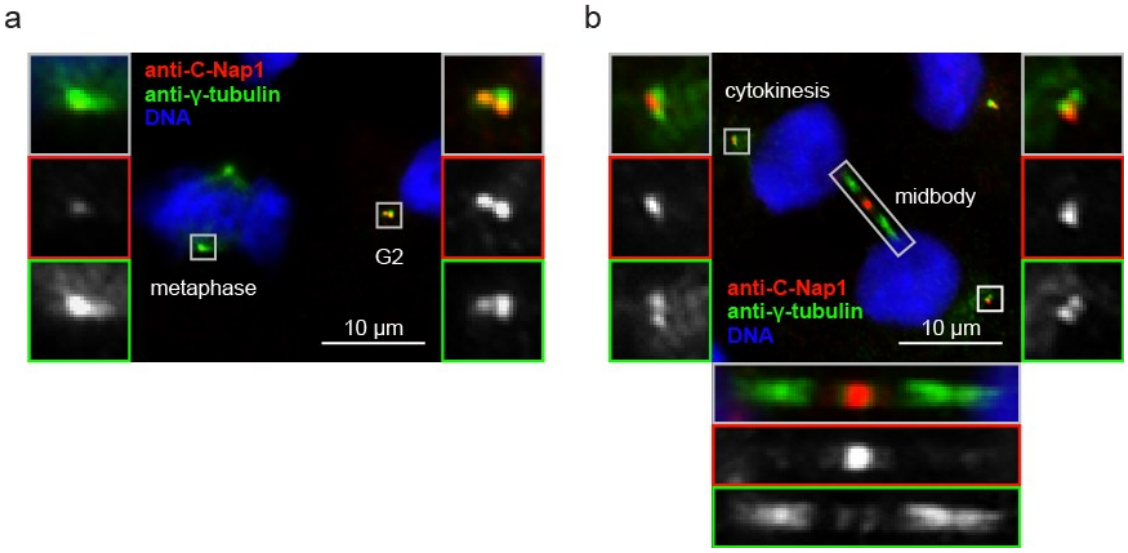

Supplemental Figure 5: Subcellular C-Nap1 localization during different cell cycle stages
(a) Immunofluorescence microscopy analysis of U2OS cells showed a strong C-Nap1-labelling at interphase (e.g. G2) centrosomes whereas C-Nap1 fluorescence intensity at spindle poles in mitosis (e.g. metaphase) appeared utterly weak. **(b)** During cytokinesis C-Nap1-immunolabelling reoccurred at centrosomes and strikingly pronounced at the midbody. C-Nap1-labelling is displayed in red, the PCM labelled with an anti-γ-tubulin antibody in green and DAPI-stained DNA in blue in the composite images. Boxes indicate magnifications of the centrosome or the midbody and scale bars represent 10 µm.

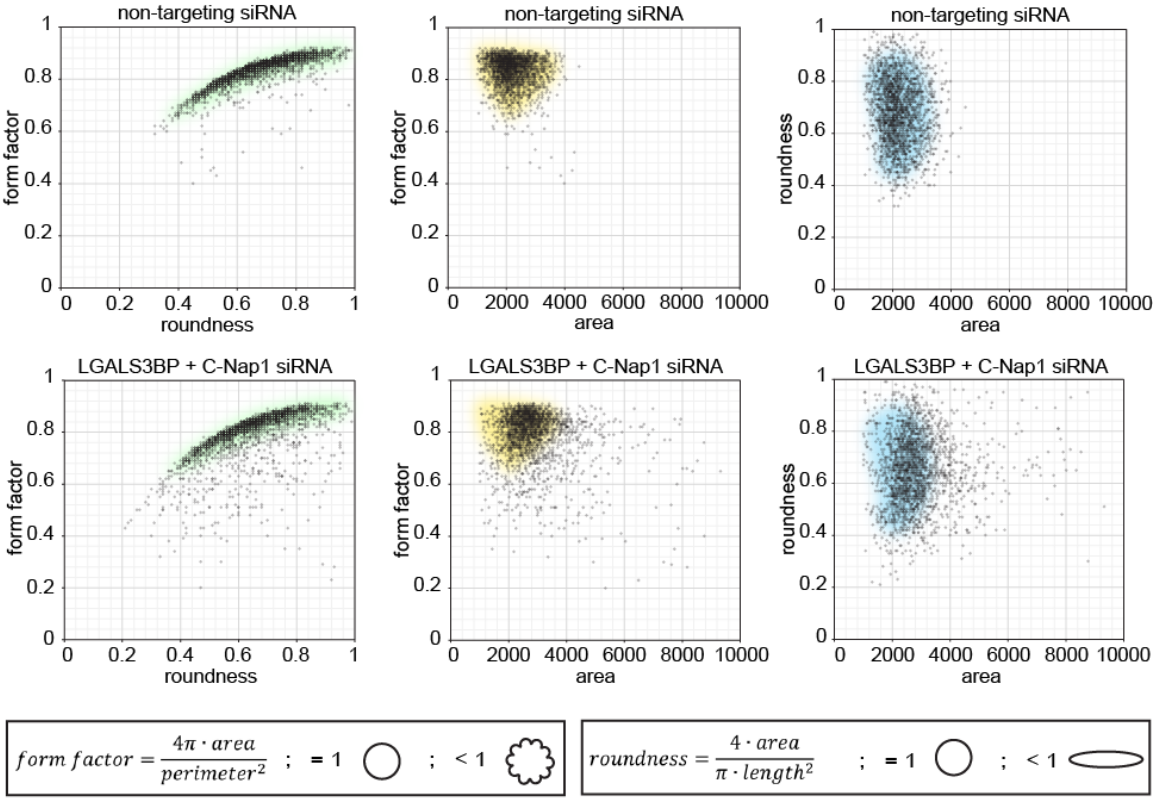

Supplemental Figure 6: Nucleus shapes upon LGALS3BP and C-Nap1 double knockdown
The scatter plots display the outcomes of an initial ImageJ analysis of nucleus shapes as well as nucleus areas in U2OS cells simultaneously depleted for LGALS3BP and C-Nap1 (lower row) opposed to control treated cells (upper row). The clusters of nucleus populations in control cells are highlighted within the plots (green, yellow and blue) to elucidate the shift out of these clusters in LGALS3BP/C-Nap1 double knockdown cells. Double-depleted cells showed a tendency to irregularly shaped nuclei given by lower form factors (plots in left and middle column, form factor described in left bottom box). Plotting the shape descriptors against the nucleus area revealed a shift towards cells with larger nuclei when compared to control cells (plots in middle and right column). Roundness values are not as prominently decreased by the double knockdown when compared to control cells as it was observed for the form factor but rather stay moderate even in cells with greater nucleus area (plots in left and right column, roundness described in right bottom box). The data represent measurements of $n > 2{,}000$ nuclei per single experiment.

List of Supplemental Tables

Supplemental Table 1: Raw data of radiometric AKT1 kinase profiling on LGALS3BP peptides
Raw data of Kinexus AKT1 profiling against synthetic wild type (T220, S256, S444) and mutant (A220, A256, A444) LGALS3BP peptides were obtained by radiometry. The duplicate measurements were averaged and blank-corrected. Measurements are given as counts per minute (cpm). AKT1 activity is given in % and is related to the positive control.

Assay Condition	Assay Results [cpm]	Average Value [cpm]	Corrected Value [cpm]	Activity [%]
Blank (- substrate)	622 684	653	0	0
Control (+regular substrate)	139,831 130,786	135,309	134,656	100
T220 peptide	9,561 9,493	9,527	8,874	7
A220 peptide	2,160 1,972	2,066	1,413	1
S256 peptide	763 619	691	38	0
A256 peptide	605 625	615	-38	0
S444 peptide	643 703	673	20	0
A444 peptide	742 710	726	73	0

Supplemental Table 2: Raw data of radiometric CK1d kinase profiling on LGALS3BP peptides
Raw data of Kinexus CK1d profiling against synthetic wild type T220 and mutant A220 LGALS3BP peptides resulted from a radiometric assay. The duplicate measurements were averaged and blank-corrected. Measurements are given as counts per minute (cpm). CK1d activity is given in % and is related to the positive control.

Assay Condition	Assay Results [cpm]	Average Value [cpm]	Corrected Value [cpm]	Activity [%]
Blank (- substrate)	689 702	696	0	0
Control (+regular substrate)	58,978 57,796	58,387	57,692	100
T220 peptide	6,961 6,845	6,903	6,208	11
A220 peptide	5,637 5,405	5,521	4,826	8

Supplemental Table 3: Raw data of radiometric PLK1 kinase profiling on LGALS3BP peptides
Raw data of Kinexus PLK1 profiling against synthetic wild type (T220, S444) and mutant (A220, A444) LGALS3BP peptides were obtained by radiometry. The duplicate measurements were averaged and blank-corrected. Measurements are given as counts per minute (cpm). PLK1 activity is given in % and is related to the positive control.

Assay Condition	Assay Results [cpm]	Average Value [cpm]	Corrected Value [cpm]	Activity [%]
Blank (- substrate)	758 689	724	0	0
Control (+regular substrate)	51,850 52,028	51,939	51,216	100
T220 peptide	2,175 2,402	2,289	1,565	3
A220 peptide	1,864 2,193	2,029	1,305	3
S444 peptide	1,882 1,464	1,673	950	2
A444 peptide	1,846 1,685	1,766	1,042	2

Supplemental Table 4: Raw data of radiometric CaMK4 kinase profiling on LGALS3BP peptides
Raw data of Kinexus CaMK4 profiling against synthetic wild type (S256, S444) and mutant (A256, A444) LGALS3BP peptides resulted from a radiometric assay. The duplicate measurements were averaged and blank-corrected. Measurements are given as counts per minute (cpm). CaMK4 activity is given in % and is related to the positive control.

Assay Condition	Assay Results [cpm]	Average Value [cpm]	Corrected Value [cpm]	Activity [%]
Blank (- substrate)	748 789	769	0	0
Control (+regular substrate)	175,373 174,998	175,186	174,417	100
S256 peptide	1,124 1,109	1,117	348	0
A256 peptide	1,094 1,155	1,125	356	0
S444 peptide	4,669 4,547	4,608	3,840	2
A444 peptide	2,322 2,339	2,331	1,562	1

Supplemental Table 5: Raw data of radiometric CHK1 kinase profiling on LGALS3BP peptides
Raw data of Kinexus CHK1 profiling against synthetic wild type (S256, S444) and mutant (A256, A444) LGALS3BP peptides were obtained by radiometry. The duplicate measurements were averaged and blank-corrected. Measurements are given as counts per minute (cpm). CHK1 activity is given in % and is related to the positive control.

Assay Condition	Assay Results [cpm]	Average Value [cpm]	Corrected Value [cpm]	Activity [%]
Blank (- substrate)	735 855	6,953	0	0
Control (+regular substrate)	166,720 166,765	166,743	165,948	100
S256 peptide	3,628 3,209	3,419	2,624	2
A256 peptide	2,410 2,495	2,453	1,658	1
S444 peptide	51,225 52,106	51,666	50,871	31
A444 peptide	9,849 6,953	8,401	7,606	5

Supplemental Table 6: Raw data of radiometric CHK2 kinase profiling on LGALS3BP peptides
Raw data of Kinexus CHK2 profiling against synthetic wild type (S256, S444) and mutant (A256, A444) LGALS3BP peptides resulted from a radiometric assay. The duplicate measurements were averaged and blank-corrected. Measurements are given as counts per minute (cpm). CHK2 activity is given in % and is related to the positive control.

Assay Condition	Assay Results [cpm]	Average Value [cpm]	Corrected Value [cpm]	Activity [%]
Blank (- substrate)	711 689	700	0	0
Control (+regular substrate)	126,208 126,208	125,822	125,122	100
S256 peptide	695 698	697	-4	0
A256 peptide	709 697	703	3	0
S444 peptide	3,441 3,678	3,560	2,860	2
A444 peptide	814 699	757	57	0

Curriculum Vitae

Der Lebenslauf ist in der Online-Version aus Gründen des Datenschutzes nicht enthalten.

Selbstständigkeitserklärung

Hiermit erkläre ich, dass ich diese Arbeit selbständig verfasst und nur die angegebenen Hilfsmittel und Quellen in Anspruch genommen habe. Die Experimente und Analysen wurden, sofern nicht anders gekennzeichnet, von mir durchgeführt. Ich versichere, dass diese Arbeit in dieser oder anderer Form keiner anderen Prüfungsbehörde vorgelegt wurde.

Berlin, 16. Dezember 2015 Sophia Schade